

Static and dynamic magnetoelastic properties of spin ice

Dissertation
zur Erlangung des wissenschaftlichen Grades
Doctor rerum naturalium

vorgelegt von

Thomas Stöter
geboren am 24.09.1989 in Magdeburg

Tag der Verteidigung: 21.11.2019

1. Gutachter: Prof. Dr. J. Wosnitza
2. Gutachter: Prof. Dr. J. Geck

Technische Universität Dresden
Institut für Festkörper- und Materialphysik
Fakultät Physik
Bereich Mathematik und Naturwissenschaften
der Technischen Universität Dresden

Eingereicht am 16.07.2019

Verteidigt am 21.11.2019

1. Gutachter: Prof. Dr. J. Wosnitza

2. Gutachter: Prof. Dr. J. Geck

Abstract

The concept of magnetic frustration is a fundamental topic in modern solid-state physics having direct consequences in systems with rich magnetic phases hosting emergent excitations, such as the magnetic monopoles in the spin-ice compounds. One important ingredient of frustration is the lattice that constrains the magnetic spins on it to a site anisotropy and inter-site coupling. Therefore, strong magnetoelastic interactions between the magnetic system and the lattice are expected and investigated in this thesis in detail.

At first, I investigate the dependence of the relative length change of single crystals of the classical spin ices $\text{Dy}_2\text{Ti}_2\text{O}_7$ and $\text{Ho}_2\text{Ti}_2\text{O}_7$ on the magnetic field and temperature by capacitive dilatometry. In terms of the magnetostriction and thermal expansion $\text{Dy}_2\text{Ti}_2\text{O}_7$ and $\text{Ho}_2\text{Ti}_2\text{O}_7$ show qualitatively similar behavior, that seems to be independent of the Kramer or non-Kramers character of the rare-earth ion. The magnitude of the magnetostrictive effect deep in the spin-ice phase at 0.3 K is $\Delta L/L = 2 \times 10^{-5}$ and 2×10^{-4} for $\text{Dy}_2\text{Ti}_2\text{O}_7$ and $\text{Ho}_2\text{Ti}_2\text{O}_7$, respectively. In numerical simulations using a manifold model, the experimental results could be qualitatively reproduced by a combination of exchange and crystal-field striction.

A second highlight of the dilatometric measurements of the spin-ice compounds is the observation of the lattice dynamics. The relaxation processes are rather slow, the longest relaxation times were observed at lowest temperatures and in the field range with magnetostrictive hysteresis, i.e., below 0.9 T for $\text{Dy}_2\text{Ti}_2\text{O}_7$ and below 1.5 T for $\text{Ho}_2\text{Ti}_2\text{O}_7$. I find that the region of longest relaxation coincides well with the kagome-ice phase of the magnetic phase diagrams; the relaxation time is of the order of 5000 s (> 80 min). With increasing temperatures the time scale of the relaxation reduces to minutes at around 0.7 K corresponding to the spin-freezing temperature obtained from ac-susceptibility measurements.

In the second study I investigate the variation of the magnetic properties in dependence of the lattice constant. A systematic reduction of the lattice constant of $\text{Dy}_2\text{Ge}_{2-x}\text{Si}_x\text{O}_7$ can be achieved by substituting the non-magnetic germanium ion in the cubic pyrochlore oxide with silicon. Characteristic properties of a spin-ice phase could be observed in measurements of magnetization, ac susceptibility, and heat capacity. From the temperature shift of the peaks, observed in the temperature-dependent heat capacity, an increase of the strength of the magnetic exchange interaction by a changed ratio of the competing exchange and dipolar interaction is deduced. The new spin-ice compounds are, thus, closer to the phase boundary between spin-ice phase and antiferromagnetically ordered all-in-all-out phase consistent with a reduction of the energy of monopole excitations.

Contents

I. Introduction – frustration and magnetostriction	1
1. Introduction	3
1.1. Motivation	3
1.2. Role of the lattice	4
1.3. Outline of this work	4
2. Theory of magnetostriction	7
2.1. The Hamiltonian of the magnetic system	7
2.2. The complete Hamiltonian of the magnetoelastic system	10
2.2.1. Magnetostriction mechanisms in rare-earth antiferromagnets	10
2.2.2. Equilibrium strain of the magnetoelastic system	12
2.2.3. Numerical simulation of the magnetostrictive effect in the spin-ice pyrochlores using McPhase	13
3. Details of the measurements and samples	17
3.1. Magnetostriction and thermal-expansion measurements with capacitance dilatometers	17
3.1.1. Design and analysis of the tilted-disk cell (TDC)	18
3.1.2. Design and analysis of the tilted-annulus cell (TAC)	19
3.1.3. Magnetostriction and thermal expansion	21
3.2. Background: Spin ice pyrochlores	24
3.2.1. Rare-earth pyrochlores	24
3.2.2. Spin-ice pyrochlores	28
3.2.3. $\text{Dy}_2\text{Ti}_2\text{O}_7$ and $\text{Ho}_2\text{Ti}_2\text{O}_7$	34
3.3. Experimental	35
3.3.1. Samples	35
3.3.2. Magnetostriction, thermal-expansion and lattice-relaxation measurements at $\text{Dy}_2\text{Ti}_2\text{O}_7$ and $\text{Ho}_2\text{Ti}_2\text{O}_7$	36

II. Results and Discussion	43
4. Quasi-static magnetoelastic properties of $\text{Dy}_2\text{Ti}_2\text{O}_7$ and $\text{Ho}_2\text{Ti}_2\text{O}_7$	45
4.1. Introduction: Phase diagrams of $\text{Dy}_2\text{Ti}_2\text{O}_7$ and $\text{Ho}_2\text{Ti}_2\text{O}_7$	46
4.2. Results for $\text{Dy}_2\text{Ti}_2\text{O}_7$	47
4.3. Results for $\text{Ho}_2\text{Ti}_2\text{O}_7$	50
4.4. Simulation of the magnetostriction	52
4.5. Discussion	60
5. Dynamic magnetoelastic properties of $\text{Dy}_2\text{Ti}_2\text{O}_7$ and $\text{Ho}_2\text{Ti}_2\text{O}_7$	67
5.1. Results	67
5.1.1. Results for $\text{Dy}_2\text{Ti}_2\text{O}_7$	68
5.1.2. Results for $\text{Ho}_2\text{Ti}_2\text{O}_7$	77
5.2. Discussion	81
6. Effects of the lattice on the magnetic properties of spin-ice studied via silicon substitution in $\text{Dy}_2\text{Ge}_{2-x}\text{Si}_x\text{O}_7$	83
6.1. Background: Substitution dependence of the magnetic interactions	83
6.2. Experimental	85
6.3. Results	87
6.4. Discussion	93
III. Summary and Outlook	95
IV. Appendix	101
A. Derivation of the formulas for the simulation of the magnetostriction	103
A.1. The mean-field Hamiltonian	103
A.2. The general linear anisotropic stress-strain relation	104
A.3. Perturbation of the magnetoelastic Hamiltonian for small arbitrary and trigonal strains	105
A.4. Free energy of the magnetoelastic system and equilibrium strain	107
A.5. Conversion between sets of elastic constants	108
A.6. Deformation of a tetrahedron in tetragonal strain	109
A.7. Elastic energy in cubic symmetry for tetragonal strain	110
A.8. Crystal field in the pyrochlore lattice	111

A.9. Wave functions of the ground state of of the rare-earth ion in $\text{Dy}_2\text{Ti}_2\text{O}_7$ and $\text{Ho}_2\text{Ti}_2\text{O}_7$	112
B. Derivation of the formulas for the analysis of the magnetostriction and relative expansion data	113
B.1. The general tilted-plate capacitor	113
C. Effective spin-ice model	117
C.1. Low-temperature simple effective model of spin ice	117
C.1.1. Properties of a tetrahedron in a field in $[1\ 1\ 1]$ direction for $\text{Dy}_2\text{Ti}_2\text{O}_7$	119
C.1.2. Properties of a tetrahedron in a field slightly off the $[1\ 1\ 1]$ direction	123
Bibliography	131

Part I.

Introduction – frustration and magnetostriction

1. Introduction

1.1. Motivation

Magnetic frustration is a much investigated concept that was discussed in depth by Anderson [1] in the 1950's. It can be characterized by the ratio between a strong magnetic interaction given by a high Curie-Weiss temperature θ_{cw} and low ordering temperature T_c . The degree of frustration is then given by the frustration parameter f :

$$f = \frac{\theta_{cw}}{T_c}, \quad (1.1)$$

which is high for strongly frustrated magnets, while for unfrustrated systems one usually assumes $f \leq 5$ [2]. In general it is understood that geometrical constraints or disorder can lead to frustration [3]. A prototypical example is the antiferromagnetic Ising magnet with triangular lattice, where the magnetic system cannot minimize its energy with a unique ground state due to the geometrical constraints of the lattice. While the required ingredients for frustration are quite well understood their consequences and emergent phenomena are still subject of current research. On the one hand, frustration is mostly a low-temperature phenomenon and has motivated a broad interest and high effort in fundamental solid state physics at low temperatures. On the other hand, the physics of frustrated magnets stretches over a wide range of magnetic fields from exotic ground states such as spin ice, spin liquids and spin glasses [2] at low fields to strong structural transitions at high fields [4].

Frustration is found in two-dimensional compounds, such as compounds with triangular lattice, as well as in three-dimensional lattices, such as the lattice of corner-sharing tetrahedra [2]. This structure of corner-sharing tetrahedra is realized in spinel compounds with formula AB_2O_4 that host high-field structural transitions [4] and the rare-earth pyrochlores $RE_2B_2O_7$ that realize the disordered ground states called spin ice or spin liquid [5]. The latter are the subject of this work. The whole class of these compounds is large and gives rise to exotic and varied new physics [6]. One of the most interesting phenomenon among these is the emergence of fractional excitations that can be interpreted

as magnetic monopoles [7]. The magnetic monopoles are the excitations out of a ground state that is analogous to the proton configuration in water ice and is, therefore, called the spin-ice configuration [8, 9]. In this work, I investigated the magnetostriction of the spin-ice compounds with their monopole excitations and the dynamics of these monopoles. Recent developments in nanoscale magnetometry have motivated a possible way to investigate these excitations experimentally [10]. Another approach would be the investigation of so called quantum spin ices with excitations that would realize an extended form of electrodynamics [11].

1.2. Role of the lattice

All of these phenomena depend on the specific geometry of the lattice and are expected to be very sensitive to distortions of the lattice. For example, a specific lattice symmetry might lead to a degeneracy of eigenstates of the system; a distortion of the lattice could destroy the symmetry, lifting the degeneracy. Measurements of the lattice properties such as the elastic moduli via ultrasound measurements [12] or the lattice expansion in magnetic fields via dilatometric measurements reveals whether the lattice is an additional degree of freedom of the system that has to be taken into account in theoretical models. In this way, these measurements complement the characterization of a compound by basic measurements of the magnetic properties such as magnetization or ac-susceptibility. In addition to that, measuring the lattice behavior of a compound may reveal phase transitions that would be unobservable by other measurement techniques, either because the range of external conditions (temperature or magnetic field) is not accessible or because it simply is not sensitive to the physics of the compound. There are several possible mechanisms of interaction between the lattice and the magnetic spin configuration [13–15] and the knowledge of which one being dominant for a specific compound can give valuable information for understanding this compound.

1.3. Outline of this work

In the remainder of part I of this manuscript the focus will be put on the following: In chapter 2, I give a short overview on the theory of magnetostriction which is complemented by some derivations in appendix A. In chapter 3, the fundamentals of the magnetostriction measurement and the spin-ice pyrochlores are explained. The equations for the analysis of the magnetostriction and thermal-expansion data are given there and derived in appendix B.

After the introduction, we dive right into the results of my investigations in part II. In chapter 4, the measurements of the quasi-static magnetostriction and thermal expansion are shown and discussed. In chapter 5, the measurements of my experiments with quick field sweeps to probe the monopole dynamics are shown and discussed. In chapter 6, another complementary study is shown where I varied the lattice parameter in order to induce a change of the magnetic properties of the parent compound.

This thesis ends in part III with a summary and an outlook and the appendices follow for the interested reader.

2. Theory of magnetostriction

In this chapter, I introduce a simple mean-field approach to model the magnetostriction in rare-earth compounds solving the Hamiltonian of the electronic system around the rare-earth atom in the crystal-electric field of the crystal and exchange interactions with neighboring ions. First of all, the Hamiltonian in eq. (2.1) of the electronic system around the atomic core of the rare earth ion is explained roughly in section 2.1. In the same section, I describe how the single-ion electronic systems are coupled to each other by introducing the exchange interaction of eq. (2.4) and then solving it in a mean-field approach, eqs. (2.6) and (2.7). In section 2.2, I introduce the coupling of the lattice to the electronic system by making the exchange interaction and the crystal-electric field depend on the strain, eqs. (2.9) and (2.10). The resulting energy difference is balanced with the deformation energy in eq. (2.8) of the crystal to obtain the equilibrium strain in the limit of small deformations, eq. (2.12). This last equation is the main result of this section.

2.1. The Hamiltonian of the magnetic system

The single-ion Hamiltonian The Hamiltonian of a magnetic atom in a crystal is described in detail in [16] and the following explanations are reproduced from there. The single-ion Hamiltonian H_{SI}^i at lattice site i is given by:

$$H_{SI}^i = H_0 + H_1 + H_{SO} + H_{CEF}^i + H_{Ze}, \quad (2.1)$$

with the contributions:

- H_0 is the sum of the Hamilton operators of the N individual electrons (mass m , position r_n) moving in the radial potential V of the positively charged nucleus without mutual interaction between the electrons:

$$H_0 = \sum_{n=1}^N \left(-\frac{\hbar^2}{2m} \Delta_n + V(r_n) \right),$$

2. Theory of magnetostriction

where $\Delta_n = \partial^2/\partial x_n^2 + \partial^2/\partial y_n^2 + \partial^2/\partial z_n^2$ in Cartesian coordinates (x_n, y_n, z_n) of electron n ,

- H_1 is the Hamilton operator of the first perturbation of H_0 by the mutual interaction of the electrons and the screening of the nucleus by the electron close to it:

$$H_1 = \frac{1}{8\pi\epsilon_0} \sum_{n \neq m} \frac{e^2}{r_{nm}} + \frac{1}{4\pi\epsilon_0} \sum_{n=1}^N \left(-\frac{Ze^2}{r_n} - V(r_i) \right),$$

where ϵ_0 denotes the vacuum permittivity, e the elementary charge, r_{nm} the distance between electron n and m , and Z the proton number of the nucleus.

- H_{SO} is the second perturbation Hamiltonian representing the spin-orbit coupling, i.e., the interaction between spin \vec{s}_n and orbital angular momentum \vec{l}_n of the electron n :

$$H_{SO} = \sum_{n=1}^N \zeta(r_n) \vec{l}_n \cdot \vec{s}_n,$$

where ζ denotes the spin-orbit-interaction strength.

- H_{CEF}^i is the perturbation by the effective potential V_c of the electric environment of the ion at lattice site i in the crystal, the so-called crystal electric field:

$$H_{CEF}^i = -|e| \sum_{n=1}^N V_c^i(\vec{r}_n) = \sum_{l=0}^{\infty} \sum_{m=-l}^l B_l^m(i) O_l^m(i), \quad (2.2)$$

where V_c^i is expanded in the Stevens parameters B_l^m and the Stevens operators O_l^m at lattice site i .

- H_{Ze}^i is the Zeeman interaction of the electrons coupling to an effective magnetic moment μ with the external magnetic field \vec{B} :

$$H_{Ze}^i = -\vec{\mu}^i \cdot \vec{B}, \quad (2.3)$$

where the magnetic moment operator reads $\vec{\mu}^i = \mu_B(\vec{L}^i + 2\vec{S}^i)$, with the Bohr magneton μ_B , the total angular momentum $\vec{L}^i = \sum_n \vec{l}_n^i$ and $\vec{S}^i = \sum_n \vec{s}_n^i$.

The Hamiltonian $H_0 + H_1 + H_{SO}$ is the same for each lattice site and its ground state is characterized by two quantum numbers j and m_j denoting the magnitude of the total angular momentum vector \vec{J} and its projection on the z axis. These numbers can be

deduced by the application of the Hund's rules. In general, the ground state is a multiplet whose degeneracy is lifted due to the crystal electric field and the other contributions to the Hamiltonian. The other parts of the total Hamiltonian depend on the lattice site; for that reason they have the superscript i for the lattice site. More details on the various parts of the Hamiltonian can be found in [16].

The magnetic Hamiltonian of the crystal The eigenstates of the single-ion Hamiltonian in the spin-ice pyrochlores $\text{Dy}_2\text{Ti}_2\text{O}_7$ and $\text{Ho}_2\text{Ti}_2\text{O}_7$ are states with fixed total angular momentum $\vec{J} = \vec{L} + \vec{S}$ because of the strong spin-orbit coupling. In the crystal, the angular momentum of nearest-neighbor ions couple to each other via exchange interaction:

$$H_{EX}^i = -\frac{1}{2} \sum_{j \in \text{NN}(i)} J_{ij} \vec{J}_i \vec{J}_j, \quad (2.4)$$

where J_{ij} is the exchange constant between site i and j and \vec{J}_i is the total angular momentum of the ion at the lattice site i . The sum of the Hamiltonians in eq. (2.1) of all single ions and all exchange interactions (eq. (2.4)) between them is used to describe the whole crystal:

$$H_{TOT} = \sum_i (H_{SI}^i + H_{EX}^i). \quad (2.5)$$

This Hamiltonian is the basis of my model of the magnetostriction in the rare-earth compounds $\text{Dy}_2\text{Ti}_2\text{O}_7$ and $\text{Ho}_2\text{Ti}_2\text{O}_7$. This Hamiltonian cannot be solved analytically; that is why I use a mean-field approximation and solve it numerically.

Numerical diagonalization of the magnetic Hamiltonian via McPhase Our goal is to diagonalize the total Hamiltonian (eq. (2.5)). An approximate solution can be found by solving a simpler problem constrained to the unit cell. I use the McPhase software bundle to solve this problem via a mean-field approach [17], which is explained in detail in appendix A.1.

The mean-field Hamiltonian H^{MF} and the mean field $\langle H^s \rangle$ are derived in the appendix eqs. (A.1) and (A.2) and read:

$$H^{\text{MF}} \approx \sum_s \left(H_{SI}^s - \frac{1}{2} \langle \vec{H}^s \rangle \vec{J}^s \right) \quad (2.6)$$

$$\langle \vec{H}^s \rangle = \sum_{i \in \text{NN}(s)} J \langle \vec{J}_i \rangle, \quad (2.7)$$

where J denotes the exchange constant to the nearest neighbors (NN) of the ion at lattice site s of the unit cell, the notation $\langle \cdot \rangle$ denotes the thermal average of the operator between the brackets and $\langle H^s \rangle$ denotes the mean field resulting from the exchange Hamiltonian (eq. (2.4)). In my case, the single-ion Hamiltonian H_{SI}^s is given by eq. (2.1). The index s marks the 16 positions of the ion in the unit cell. The crystal field may vary between for the various s . The ions at different positions s are coupled to each other via the the mean field $\langle H^s \rangle$.

The mean-field ground state is obtained from the diagonalization of eq. (2.6) using eq. (2.1) and a self-consistent mean field eq. (2.7) in the following iterative way. Given an arbitrary initial state sufficiently close to the solution I calculate the mean field for this state using eq. (2.7). The Hamiltonian (eq. (2.6)) is diagonalized giving an updated set of eigenstates and energy levels of each lattice site. At temperature T the thermal expectation value $\langle \vec{J} \rangle$ is calculated using the Boltzmann distribution. The new state is then used as the initial state of the next iteration. This is repeated until the mean field converges to a stable solution. In order to obtain the solution with the global minimal free energy, I compare the free energies of solutions obtained from various initial values using the above iteration method. The result is a self-consistent approximation to the solution of the Hamiltonian (eq. (2.5)) with the minimal free energy, that is some discrete eigenvalues (energy levels) E_i and corresponding eigenvectors (wave functions) ψ_i .

In the next section I discuss how to couple these solutions of the eigenvalue problem of the Hamiltonian to the lattice.

2.2. The complete Hamiltonian of the magnetoelastic system

Having introduced and solved the Hamiltonian of the electronic system of the crystal we now turn to using this solution to estimate the magnetoelastic properties of the lattice. In this section, I review two possible mechanisms of magnetostriction, the crystal-field striction mechanism and the exchange-striction mechanism. I use a perturbation approach to solve the ensuing equations for small deformations of the lattice. In particular, I focus on tetragonal strain modes.

2.2.1. Magnetostriction mechanisms in rare-earth antiferromagnets

Magnetostriction denotes the effect of the magnetic field on the lattice of a crystal, refer to [15] for a review. In order to investigate the magnetoelastic coupling I introduce the

strain tensor ϵ and investigate the properties of the system in the linear limit of small deformations. Using the new degree of freedom the magnetic system can decrease its energy at the expense of the deformation energy of the lattice, given in scientific and Voigt notation:

$$E_{\text{el}}(\epsilon) = \frac{V}{2} \sum_{ijkl} c_{ijkl} \epsilon^{ij} \epsilon^{kl} = \frac{V}{2} \sum_{mn} c_{mn} \epsilon^m \epsilon^n a, \quad (2.8)$$

where V is the volume of the specific area of interest (the crystal or the unit cell), c_{ijkl} is the elasticity tensor and ϵ^{ij} the strain tensor. For the correspondence between scientific and Voigt notation I refer the reader to section A.2 in the appendix. The magnetic system can decrease its energy due to the strain dependence of the exchange interaction and the crystal electric field Hamiltonian.

Exchange mechanism The exchange interaction given in eq. (2.4) depends strongly on the distance between two ions in the lattice. Mostly only nearest-neighbor interactions are taken into account. When the lattice is deformed by a strain ϵ the distance between nearest-neighbor ions changes and, thus, the strength of the interaction. I model this with a strain-dependent exchange constant $J(\epsilon)$ and the exchange interaction is modified in the following way:

$$H_{EX}^i(\epsilon) = -\frac{1}{2} \sum_{j \in \text{NN}(i)} J(\epsilon) \vec{J}_i \vec{J}_j. \quad (2.9)$$

Due to Zeeman interaction H_{Ze} (eq. (2.3)) of the ion with the magnetic field, the \vec{J}_i are aligned parallel pointing into the same direction at high fields $H_{Ze} \gg H_{\text{ex}}$ and $H_{Ze} \gg H_{\text{CEF}}$. In that case, the magnetic system may decrease its energy at the expense of the lattice by deforming and decreasing the unfavorable exchange interaction. Of course, this happens to some degree even at lower magnetic fields. This mechanism is called exchange-striction.

Crystal-field mechanism Since the crystal electric field depends on the local environment of the ion which is deformed by the strain, the crystal-field parameters B_l^m depend on the strain ϵ . Hence, also the crystal-field Hamiltonian H_{CEF} (eq. (2.2)) depends on ϵ :

$$H_{\text{CEF}}^i(\epsilon) = \sum_{l=0}^{\infty} \sum_{m=-l}^l B_l^m(\epsilon, i) O_l^m(i). \quad (2.10)$$

A change of the crystal-field Hamiltonian obviously also changes the ground state and the magnetic state. Conversely, a change of the magnetic state by an increased external magnetic field can make it favorable to distort the lattice at the expense of strain energy to save magnetic energy in the crystal field. The crystal-field striction is important when

the temperature is low enough so that only few crystal field levels are populated and the symmetry of the electronic system of the ion takes on a symmetry compatible with the symmetry of the crystal.

2.2.2. Equilibrium strain of the magnetoelastic system

In the following paragraphs, I put all the ingredients from the last sections together to complete my model of the strain in equilibrium. For this, I use the Hamiltonian above with the strain-dependent exchange and crystal-field striction which add up to the magnetoelastic Hamiltonian. That Hamiltonian is balanced with the elastic energy of the crystal to deduce a formula of the equilibrium strain. This is a hard problem to solve in complete generality; therefore, I constrain myself to a solution of the problem for perturbatively small tetragonal strains with $\epsilon = -\epsilon_1 = -\epsilon_2 = 2\epsilon_3$.

The magnetoelastic Hamiltonian The magnetic system can decrease its energy at the expense of the energy of the lattice. I introduce another degree of freedom in terms of the lattice strain ϵ by adding the elastic energy (eq. (2.8)) to the Hamiltonian and the lattice strain ϵ enters into the magnetic system via the exchange (eq. (2.9)) and the crystal-field striction mechanism (eq. (2.10)) described above. So, in total I modify the Hamiltonian in eq. (2.5) and obtain:

$$H_{TOT}(\epsilon) = \sum_i (H_{SI}^i(\epsilon) + H_{EX}^i(\epsilon)) + E_{el}(\epsilon), \quad (2.11)$$

$$H_{SI}^i(\epsilon) = H_0 + H_1 + H_{SO} + H_{CEF}^i(\epsilon) + H_{Ze}^i.$$

However, there is no way of knowing the exact form of the strain dependence of the exchange interaction and the crystal field. Therefore, I limit myself to perturbatively small strains ϵ ; in this case, a linear strain dependence is sufficient.

Perturbative solution of the magnetoelastic Hamiltonian In the case of perturbatively small ϵ in the tetragonal strain mode I can approximate $H_{TOT}(\epsilon) = H(0) + \delta H$ with:

$$\delta H = \epsilon \sum_i \left(\sum_{l=0}^{\infty} \sum_{m=-l}^l \left[\frac{\partial B_l^m(\epsilon)}{\partial \epsilon} \right]_{\epsilon=0} O_l^m + \sum_{j \in \text{NN}(i)} \left[\frac{\partial J(\epsilon)}{\partial \epsilon} \right]_{\epsilon=0} \vec{J}_i \vec{J}_j + \frac{3}{4} V(c_{11} - c_{12}) \epsilon \right), \quad (2.12)$$

which is derived in the appendix and the result of section A.3. In order to solve this Hamiltonian for perturbatively small ϵ I use first-order perturbation theory. Using the eigenstates of the unperturbed system, I can calculate the equilibrium strain ϵ' in dependence of the magnetic field H and the temperature T . In this first-order approximation the perturbation of the eigenstate does not contribute to the energy. Confining the calculation to the strain of one unit cell with S rare-earth ions, I obtain the equilibrium strain ϵ' via:

$$\epsilon' = -\frac{4}{3V(c_{11} - c_{12})} \sum_{s=1}^S \left(\sum_{l=0}^{\infty} \sum_{m=-l}^l \left[\frac{\partial B_l^m(\epsilon)}{\partial \epsilon} \right]_{\epsilon=0} \langle O_l^m \rangle - \frac{1}{2} \sum_{j \in \text{NN}(s)} \left[\frac{\partial J(\epsilon)}{\partial \epsilon} \right]_{\epsilon=0} \langle \vec{J}_s \vec{J}_j \rangle \right). \quad (2.13)$$

The complete derivation of the formula for the equilibrium strain ϵ' is given in the appendix section A.4.

This equation contains several unknown parameters that have to be filled in either from literature or from own estimations:

- $[\partial B_l^m(\epsilon)/\partial \epsilon]_{\epsilon=0}$ are the magnetoelastic constants of the crystal field and are estimated via the point-charge model.
- $\langle O_l^m \rangle$ is the thermal average of the Stevens operators which I evaluate with McPhase from the solution of the Hamiltonian at zero strain.
- $\langle \vec{J}_s \vec{J}_j \rangle$ is the correlation of the nearest-neighbor spins, which is calculated in a mean-field approach via McPhase.
- c_{ij} are the elastic constants that can be taken from other measurements from the literature.
- $[\partial J(\epsilon)/\partial \epsilon]_{\epsilon=0}$ is the strain derivative of the exchange constant $J_{ij} = J$ and called the magnetoelastic constant of the exchange interaction.

In the next section, I will explain in greater detail how these quantities are determined and how I use McPhase in this problem.

2.2.3. Numerical simulation of the magnetostrictive effect in the spin-ice pyrochlores using McPhase

In the following paragraphs, I explain how I use McPhase to calculate the equilibrium strain given in eq. (2.13). In a first step, I use McPhase to solve the Hamiltonian in eq. (2.11)

at zero strain; that is, I obtain the eigenvalues and wavefunctions of the eigenstates to calculate the thermal averages of the quantities $\langle \vec{J}_i \vec{J}_j \rangle$ and $\langle O_l^m \rangle$ in eq. (2.13). In a second step, I estimate the additional parameters above to evaluate eq. (2.13) using the point-charge module of McPhase for an estimate of $[\partial B_l^m(\epsilon)/\partial\epsilon]_{\epsilon=0}$, while the three other values are free parameters or may be taken from literature. More details on the procedure is given below and an explanation of how McPhase works and can be used can be found in the manual [18].

Thermal averages of the Stevens operators and JJ correlations From the set of crystal-field parameters of the unstrained crystal I calculate the energy scheme and the eigenstates of the Dy ions at specific fields and temperatures using McPhase. These eigenstates and their energies are used to calculate the thermal average values of the observables O_l^m and J_i . For the pyrochlore lattice, O_l^m is non-zero only for $l = 0, 2, 4$ and 6 and $m = 0, \pm 3$ and ± 6 . For the interested reader, the O_l^m can be expressed in terms of the angular momentum operators J and J_z , section A.8. Finally, I can insert these values into the formula of the magnetostriction (eq. (2.13)).

Crystal-field parameters I approximate the magnetoelastic parameter $[\partial_\epsilon B_l^m(\epsilon)]|_{\epsilon=0}$ as difference quotient:

$$[\partial_\epsilon B_l^m(\epsilon)]|_{\epsilon=0} \approx \frac{B_l^m(\epsilon) - B_l^m(0)}{\epsilon}. \quad (2.14)$$

The crystal-field parameters $B_l^m(\epsilon)$ for the pyrochlore lattice (space group $Fd\bar{3}m$) are calculated with the given parameter ϵ assuming point charges at the locations of the ions. At first, for the unstrained lattice and then for the strained lattice with specific tensor ϵ . With the above equation I get another value needed in eq. (2.13).

Elastic constants I use the elastic constants of $\text{Dy}_2\text{Ti}_2\text{O}_7$ and $\text{Ho}_2\text{Ti}_2\text{O}_7$ measured by Erfanifam *et al.* [19]. For the tetragonal strain mode, I need an elastic constant of the form $c_{11} - c_{12}$, which can be expressed in terms of the constants C_{11} , C_L and C_T measured by Erfanifam *et al.* [19]:

$$c_{11} - c_{12} = \frac{1}{2}(c_{11} - c_L + 4c_T), \quad (2.15)$$

which is derived in section A.5.

Exchange parameters Finally, there are two free parameters, $J_{ij} = J$ and $\frac{\partial J}{\partial \epsilon}$, left that are fixed by comparison with my measurements. The latter can be simplified in this way:

$$\frac{\partial J}{\partial \epsilon} = \frac{\partial J}{\partial r_{ij}} \frac{\partial r_{ij}}{\partial \epsilon}, \quad (2.16)$$

with r_{ij} denoting the distance between nearest neighbor ions i and j . As derived in section A.6, I have $\partial r_{ij}/\partial \epsilon = -\frac{1}{2}l$ for site i and j both in the kagome plane and $\partial r_{ij}/\partial \epsilon = +\frac{1}{2}l$ for site i or j in the triangular plane of the apical vertices. The distance between neighboring Dy atoms is given by $\sqrt{2}/4 \cdot a$, which equals 3.58 Å for $a = 10.1240$ Å. I have to choose the free parameter $l \frac{\partial J}{\partial r_{ij}} = l \frac{\partial J}{\partial r}$.

Explicit formula The final formula used for the numerical simulation is then:

$$\begin{aligned} \epsilon' = & -\frac{4}{3V(c_{11} - c_{12})} \left(\sum_{s=1}^4 \sum_{l=0}^6 \sum_{m=-l}^l \left[\frac{B_l^m(\epsilon) - B_l^m(0)}{\epsilon} \right]_{\epsilon=0.01} \langle O_l^m \rangle \right. \\ & - \frac{l}{8} \frac{\partial J}{\partial r} \left[\langle \vec{J}_1 \vec{J}_2 \rangle + \langle \vec{J}_1 \vec{J}_3 \rangle + \langle \vec{J}_1 \vec{J}_4 \rangle + \langle \vec{J}_2 \vec{J}_1 \rangle + \langle \vec{J}_3 \vec{J}_1 \rangle + \langle \vec{J}_4 \vec{J}_1 \rangle \right] \\ & \left. + \frac{l}{8} \frac{\partial J}{\partial r} \left[\langle \vec{J}_2 \vec{J}_3 \rangle + \langle \vec{J}_2 \vec{J}_4 \rangle + \langle \vec{J}_3 \vec{J}_4 \rangle + \langle \vec{J}_3 \vec{J}_2 \rangle + \langle \vec{J}_4 \vec{J}_2 \rangle + \langle \vec{J}_4 \vec{J}_3 \rangle \right] \right). \quad (2.17) \end{aligned}$$

In conclusion of this chapter, I have derived a formula for the equilibrium strain of the electronic system in a magnetic field \vec{H} ; the formula is eq. (2.17). In section 4.4 I use this formula to calculate the magnetostriction of $\text{Dy}_2\text{Ti}_2\text{O}_7$ and $\text{Ho}_2\text{Ti}_2\text{O}_7$.

3. Details of the measurements and samples

This chapter is split in three parts: At first, in section 3.1, I introduce the details of the capacitance dilatometers I used in this study. Then, in section 3.2, I give the necessary general background about the spin-ice materials $\text{Dy}_2\text{Ti}_2\text{O}_7$, $\text{Ho}_2\text{Ti}_2\text{O}_7$ and $\text{Dy}_2\text{Ge}_{2-x}\text{Si}_x\text{O}_7$. For $\text{Dy}_2\text{Ge}_{2-x}\text{Si}_x\text{O}_7$ some more specific background is given in chapter 6 in Part II. Last but not least, in section 3.3 I give the specific details on the experiments I conducted, but the experimental details of the $\text{Dy}_2\text{Ge}_{2-x}\text{Si}_x\text{O}_7$ study are given in chapter 6.

3.1. Magnetostriction and thermal-expansion measurements with capacitance dilatometers

In dilatometric techniques the relative change of length $\Delta L/L$ of a sample is measured [15]; if only the temperature is varied, the thermal expansion is measured, while at constant temperature and varying magnetic field the magnetostrictive effect is measured. In varying temperature the magnetic sample might of course order magnetically and experiences a so called spontaneous magnetostriction, whereas in a varying external magnetic field the magnetostriction is called forced. In general, magnetostriction and thermal expansion are rather small effects and need sophisticated measurement devices to be measurable. Both effects are measured as relative length change $\Delta L/L$ (without unit). Alternatively, magnetostriction may also be characterized as derivative $\alpha_B = d(\Delta L/L)/dB$ (with magnetic flux density B ; unit T^{-1}) and thermal expansion analogously as derivative $\alpha_T = d(\Delta L/L)/dT$ (with temperature T , K^{-1}). Typical magnetostrictive effects are in the order of 10^{-6}T^{-1} , but may be as big as 10^{-3}T^{-1} in special compounds [15]; and thermal expansion is an effect in the order of 10^{-8}K^{-1} to 10^{-5}K^{-1} [14]. In order to measure the small changes of the lattice due to temperature changes or varying the magnetic field various designs of dilatometers were invented, for a review refer to [15] and references therein. Capacitance dilatometers [20–23] measure the relative expansion of a sample as change of the capac-

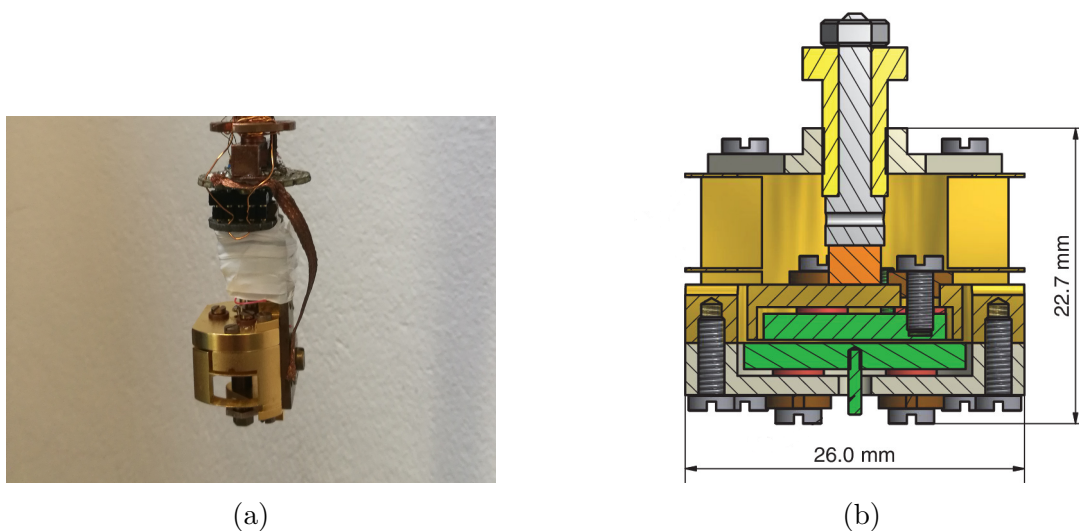


Figure 3.1.: (a) Photograph of the tilted-disk cell (TDC) at the ^3He insert and (b) technical scheme of the TDC with the sample in orange and the capacitor plates in green; based on [23].

ity. They are the most sensitive measurement devices for magnetostriction and thermal expansion with sensitivities up to 10^{-9} in $\Delta L/L$. Therefore, even small thermal-expansion effects at lowest temperatures can be observed. However, they are also sensitive to vibrations and do not lend themselves to pulsed-field measurements for which optical or X-ray methods are better suited [15].

In this work, two capacitance dilatometers, the tilted-disk cell (TDC) and the tilted-annulus cell (TAC), were used to measure the magnetostriction and thermal expansion of $\text{Dy}_2\text{Ti}_2\text{O}_7$ and $\text{Ho}_2\text{Ti}_2\text{O}_7$. In this section, I introduce the two capacitance dilatometers and derive the equations used for the analysis of the raw data.

3.1.1. Design and analysis of the tilted-disk cell (TDC)

The TDC is a commercially available tilted-plate dilatometer with circular capacitor plates described in [23] and displayed in figs. 3.1a and 3.1b. The bottom plate (in fig. 3.1b) is fixed to the frame while the top plate is held by a spring fixed to the frame. The spring is designed to work as a suspension parallelogram that conserves the orientation of the plate even under stress so that the tilting angle is constant and the plate can only move vertically. The sample is located on top of the upper plate and is pressed on it via a screw that is fixed to the frame. The force put on the sample is of the order of 3 N. An expansion of the sample pushes the upper capacitor plate down closer to the bottom one

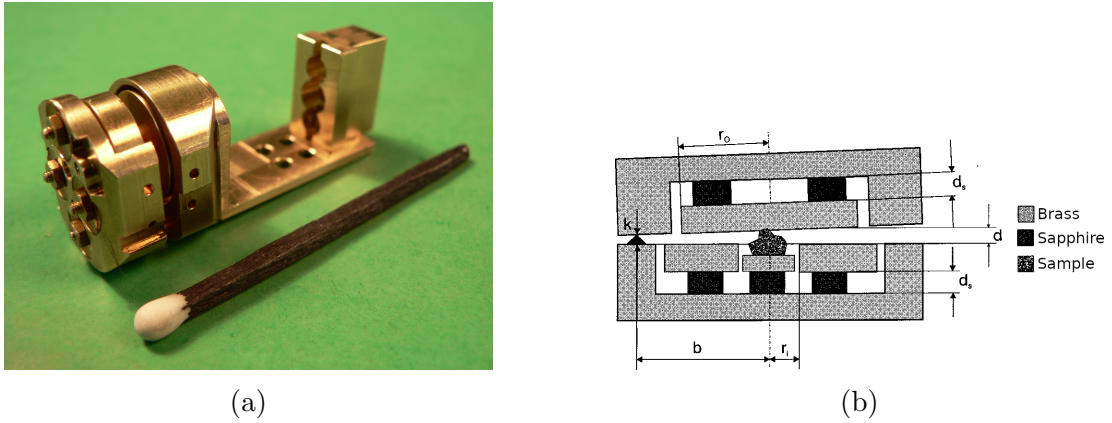


Figure 3.2.: (a) Photograph of the tilted-annulus cell (TAC) and (b) scheme of the TAC (modified on the basis of Ref. [22])

which results in an increase of the capacitance. The TDC is insensitive to magnetoelectric effects, since the sample is located outside of the capacitance plates.

The dependence of the width of the gap between the capacitor plates d on the capacity C for the TDC is derived in the appendix, eq. (B.5). The change of the gap Δd that leads to a change of the capacity from C_1 to C is given in the original publication [23] and derived in detail in appendix B.1; it obeys the following equation:

$$\Delta d = \frac{\epsilon_0 \pi r^2}{C_1 C} (C_1 - C) \left[1 - \frac{C_1 C}{C_{max}^2} \right], \quad (3.1)$$

where ϵ_0 is the dielectric constant of vacuum (ϵ_r being the relative permittivity of the gas atmosphere set to 1 [23]), r the radius of the capacitor plates and C_{max} the short-circuit capacity. While most of these values are specified in the manual, the short-circuit capacity C_{max} has to be measured. The capacitor plates have the radius 7.0(1) mm and the short-circuit capacity $C_{max} = 120(10)$ pF. Mathematically, a resolution of $\Delta l = 3 \times 10^{-12}$ m for $\Delta C = 10^{-6}$ pF at $C = 20$ pF is possible; hence, for samples with a length L_S in the order of millimeter a $\Delta l/l \approx \Delta d/L_S = 10^{-9}$ can be resolved.

3.1.2. Design and analysis of the tilted-annulus cell (TAC)

The TAC is also a commercially available tilted-plate capacitance dilatometer that is described in [22] and displayed in figs. 3.2a and 3.2b. In the TAC both capacitor plates are annulus-shaped; the bottom plate is fixed to the frame and the top plate is fixed to a second frame part which additionally functions as an electrical shielding. The top plate is pressed to the bottom frame via a soft CuBe spring. The sample is put on a sapphire

platelet embedded in the hole of the bottom plate and is pressed on it by the top frame part; there it is situated in the hole of the top plate. The force exerted on the sample is of the order of 50 mN (depending on the thickness, i.e., strength of the spring) and is two orders of magnitude smaller than for the TDC. When the sample expands it pushes the top frame away from the bottom part and increases the distance between the plates; at the same time the tilting of the upper plate changes. In order for the two capacitor plates not to touch, the sample has to have a specific length; if the sample is too small the necessary length may be achieved by sandwiching it between two brass cylinders and if it is too long, it has to be cut.

I simply model the TAC with its annulus-shaped capacitor plates with inner radius r_i and outer radius r_o as the difference of two disk-shaped tilted-plate capacitors with radii r_i and r_o . The dependence of the capacitance C on the gap width d in the center is thus given by the following formula which is also explained in [22]:

$$C = \frac{2\epsilon_0}{d} \left[A_o(T) \frac{1 - \sqrt{1 - \gamma_o^2}}{\gamma_o^2} - A_i(T) \frac{1 - \sqrt{1 - \gamma_i^2}}{\gamma_i^2} \right], \quad (3.2)$$

with A_o and A_i denoting the area of the outer and the inner disk of the annulus and the variables γ_i and γ_o are geometrical parameters of the cell given by:

$$\gamma_{o/i} = \frac{r_{o/i}}{b} \left(\frac{k(T)}{d(T)} - 1 \right),$$

where b is the distance of the middle center of the annulus to the pivot point and k is the height of the pivot point over the bottom capacitor plate; these lengths are displayed in fig. 3.2b. These lengths, as well as the radii r_i and r_o , are temperature dependent due to the thermal expansion of the brass the cell is made of and the sapphire bearings in the cell:

$$\begin{aligned} k(T) &= k(T_0) \left(1 + \left(\frac{\Delta L}{L} \right)_{SL} (T) \right), \\ k(T_0) &= \epsilon_0 \frac{A_o - A_i}{C_0}, \\ A_{o/i}(T) &= \pi r_{i/o}^2 \left(1 + \left(\frac{\Delta L}{L} \right)_{BL} (T) \right)^2, \end{aligned}$$

where C_0 is the capacitance for parallel plates and $(\Delta L/L)_{SL}$ and $(\Delta L/L)_{BL}$ denote the thermal expansion data of sapphire and brass from the literature [24]. Unlike the case of

the TDC the formula for the TAC (eq. (3.2)) cannot be inverted analytically; therefore, I invert it numerically for each measured capacitance C .

The required cell parameters are: $r_o = 6.2$ mm, $r_i = 2.6$ mm, $b = 9.45$ mm and $C_0 = 2.9$ pF. A gap $d = 0.25$ mm corresponds to a capacity of 3.68 F, a value I tried to achieve approximately at room temperature. Mathematically a change of the gap by 5×10^{-8} mm at this capacity would result in a change of the capacity of 10^{-7} pF. For a sample of dimension L_S in the millimeter range a relative expansion of 10^{-8} is detectable.

3.1.3. Magnetostriction and thermal expansion

In the experiments I conduct two different measurements: in the magnetostriction measurements I vary the field while keeping the temperature constant and in the thermal expansion measurements I vary the temperature at constant field.

Magnetostriction For the case of the magnetostriction measurement the relative expansion $\frac{\Delta L}{L}$ of the sample can be related to the change of the gap width Δd since both, TDC and TAC, were designed to have minimal magnetostrictive effects of the cell material [22, 23]. Therefore, I use the following formula for the analysis of the magnetostriction data:

$$\frac{\Delta L}{L} = \frac{\Delta d}{L_S}, \quad (3.3)$$

where L_S is the sample length. Depending on which dilatometer cell is used for the measurement, I have to calculate Δd with eq. (3.1) or eq. (3.2) for the TDC or the TAC, respectively.

Thermal Expansion The thermal expansion has to be more thoroughly analyzed because the expansion of the cell material is of the same order of magnitude as the investigated materials and will lead to incorrect results if not corrected for. Therefore, in preparation of the actual measurements, the gap change that is caused by the thermal expansion Δd_{Cell} of the dilatometer cell has to be determined. This is done by measuring a brass sample of length L_{Br} with known thermal expansion $(\Delta L/L)_{Br}$ (shown in fig. 3.3). The difference between the expected gap change due to the thermal expansion of the brass sample and

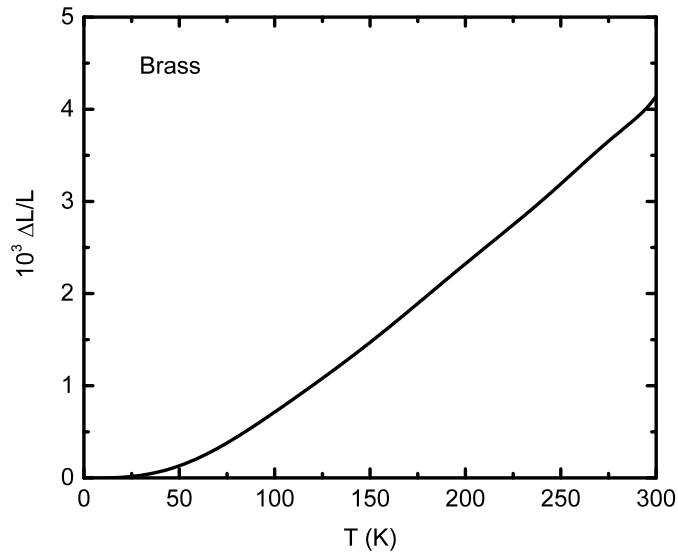


Figure 3.3.: Temperature dependence of the relative length change $\Delta L/L$ of copper used for the background determination of the thermal-expansion measurements, data taken from [24].

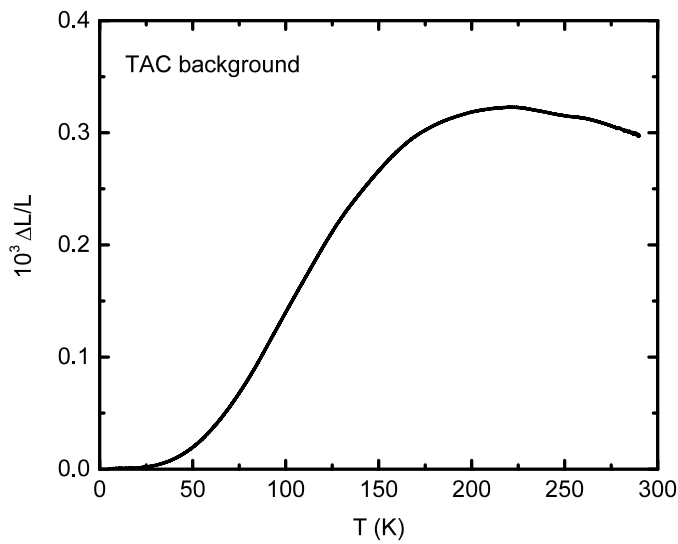


Figure 3.4.: Background of the TAC in thermal-expansion measurements.

the measured gap change Δd is the cell signal. With these considerations the identities can be deduced:

$$\begin{aligned}\Delta d &= \Delta d_{\text{Br}} + \Delta d_{\text{Cell}}, \\ \Delta d_{\text{Cell}} &= \Delta d - \Delta d_{\text{Br}} = \Delta d - L_{\text{Br}} \left(\frac{\Delta L}{L} \right)_{\text{Br}}.\end{aligned}\quad (3.4)$$

The cell effect of the TAC is shown in fig. 3.4. The TDC was used only for measurements for temperatures below 2 K where cell effects are negligible; the cell effects are described in Ref. [23].

In the actual measurements, I tried to reproduce the same initial gap as in the preparatory measurement above to ensure that the measurements are made under comparable conditions. The sample with length L_S is sandwiched between brass pieces of total length L_{BrS} such that their combined length is approximately the length L_{Br} of the brass piece in the preparatory measurement, i.e., $L_S + L_{\text{BrS}} \approx L_{\text{Br}}$. The gap change Δd is comprised of three contributions: the expansion of the sample Δd_S , the expansion of the brass pieces Δd_{BrS} and the cell signal Δd_{Cell} :

$$\Delta d_{\text{prep}} = \Delta d_S + \Delta d_{\text{BrS}} + \Delta d_{\text{Cell}}. \quad (3.5)$$

In eq. (3.5), I substitute Δd_{Cell} for the expression given in eq. (3.4) and deduce the formula for the gap change caused by the expansion of the sample:

$$\Delta d_S = \Delta d - \Delta d_{\text{prep}} + (L_{\text{Br}} - L_{\text{BrS}}) \left(\frac{\Delta L}{L} \right)_{\text{Br}}. \quad (3.6)$$

The relative thermal length change of the sample $(\Delta L/L)_S$ is then given by dividing eq. (3.6) by the sample length L_S :

$$\left(\frac{\Delta L}{L} \right)_S = \frac{\Delta d_S}{L_S} = \frac{\Delta d}{L_S} - \frac{\Delta d_{\text{prep}}}{L_S} + \frac{L_{\text{Br}} - L_{\text{BrS}}}{L_S} \left(\frac{\Delta L}{L} \right)_{\text{Br}}. \quad (3.7)$$

This is the equation that is used throughout Part II to analyze the thermal-expansion measurements.

It should be mentioned that eq. (3.7) is slightly different from the equations given in [22] and [25] for the thermal expansion in the TAC. The dilatometer cells used in the two

publications have a slightly different design and the formulas differ accordingly; I use the design from [25]. The thermal expansion of the sample is calculated in [22] via:

$$\left(\frac{\Delta L}{L}\right)_s = \frac{\Delta d}{L_S} - \frac{\Delta d_{\text{prep}}}{L_S} + \left(\frac{\Delta L}{L}\right)_{\text{Br}}. \quad (3.8)$$

It can be seen that eq. (3.7) equals eq. (3.8) if $L_{\text{Br}} - L_{\text{BrS}} = L_S$, i.e., when the length of the brass sample in the “empty” cell has the same length as the actual sample plus the brass spacers. In general, this cannot be achieved exactly; moreover, the contribution of this term becomes more important when the sample is very thin.

The detailed specifics of the measurements are given in section 3.3 after an overview of the compound class my samples belong to in the following section.

3.2. Background: Spin ice pyrochlores

In this section, I give a brief overview on the spin-ice compounds and put them into context with related materials.

3.2.1. Rare-earth pyrochlores

The spin-ice pyrochlores belong to the class of rare-earth compounds with the pyrochlore lattice structure and the general chemical formula $A_2B_2O_7$. This class consists of combinations of trivalent ions at the A site and tetravalent ions at the B site [6], see fig. 3.5. However, not all combinations of A and B ions can be prepared in the pyrochlore structure under low-pressure conditions; a ratio of the ionic radii R_A/R_B between 1.36 and 1.71 has been found to be stable [6, 27, 28]. This region of stability can be extended if high hydrostatic pressures are applied during the crystal synthesis [26] and even pyrochlores with a ratio $R_A/R_B = 1.94$, e.g., $\text{Dy}_2\text{Ge}_2\text{O}_7$, can be grown [29, 30].

Lattice structure The pyrochlore structure consists of two interpenetrating sublattices of corner-sharing tetrahedra of the A and the B site, respectively; see fig. 3.6. Sometimes the term pyrochlore is also used to only mean a single one of these sublattices instead of both of them. The symmetry of $A_2B_2O_7$ is cubic and the point group of the lattice is $Fd\bar{3}m$. The coordination of the ions on the two sublattices is different as is expected from their oxidation states. The A site is eight-fold coordinated with oxygen, while the B site is six-fold coordinated with oxygen [32]. The oxygen cage around the A site is made up of a ring of six oxygen ions (O) around A and two oxygen ions (O') above and below the

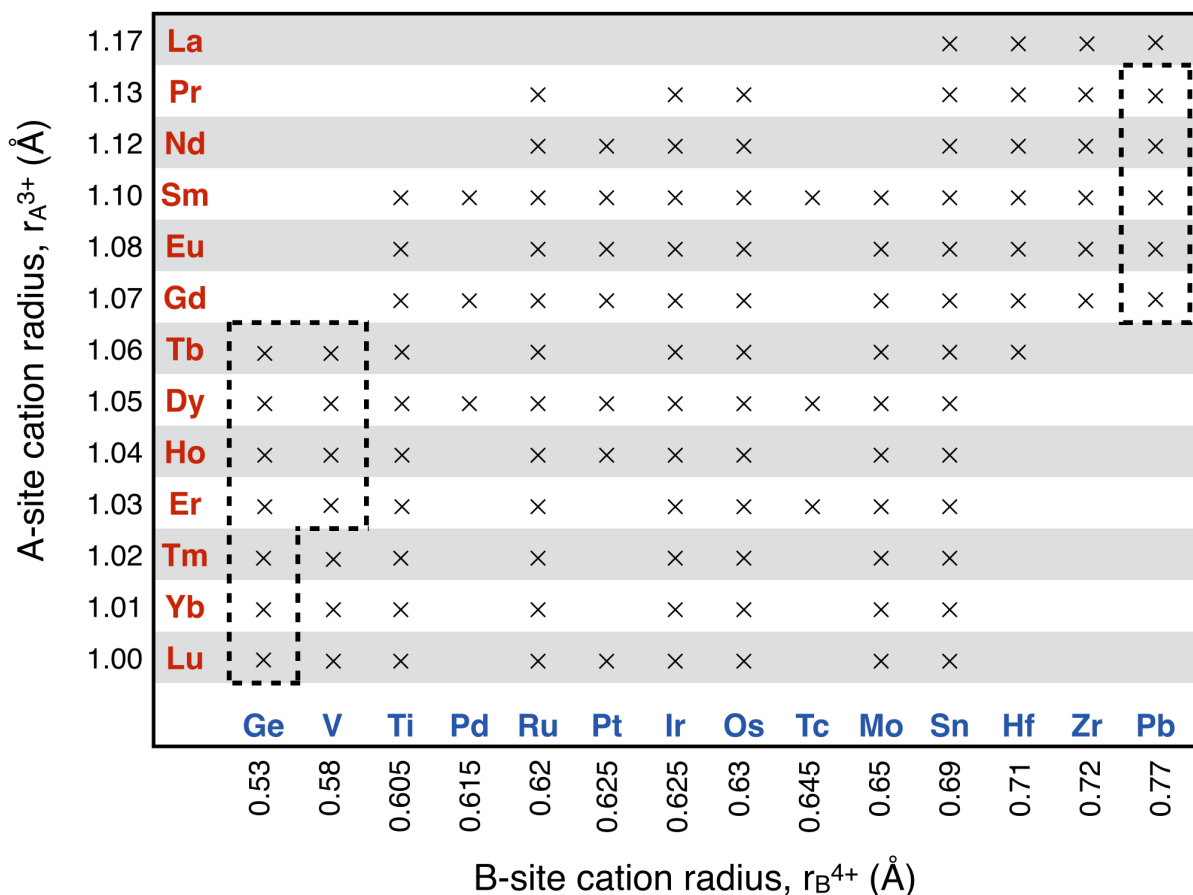


Figure 3.5.: Possible combinations of trivalent A site ions and tetravalent B site ions that form $A_2B_2O_7$ with corresponding ionic radii r_A and r_B , respectively. The combinations that are stable only after high-pressure synthesis are enclosed in dashed lines. Reproduced from [26].

rare earth on the A site. This results in a large axial symmetry of the crystal-electric field influencing the ground state of the rare-earth ion. Depending on the specific ground state of the rare-earth ion on the A site this axial symmetry leads to an easy-axis anisotropy along or an easy-plane anisotropy perpendicular to the local $[111]$ axis. This local $[111]$ axis differs between the four rare-earth positions of a tetrahedron leading to non-collinear magnetic moments. Specifically, the axes are $[111]$, $[\bar{1}11]$, $[1\bar{1}1]$ and $[11\bar{1}]$. Depending on the combination of A and B site atoms the lattice parameter and the positional parameter x change. For example, for the same B -site ion, the lattice parameter is expected to become larger for rare-earth ions with smaller atomic number Z corresponding to larger ionic radii which is also seen in experiment [32].

The $[111]$ axis goes through the center of the tetrahedron to one of its vertices and is aligned with the Ising axis of the spin at this vertex. Besides the $[111]$ axis there are two

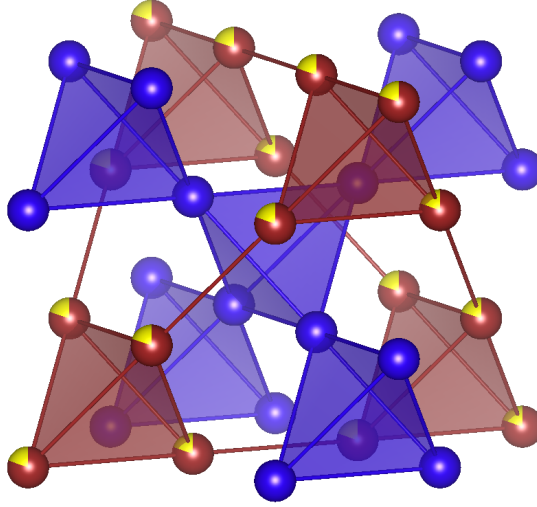


Figure 3.6.: Structure of the pyrochlore lattice: the A site is occupied by the trivalent rare-earth ion (shown as blue spheres) and the B site is occupied by a tetravalent ion such as Ti^{3+} or Ge^{4+} possibly partially substituted by a second kind of tetravalent ion such as Si^{4+} (shown as red spheres with a yellow segment); the oxygen ions are omitted. Reproduced from [31].

Table 3.1.: Positions of the atoms in a unit cell of $A_2B_2O_7$, [32].

Atom	Wyckoff notation	x	y	z
A	16d	$1/2$	$1/2$	$1/2$
B	16c	0	0	0
O	48f	x	$1/8$	$1/8$
O'	8b	$3/8$	$3/8$	$3/8$

other high symmetry axes: $[100]$ and $[110]$. The $[110]$ axis points along the straight line connecting two vertices of a tetrahedron and is perpendicular to the line connecting the other two vertices, while the $[100]$ axis directs through the center of the tetrahedron and is perpendicular to two opposite sides of it. The plane perpendicular to $[111]$ contains $[11\bar{2}]$ and is also interesting as it splits the direction space into positive and negative $[111]$ direction.

Magnetic state of the rare-earth ions The magnetic properties of the pyrochlores with non-magnetic Ti on the B site depend only on the magnetic state of the rare-earth ions on the A site. As discussed in chapter 2, the Hamiltonian of the single ion is governed by the Coulomb interactions between electrons H_C , the spin-orbit coupling H_{SO} and crystal-electric field H_{CF} . For the $4f$ electrons of the rare-earth atoms, the Coulomb repul-

sion term dominates the spin-orbit coupling which is bigger than the crystal-electric field: $H_C \gg H_{SO} \gg H_{CF}$. Therefore, the LS-coupling scheme in the Russel-Saunders (RS) approximation is appropriate to describe the ground state on which the crystal field acts as a perturbation. I refer the reader to Ref. [16] or the review [33] which gives an in-depth overview of the physics of f -electron systems. The ground states of the rare-earth ions in vacuum are text-book knowledge [34] and the whole spectrum of states for LS-coupling is also known [35]. Notable special cases are Gd^{3+} with only spin-momentum that may realize a Heisenberg system and Eu^{3+} having a total angular momentum of 0. The Stevens factors α , β and γ give information about how the magnetic moment of the ion is oriented with respect to the electronic charge cloud. Especially, an $\alpha < 0$ is characteristic of an axial anisotropy, an $\alpha > 0$ of an planar anisotropy and $\alpha = 0$ denotes the isotropic case. The values of α were calculated by Stevens for the trivalent rare-earth ions [36]. I would expect Gd to follow an isotropic Heisenberg Hamiltonian; Pm, Sm, Er, Tu and Yb should have planar anisotropy; Ce, Pr, Nd, Tb, Dy and Ho should be axial anisotropic. Indeed, in the pyrochlore lattice with Ti on the B site, Gd realizes an isotropic Heisenberg system; planar systems are realized with Er and Yb and easy-axis systems with Tb, Ho and Dy on the A site [5, 6].

Ground state of the rare-earth ion in the pyrochlore lattice The rare-earth ions in the pyrochlore lattice sit in a position with a trigonal lattice symmetry of D_{3d} [37]. In this symmetry, the crystal field has only six independent components: B_2^0 , B_4^0 , B_4^3 , B_6^0 , B_6^3 and B_6^6 [16]. The expectation values of the operators are tabulated [36, 38, 39]. The relative strength of the contributions of the Stevens operators is determined by the actual crystal field parameters B_l^m given in [40] or can be calculated with a point-charge model. The crystal field parameters of the rare-earth titanium pyrochlores are given in [40–42] and explicitly given in chapter 4 in Part II.

The oxygen around the rare-earth ions create a strong crystal field inducing a strong axial anisotropy. The pyrochlores with Yb and Er have planar character, while those with Ho, Dy and Tb have axial character. The magnetic moment may only point in or out of its tetrahedron for the three latter cases.

In the following, I am interested in the easy-axis systems with Dy and Ho in the titanate and germanate pyrochlores which exhibit the spin-ice ground state.

Interactions between rare-earth ions The reference [43] gives an overview of all possible exchange interactions between f -electron systems such as the rare-earth ions. The most general linear exchange Hamiltonian between nearest neighbors is the bilinear functional:

$$H_{\text{EX}} = \frac{1}{2} \sum_i \sum_{j \in \text{NN}(i)} \vec{J}_i J_{ij} \vec{J}_j, \quad (3.9)$$

with \vec{J} and J_{ij} denoting the three dimensional total-angular momentum operator and the exchange matrix, respectively. This Hamiltonian may be transformed such that each \vec{J} is in its own local coordinate frame corresponding to its site symmetry and its crystal field. In the pyrochlores, this frame is chosen such that the local z axis points along the local $[1\ 1\ 1]$ direction and the Hamiltonian takes a much simpler form given in [44–46]. In this formulation the angular-momentum operator \vec{J}_i is expressed by its local z component J_i^z (in its local $[1\ 1\ 1]$ direction) and the ladder operators J_i^+ and J_i^- that increase or decrease J_i^z by 1, respectively. The exchange coupling between the z components of the angular momentum of the two ions leads to classical effects such as ferromagnetic or antiferromagnetic ordering. The other exchange constants induce quantum effects, see [11] for a review. There are several symmetry constraints for the components of J_{ij} that reduce the number of independent components from 9 to 4. Further constraints arise from whether the ion is Kramers or non-Kramers: In the latter case, the coupling between J_i^z and J_j^+ or J_j^- and vice versa are zero, and in the former they may be non-zero [46]. The spin-ice model is the one with only non-zero exchange between local z components of \vec{J} and will be explained later on. Apart from this (classical) spin-ice model, other cases of the above Hamiltonians were studied finding quantum-spin-ice ground states [44, 46–49].

Possible interactions that could result in the effective Hamiltonian above are the dipolar interactions, superexchange between rare-earth ions via oxygen, direct exchange [33]. In the case of $\text{Dy}_2\text{Ti}_2\text{O}_7$ and $\text{Ho}_2\text{Ti}_2\text{O}_7$, these produce mostly interactions between local z components of \vec{J} in the order of 1 K and suppress all other couplings to orders of a few mK [50]. This is not the case for the $\text{Tb}_2\text{Ti}_2\text{O}_7$ pyrochlore which might be the reason why it is not a classical spin ice.

3.2.2. Spin-ice pyrochlores

In the following paragraphs I give a basic overview on the spin-ice physics, in particular, the various spin-ice models, the physics of this theoretical model and the realization of it in $\text{Dy}_2\text{Ti}_2\text{O}_7$ and $\text{Ho}_2\text{Ti}_2\text{O}_7$. The interested reader may check [51] for a very nice and basic

explanation of the spin-ice model. For reviews on the experimental and the theoretical perspective, see [5, 6, 52] and [8, 9], respectively.

Spin ice model The spin-ice model [53] is effectively given by an antiferromagnetic Ising Hamiltonian:

$$H = -J_{\text{nn}} \sum \vec{S}_i \vec{S}_j, \quad (3.10)$$

with the sum going over all pairs of nearest neighbors, J_{nn} denoting the exchange coupling and \vec{S}_i the spin at site i pointing along its local $[111]$ axis into or out of a specific tetrahedron. However, this model neglects the strong dipolar interaction present between rare-earth ions with large magnetic moments. Therefore, an important modification of this model is the inclusion of long-range dipolar interactions [54] leading to the famous dipolar-spin-ice model:

$$H = -J_{\text{nn}} \sum \vec{S}_i \vec{S}_j + Dr_{\text{nn}}^3 \sum_{j>i} \frac{\vec{S}_i \vec{S}_j}{|r_{ij}|^3} - \frac{3(\vec{S}_i \cdot \vec{r}_{ij})(\vec{S}_j \cdot \vec{r}_{ij})}{|r_{ij}|^5}, \quad (3.11)$$

where r_{nn} is the distance between nearest neighbors and \vec{r}_{ij} is the distance vector between the spin at site i and its nearest neighbor at site j . The strength of the dipolar interaction D is given by,

$$D = (\mu_0/4\pi) \frac{g^2 \mu^2}{r_{\text{nn}}^3}, \quad (3.12)$$

where μ_0 is the vacuum permeability and $g\mu = 10 \mu_B$ for Dy^{3+} and Ho^{3+} ions. Truncating the dipolar interaction to nearest neighbors only gives an exchange-like term with a pseudo exchange constant D_{nn} [54]:

$$D_{\text{nn}} = \frac{5D}{3}. \quad (3.13)$$

More recent models use exchange interactions beyond nearest neighbors (such as next-nearest and next-to-next-nearest neighbors) [55]. However most of the experimental observations can be explained with the spin-ice or dipolar-spin-ice model given above.

The dumbbell model The biggest theoretical achievement was to reformulate the spin-ice Hamiltonian above in terms of magnetic monopole excitations via a so called dumbbell model [56]. The spins at the vertices are effectively dipoles that can be interpreted as compounds of two magnetic charges q , one positive and one negative. Depending on whether the spins point into or out of a specific tetrahedron a positive or the negative charge is in that tetrahedron. Therefore, with four spins at the vertices of each tetrahedron, four charges are in each tetrahedron adding up to a total charge Q of a tetrahedron. The

Table 3.2.: Overview of the excitations in the spin-ice model and their interpretation in the dumbbell model

Spin-ice model	Dumbbell model
2-in-2-out	vacuum
3-in-1-out	monopole with charge +1
3-out-1-in	monopole with charge -1
all-in	monopole with charge +2
all-out	monopole with charge +2

total charge Q may take integer values between -2 and $+2$ (table 3.2). The reformulation of the spin-ice model into this dumbbell picture is given by:

$$H = \frac{\mu_0}{4\pi} \sum_{\alpha < \beta} \frac{Q_\alpha Q_\beta}{r_{\alpha\beta}} + \frac{v_0}{2} \sum_{\alpha} Q_\alpha^2, \quad (3.14)$$

where α and β denote the number of the tetrahedron, μ_0 is the vacuum permeability, $Q_\alpha = \sum_{i \in V(\alpha)} q_i$ with $V(\alpha)$ being the vertices of the α 'th tetrahedron and q_i the charge of the dumbbell at vertex i at the center of the tetrahedron, $r_{\alpha\beta}$ denotes the distance between the centers of tetrahedron α and β and v_0 is the on-site Coulomb interaction. The configuration of two spins pointing in and two spins pointing out leads to $Q = 0$ for the tetrahedron while all other configurations lead to non-zero Q either ± 1 or ± 2 . These non-zero charged tetrahedra can be interpreted as magnetic monopoles with positive or negative charge 1 or 2. The dipolar interaction between the spins translates to the Coulomb interaction between these magnetic monopoles. More details of the dumbbell model can be found in the review [9] and table 3.2 contrasts the excitations in the two models against each other.

The spin-ice ground state For each tetrahedron there are 16 possible spin configurations, shown in fig. 3.7. The six so-called spin-ice configurations at the bottom of the figure are those with two magnetic moments pointing into and two magnetic moments pointing out of each tetrahedron, the 2-in-2-out configuration. These configurations are called spin-ice configurations because they resemble the configuration of hydrogen around oxygen in water ice [5]: The oxygen atoms are at the center of tetrahedrons of hydrogen. Two of the hydrogen atoms are closer to the center of one tetrahedron while the other two are a bit further away, the 2-in-2-out rule. In the spin-ice model, each of these six configurations has the same energy for ferromagnetic interaction between nearest-neighbor magnetic moments and are thus degenerate at zero temperature. This leads to a residual zero-point entropy [57]. The other ten configurations of magnetic moments on the pyrochlore lattice are eight

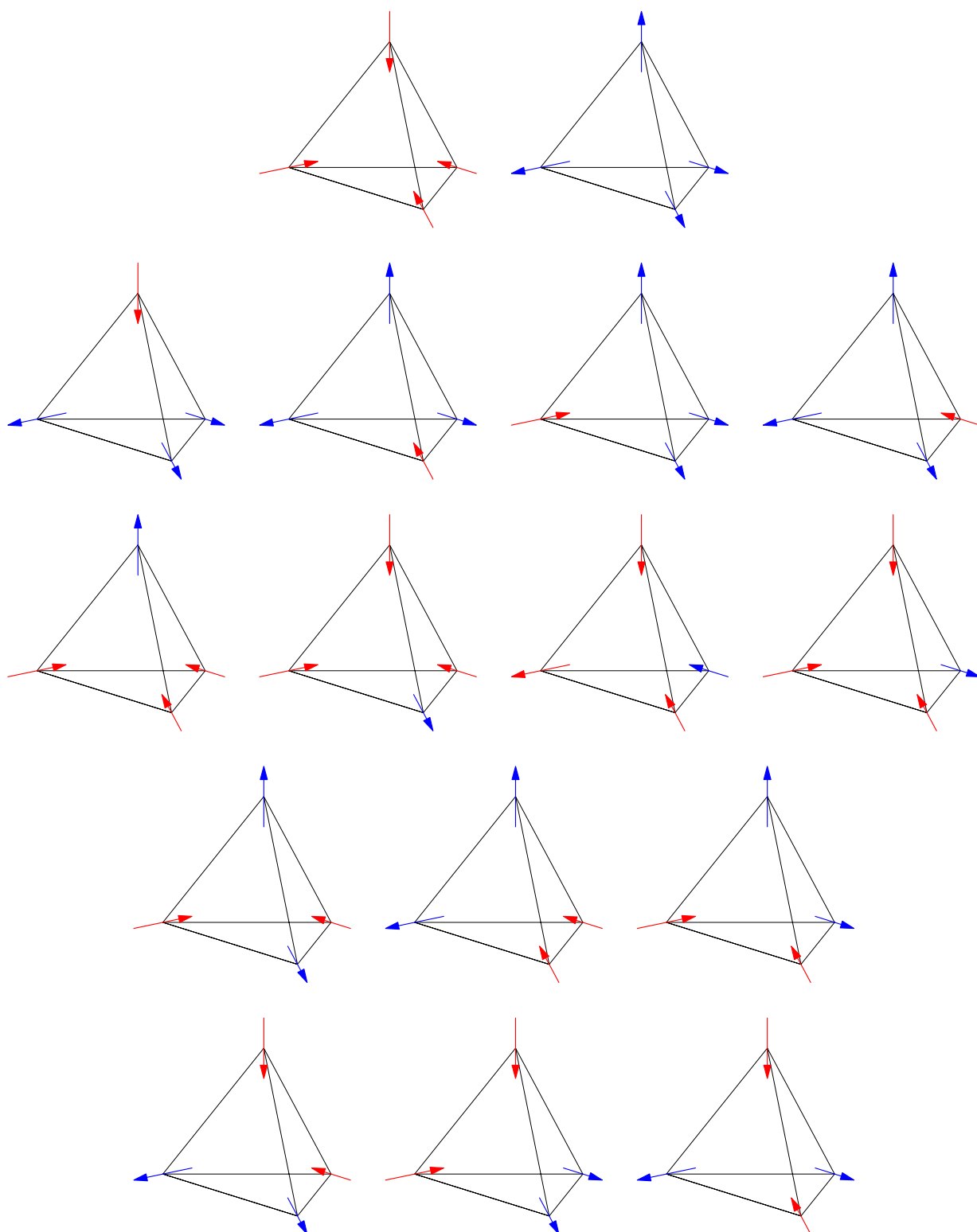


Figure 3.7.: The configurations of the magnetic moments with local Ising axes on the vertices of a tetrahedron. Top row: 4-in and 4-out, second row: four 3-out-1-in, third row: four 3-in-1-out, fourth and fifth row: six 2-in-2-out configurations.

configurations with only one magnetic moment pointing in or out and three pointing out or in, respectively, called the 3-in-1-out or 1-in-3-out configurations; and two configurations with all magnetic moments pointing into or out of the tetrahedron, called the all-in and all-out configurations. The energy gap between the 2-in-2-out to the 3-in-1-out or 3-out-1-in state is $2J$ and needs one spin flip and to the all-in or all-out is $6J$ and needs two spin flips. At high enough temperatures these higher-energy configurations are excited. Compared to the zero influx-outflux balance of the spin-ice state, the 3-in-1-out configuration has positive influx balance and can be interpreted as a sink of the magnetic field, i.e., a negative magnetic monopole, and the 3-out-1-in configuration has a negative influx balance being interpreted as a source of the magnetic field, i.e., a positive magnetic monopole. These excitations can be interpreted as magnetic monopoles in the dumbbell model.

Field along $[1\ 1\ 1]$ direction The magnetization for a field along the $[1\ 1\ 1]$ direction was investigated for the spin-ice model [58, 59]. The $[1\ 1\ 1]$ direction is parallel to one of the four spins in each tetrahedron, the apical spin. At zero field, all of the six spin-ice configurations have the same energy. For a small field along $[1\ 1\ 1]$, the apical spin of each tetrahedron flips in direction of the field to minimize Zeeman energy. However, one of the spins at the base of the tetrahedron has to flip to compensate the top spin and achieve the spin-ice configuration that minimizes the exchange energy. For higher fields, when the Zeeman energy exceeds the exchange energy, also the spins at the base are flipped so that all of them have a positive projection on the magnetic field vector. At this high field, each tetrahedron is in either the 3-in-1-out or the 3-out-1-in configuration. Tetrahedra in one layer perpendicular to $[1\ 1\ 1]$ are in one of these two configurations alternating from layer to layer. In the monopole picture of the dumbbell model, the magnetic field in $[1\ 1\ 1]$ direction translates into a staggered chemical potential for monopoles and antimonopoles on planes with up-pointing and down-pointing tetrahedra, respectively.

Theory asserts that for a nearest-neighbor spin-ice model the first-order transition between low- and high-field phase would be absent at low temperatures and only a second-order transition would be found [56]. In the dipolar-spin-ice model, such a transition is possible and was found numerically [56].

This concludes the explanation of the static properties of the spin-ice model and in the last paragraph of this overview I discuss the dynamical aspects of the spin-ice models.

Dynamics The dynamics of the spin-ice models have been studied in several publications: the equilibrium dynamics in the kagome-ice phase was investigated in terms of the nearest-neighbor spin-ice model [58], the equilibrium dynamics at zero field in terms of

the monopole picture of the dumbbell model [60] and out-of-equilibrium after thermal quenches [61] or after field quenches [62] in the dipolar-spin-ice model. In the following, I will explain the microscopic picture of what happens after thermal and field quenches in the spin ice based on the last two publications.

Temperature quenches have theoretically been proposed and investigated for their unusual dynamics and to probe the dynamics of the monopoles. Firstly note, that at zero field the spin-ice configurations are the lowest-energy state. This state is only stabilized by the exchange interaction between nearest-neighbors. Excitations of this ground state are tetrahedra with 3-in-1-out, 3-out-1-in, 4-in and 4-out configurations that are possible at higher temperatures. When the temperature is reduced quickly the monopoles of the high-temperature many-excitation state have to annihilate before reaching the low-temperature few-excitation state. The dynamics of this process were studied in [61] and the results are stated in the following. The monopole annihilation is efficient and fast only when the monopole density is high. As soon as the monopoles become sparse it is likely that a monopole-antimonopole pair binds together to form a so-called non-contractible pair. Non-contractible pairs are a monopole and an antimonopole sitting on adjacent tetrahedra that create two doubly charged monopoles when the spin between them is flipped. Therefore, this spin flip is energetically forbidden and several other spin flips are needed to annihilate them. However, due to the Coulomb interaction of their magnetic charges they cannot move away from each other without increasing their potential energy. The fastest way of annihilation is that they go along a loop around the plaquette that they are part of. However, then their distance to each other and their mutual Coulomb potential grow, which is energetically not favorable. The energy needed for this is in the order of 1.5 K and is, therefore, highly unfavorable at low temperatures. However, in order to see this slow annihilation dynamics the monopole density must not be too small. Such a high monopole density can only be obtained at low temperatures if the cool down from the monopole-rich high-temperature phase is done quickly. The time scale needed for the cooling is in the order of 100 ms, which is difficult to achieve experimentally. Therefore, temperature quenches are not the first option to probe the monopole dynamics in experiment. It is possible, to achieve a very similar situation when quenching a high magnetic field in $[1\ 1\ 1]$ direction down to zero field.

As explained before, in the case of magnetic field in $[1\ 1\ 1]$ direction the high-field phase of the spin-ice model is a long-range ordered phase: a lattice of alternating monopoles and antimonopoles. It is saturated at each lattice site (the centers of the tetrahedra) occupied by either a magnetic monopole or antimonopole. In contrast to the situation at high temperatures and zero field where the monopoles and antimonopoles are randomly distributed,

in the high-field phase monopoles and antimonopoles are sitting in adjacent tetrahedra and the annihilation should be very efficient. In the low-field phase (spin-ice and kagome-ice phase) there are only few thermally excited magnetic monopoles. This is analogous to the situation of the thermal quenches discussed above, but field quenching is much easier to perform than thermal quenching. Quenching from the high-field monopole-rich into the low-field monopole-poor phase monopoles and antimonopoles have to annihilate. The dynamics of this process were investigated numerically by Mostame *et al.* [62] and their results are briefly explained in the following. They identified three regimes of monopole dynamics, two of which are relatively quick depending on the temperature. The third one is dominant and reaches long time scales of 1000 s and above at low temperatures. At short time scales monopole annihilation between nearest neighbors is dominant followed by a diffusion-annihilation process. In the third regime monopole and antimonopole pairs form non-contractible pairs as after a thermal quench.

The monopole-annihilation process following a field quench is an interesting axis for the discussion of the results of my lattice-relaxation experiments. With this, I conclude the review of the theoretical basics of the spin-ice model and I briefly make a connection of this model to the real materials $\text{Dy}_2\text{Ti}_2\text{O}_7$ and $\text{Ho}_2\text{Ti}_2\text{O}_7$ in the next section.

3.2.3. $\text{Dy}_2\text{Ti}_2\text{O}_7$ and $\text{Ho}_2\text{Ti}_2\text{O}_7$

The review article [8] gives a very good overview on the measurements done on $\text{Dy}_2\text{Ti}_2\text{O}_7$ and $\text{Ho}_2\text{Ti}_2\text{O}_7$ and describes how these compounds were characterized as spin ice. The main features are stated in the following: strong frustration as large ratio of Curie-Weiss temperature (1.2 K for $\text{Dy}_2\text{Ti}_2\text{O}_7$ [63] and 1.8 K for $\text{Ho}_2\text{Ti}_2\text{O}_7$ [64]) and ordering temperature (below 0.06 K for $\text{Dy}_2\text{Ti}_2\text{O}_7$ [63] and below 0.35 K for $\text{Ho}_2\text{Ti}_2\text{O}_7$ [65]); magnetic anisotropy [63, 66] and magnetization plateau [67, 68] characteristic for spin-ice compounds; residual spin-ice entropy [69, 70]; strong axial anisotropy of the crystal field and the large gap to the first excited crystal-field level of 230 K [42]; pinch points in neutron diffraction [71, 72] that are characteristic of the spin-ice phase [9]. It is the strong crystal field that makes $\text{Dy}_2\text{Ti}_2\text{O}_7$ and $\text{Ho}_2\text{Ti}_2\text{O}_7$ to be well described by the spin-ice model (eq. (3.10)), as was shown in [50]. In fact, most experimental observations are captured by this simple model [52, 73]. The dipolar-spin-ice model describes the equilibrium dynamics of the spin-ice ground state [60] and long-range correlations [9] visible as pinch points in neutron-diffraction experiments. In the dipolar-spin-ice model, a long-range ordered ground state at around 0.18 K is predicted [74] that has not yet been found experimentally, possibly due to the spin freezing below 0.5 K. In summary, the (dipolar) spin-ice model describes well

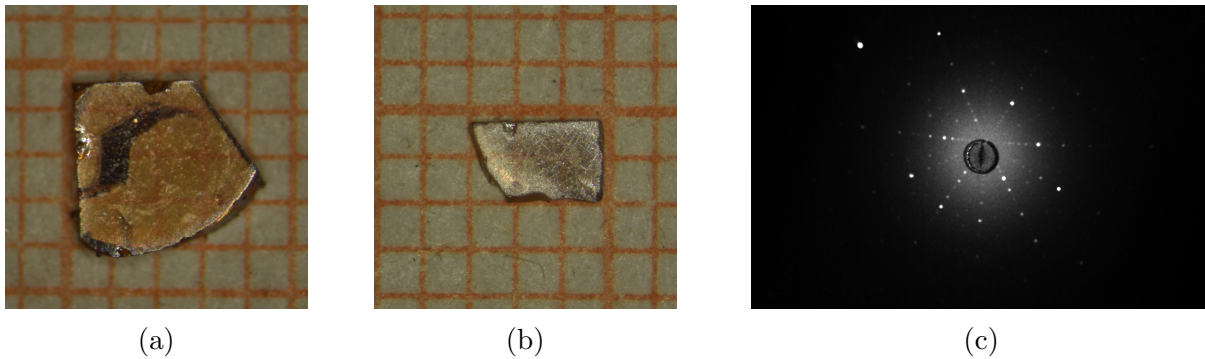


Figure 3.8.: Photographs of the $\text{Dy}_2\text{Ti}_2\text{O}_7$ samples (a) DTO5 and (b) DTO3 supplied by G. Balakrishnan. (c) Laue diffractogram of DTO3 sample oriented in $[1\ 1\ 1]$ direction.

the observations of the spin-ice materials $\text{Dy}_2\text{Ti}_2\text{O}_7$ and $\text{Ho}_2\text{Ti}_2\text{O}_7$ and I may discuss my results in view of this model.

Via dilatometric measurements I have evidenced further details on the interaction between lattice and magnetic effects in the spin-ice compounds. Magnetoelastic coupling should couple changes of the magnetic configuration in a varying magnetic field to changes of the lattice parameter. Dilatometric measurements are very sensitive, so that new phenomena of the magnetic system might be found as features of the lattice expansion.

3.3. Experimental

3.3.1. Samples

$\text{Dy}_2\text{Ti}_2\text{O}_7$ The oriented single-crystalline samples of $\text{Dy}_2\text{Ti}_2\text{O}_7$ were grown by G. Balakrishnan by the floating-zone technique at the University of Warwick [75]. The crystal was oriented with a Laue X-ray machine and it was checked to be of good quality, fig. 3.8c. The relaxation, the thermal expansion below 2 K and the magnetostriction measurements were performed on sample DTO3, see fig. 3.8b; these measurements were done in longitudinal geometry, i.e.. $\Delta L \parallel H \parallel [1\ 1\ 1]$ with the TDC dilatometer in a 18 T magnet. The relaxation was also measured in transverse geometry ($\Delta L \perp H \parallel [1\ 1\ 1]$). The thermal-expansion measurements between 2 K and room temperature were done on sample DTO5, fig. 3.8a, with the TAC dilatometer in a 15 T magnet. The dimensions and an estimate of the demagnetization factor are given in table 3.3.

$\text{Ho}_2\text{Ti}_2\text{O}_7$ The oriented single-crystalline samples of $\text{Ho}_2\text{Ti}_2\text{O}_7$ were grown by C. Wiebe and H. Zhou at the University of Tennessee. The measurements above 2 K were done on

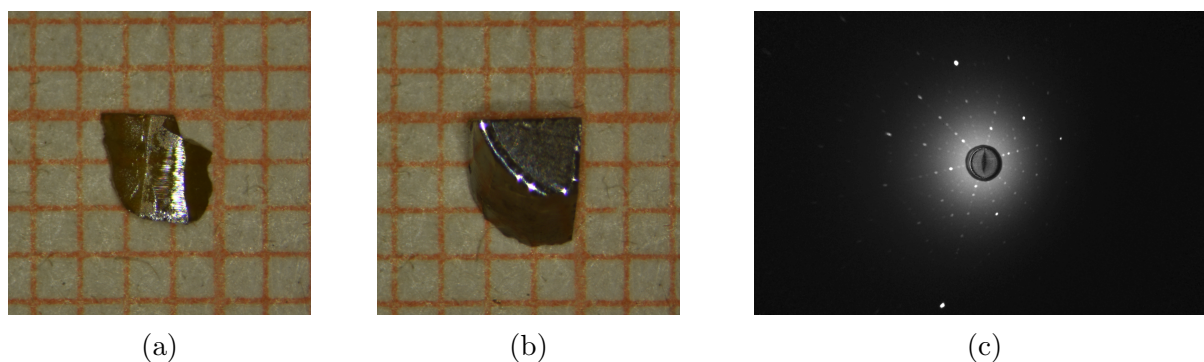


Figure 3.9.: Photographs of $\text{Ho}_2\text{Ti}_2\text{O}_7$ samples (a) HTO1 and (b) HTO2 supplied by C. Wiebe. (c) Laue diffractogram of sample HTO2 oriented in $[1\ 1\ 1]$ direction.

Table 3.3.: $\text{Dy}_2\text{Ti}_2\text{O}_7$ and $\text{Ho}_2\text{Ti}_2\text{O}_7$ samples with their dimensions and corresponding estimations of the demagnetization factors using an ellipsoid approximation [76]

Sample	Dimension in mm \times mm \times mm	Demagnetizing factor N
DTO3	$3.0 \times 1.9 \times 0.39$	0.75
DTO5	$4.0 \times 4.0 \times 1.31$	0.65
HTO1	$2.5 \times 2.2 \times 0.59$	0.70
HTO2	$2.71 \times 2.47 \times 2.36$	0.35

HTO1, shown in fig. 3.9a, with the TAC dilatometer in a 15 T magnet and the measurements below 2 K including the relaxation measurements were done on HTO2, shown in fig. 3.9b, with the TDC dilatometer in a 18 T magnet. The orientation of sample HTO2 was checked via a Laue diffractometer fig. 3.9c and the quality was found to be good. The dimensions and an estimate of the demagnetization factor are given in table 3.3.

3.3.2. Magnetostriction, thermal-expansion and lattice-relaxation measurements at $\text{Dy}_2\text{Ti}_2\text{O}_7$ and $\text{Ho}_2\text{Ti}_2\text{O}_7$

For the magnetostriction and thermal-expansion measurements two capacitance dilatometers, the TDC and the TAC, were used. Two setups at two different magnets from Oxford Instruments were used, a 15 T magnet at the Technical University Dresden and a 18 T magnet at the Dresden High-Magnetic-Field Laboratory of the Helmholtz-Zentrum Dresden-Rossendorf. The 18 T magnet is a LN_2 -shielded ^4He -bath cryostat with a commercial sorb-pumped ^3He -insert. The 15 T magnet is a ^4He -bath cryostat with a variable-temperature insert (VTI); the temperature of the sample is controlled by a He-gas flow through a needle valve from the bath. At both setups the capacity was determined using an Andeen-Hagerling capacitance bridge, model 2500A or 2700A. The temperature of

the TAC was measured with a Cernox thermometer; and the temperature of the TDC was measured with a Cernox thermometer at temperatures above 4 K and with a RuO₂ resistance thermometer below 4 K with a standard calibration curve. The resistance was measured with a Lakeshore 370 in the 18 T magnet setup and a Conductus LTC-20 at the 15 T magnet setup.

Quasi-static magnetostriction measurements The magnetostriction of Ho₂Ti₂O₇ in the temperature range from 1.5 K to 300 K I used the TAC (fig. 3.2a) in a variable-temperature insert (VTI) in a 15 T magnet. For the magnetostriction of Dy₂Ti₂O₇ in the temperature range from 0.3 to 40 K I used the TDC a sorb-pumped closed-cycle ³He system that was inserted into the 18 T magnet. The magnetostriction was measured while sweeping the field at a rate of 0.2 T min⁻¹ for temperatures above 1 K and 0.015 T min⁻¹ below. Above 1 K, there was no sweep-rate dependence or hysteresis observed. The thermal expansion between 1.5 and 300 K of both compounds was measured in the TAC in the VTI in the 15 T magnet. The temperature was swept at 1 K min⁻¹ from base temperature to room temperature and then down to base temperature.

The low-temperature magnetostriction from 0.27 K to 1.5 K and was measured using a sorb-pumped closed-cycle ³He system that was inserted into the 18 T magnet. I used the TDC (fig. 3.1) in this cryostat. The field was swept slowly at a rate of 0.015 T min⁻¹ at various temperatures in order to avoid non-equilibrium effects and for high field resolution. Between each sweep the temperature was raised above 1 K and the magnet demagnetized by oscillating the field around 0 T with decreasing amplitude. The ³He was recondensed and the new sweep started after stabilizing the dilatometer cell at the new temperature. The thermal expansion below 2 K was measured by stepping the temperature by 5% of the initial temperature starting at 0.3 K (i.e., the temperature at step n is $1.05^n \cdot 0.3$ K); at each step the temperature was stabilized for 3 min which is a compromise between the hold time of the cryostat and the required long stabilization times.

Lattice-relaxation measurements The lattice-relaxation measurements were performed in the sorb-pumped closed-cycle ³He system that was inserted into the 18 T magnet. The lattice dynamics at low temperatures were probed with several different protocols. Common to all protocols is the demagnetization sequence before each sequence of quenches; it is the same as used for the field-sweep measurements above. After the demagnetization process, the sample was cooled down to the measurement temperature and stabilized for 30 min.

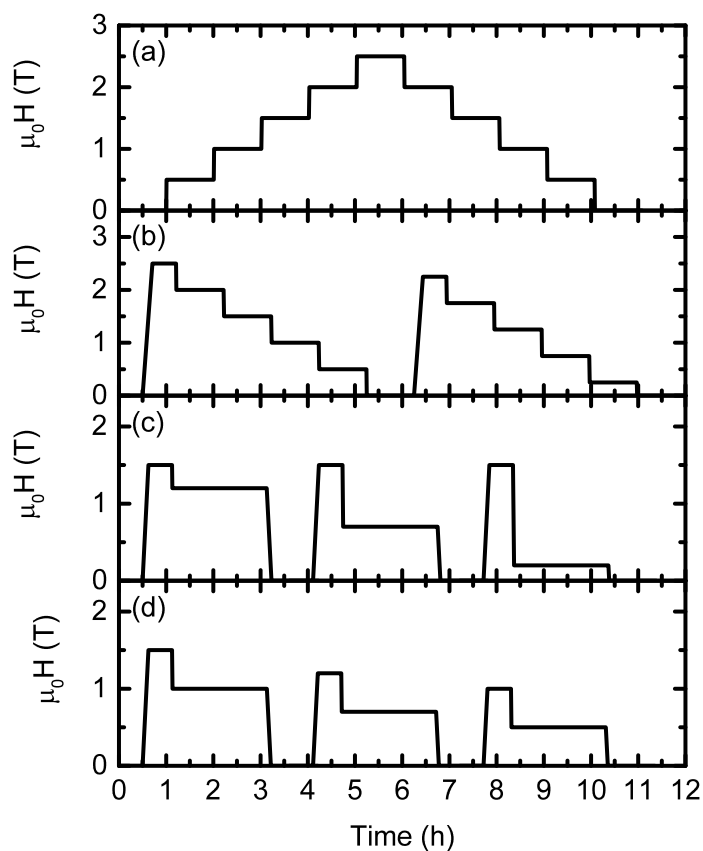


Figure 3.10.: The graphs show various quench sequences employed to probe the relaxation dynamics of $\text{Dy}_2\text{Ti}_2\text{O}_7$ and $\text{Ho}_2\text{Ti}_2\text{O}_7$. These specific examples were used for $\text{Dy}_2\text{Ti}_2\text{O}_7$ as for $\text{Ho}_2\text{Ti}_2\text{O}_7$ slightly different sequences were used. From top to bottom: (a) One sequence of type A, (b) two sequences of type B, (c) three sequences of type C and (d) three sequences of type D.

The first sequence was used to give an overview about where relaxation behavior could be observed and whether it could be found in upswing and downswing alike:

- A: The field is swept to the initial field of 0 T at a rate of 0.2 T min^{-1} and stabilized for 30 min. Then the magnetic field is stepped up at a fast sweep rate of 1 T min^{-1} in 5 steps of 0.5 T to a final field of 2.5 T stabilizing the system for 1 h after each step monitoring the relaxation in the upswing steps. After that the field is stepped down in the same steps at the same rate until it reached 0 T monitoring the relaxation in the downswing steps.

The sequence can be seen in fig. 3.10(a). After having found the region of relaxation, I probed it separately with a similar sequence that has less steps, so that the relaxation after each step could be monitored for a longer time:

B: The field is swept up to 2.5 T and the sample stabilized for 30 min. The field is stepwise reduced to zero field by 0.5 T per step with a sweep rate of 1 T min^{-1} . After each step the sample is stabilized for 1 h and the relaxation monitored.

This sequence is shown in fig. 3.10(b). With the next sequence I intended to probe the dependence of the relaxation on a longer time scale and more controlled by making only one step from the high field phase into the low-field phases:

C: At the measurement temperature the field is swept from 0 to 1.5 T at a rate of 0.2 T min^{-1} and the sample stabilized for 30 min. Then the field is swept down quickly to the final field with a rate of 1 T min^{-1} . The relaxation of the sample is monitored for 2 h and then the field is swept down to zero, ending the sequence.

This sequence is displayed in fig. 3.10(c). In the next sequence the question should be answered, whether the relaxation was also visible when the initial field was not as high as needed to set the system to the high-field phase:

D: At the measurement temperature the field is swept up to the initial field equal or below 1.5 T. Then the field is quenched down by 0.5 T and the relaxation is monitored for 2 h. The field is swept down to zero and the sequence ended.

The sequence D is shown in fig. 3.10(d). In a final sequence, I wanted to see whether the relaxation could also be seen at smaller step sizes. For this I used a sequence like sequence A with reduced step size and many steps; however, since the hold time of the cryostat is limited and the monitoring time for each relaxation should be at least 1 h the complete sequence could not be fitted in to the hold time. The sequence was, therefore, split into several parts and resumed after each recondensation and demagnetization at a field smaller than the end field of the previous part:

E: The field is swept from zero field to the initial field, where the sample is stabilized for 30 min. Then the field is increased or decreased stepwise, stabilizing the sample for 1 h and monitoring the relaxation. The sequence ends, when the hold time of the cryostat was reached.

This sequence is similar to sequence A (fig. 3.10(a)).

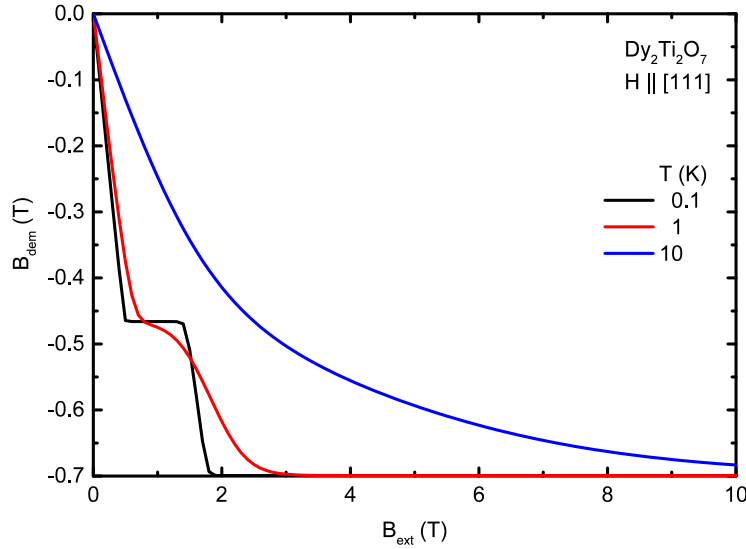


Figure 3.11.: Dependence of the demagnetization correction $B_{\text{dem}} = B_{\text{int}} - B_{\text{ext}}$ on the external field B_{ext} for various temperatures for $\text{Dy}_2\text{Ti}_2\text{O}_7$ with demagnetizing factor $N = 0.75$. I used eqs. (C.5) and (C.11) to calculate B_{dem} .

Demagnetization correction Our samples of $\text{Dy}_2\text{Ti}_2\text{O}_7$ and $\text{Ho}_2\text{Ti}_2\text{O}_7$ were plate-like with the $[111]$ perpendicular to the large faces. Since I applied the magnetic field in that direction large demagnetization effects have to be taken into account. The internal field (important for the intrinsic properties I want to probe) is different from the external field which I measure. The field values given for the thermal expansion and the relaxation measurements are internal field values. The volume-specific magnetization in $\text{Dy}_2\text{Ti}_2\text{O}_7$ and $\text{Ho}_2\text{Ti}_2\text{O}_7$ with a magnetic moment $m = x \cdot \mu_B / (\text{Dy}/\text{Ho})$ and lattice constant $a = 10.10 \text{ \AA}$ [30] is given by:

$$\mu_0 M = \mu_0 m / V = x \mu_0 \frac{16 \mu_B}{a^3} = x \cdot 0.181 \text{ T}. \quad (3.15)$$

The factor 16 is due to the 16 (Dy/Ho) atoms per unit cell. The field-dependence of the demagnetizing effect with a demagnetizing factor of $N = 0.75$ for $\text{Dy}_2\text{Ti}_2\text{O}_7$ is displayed in fig. 3.11.

Magnetic torque I refer the reader to the calculation in subsection C.1.2 which indicates that large magnetic torque could lead to a rotation of the sample. In order to exclude possible large parasitic magnetic-torque effects, I verified my results with another measurement. I glued the $\text{Dy}_2\text{Ti}_2\text{O}_7$ sample using a two-component epoxy resin to the sample holder fixed to the frame of the TDC dilatometer minimizing the possibility of the tilting or rotation

of the sample due to the magnetic torque. I reproduced the previous measurements and, therefore, exclude that my previous results were influenced by torque effects.

Part II.

Results and Discussion

4. Quasi-static magnetoelastic properties of $\text{Dy}_2\text{Ti}_2\text{O}_7$ and $\text{Ho}_2\text{Ti}_2\text{O}_7$

The ground state of the spin-ice compounds $\text{Dy}_2\text{Ti}_2\text{O}_7$ and $\text{Ho}_2\text{Ti}_2\text{O}_7$ is highly degenerate. This is a result of the fact, that, for instance, six spins around a hexagonal plaquette of the pyrochlore lattice may be reversed still preserving the spin-ice rule. Due to the cubic lattice symmetry, the ground state is isotropic. By applying a magnetic field, the symmetry is broken by favoring one specific direction lifting the degeneracy of the spin system. Depending on the strength of the spin-lattice coupling the symmetry of the lattice should also change in a way measurable by dilatometry. This means, that dilatometry is a very good means to quantify the spin-lattice coupling, i.e., the distance dependence of the exchange interactions and the strain dependence of the ground-state energy. As a result, I obtain the relative strengths of the two spin-lattice couplings.

This chapter is concerned with the static magnetoelastic properties of $\text{Dy}_2\text{Ti}_2\text{O}_7$ and $\text{Ho}_2\text{Ti}_2\text{O}_7$ probed by capacitance dilatometry in fields up to 10 T and temperatures from 0.3 to 300 K. The static magnetoelastic properties of a sample are those properties that are probed in the equilibrium. The thermal expansion of both compounds does not show any sign of a structural transition. As for the magnetostriction, both compounds show similar behavior and a transition in a field range consistent with published phase diagrams. At first, the data for $\text{Dy}_2\text{Ti}_2\text{O}_7$ and then the data for $\text{Ho}_2\text{Ti}_2\text{O}_7$ are shown in the following two sections, respectively. Both sets of data are then discussed in their own section. In order to get a better insight into the microscopics of the magnetostrictive behavior of the compounds at low temperatures I devised a simulation using the McPhase software package. The results are wrapped up in the last section of this chapter.

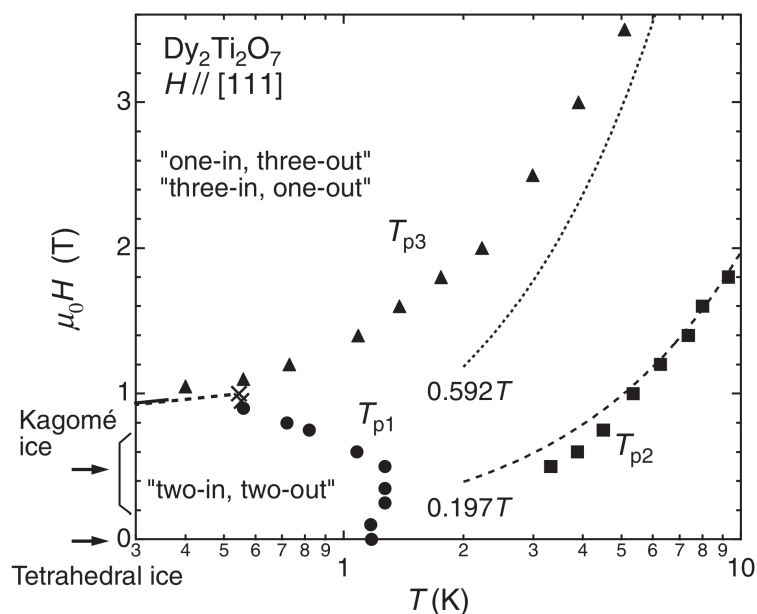


Figure 4.1.: Phase diagram of $\text{Dy}_2\text{Ti}_2\text{O}_7$ on the basis of specific-heat measurements. Reproduced from [69].

4.1. Introduction: Phase diagrams of $\text{Dy}_2\text{Ti}_2\text{O}_7$ and $\text{Ho}_2\text{Ti}_2\text{O}_7$

The phase diagram (figs. 4.1 and 4.2) of the classical spin ices $\text{Dy}_2\text{Ti}_2\text{O}_7$ and $\text{Ho}_2\text{Ti}_2\text{O}_7$ is characterized by changes of the magnetic structure. The magnetic specific heat at zero field features a Schottky-like anomaly at the temperature T_{p1} around 1.2 K for $\text{Dy}_2\text{Ti}_2\text{O}_7$ [69] and 1.9 K for $\text{Ho}_2\text{Ti}_2\text{O}_7$ [52]. Below this temperature, the spin-ice state is realized and above this temperature the spins are free to point in or out of the tetrahedron in any of the 16 configurations consistent with the local Ising axes. Depending on the magnitude of the magnetic field aligned along the $[1\ 1\ 1]$ direction there are two more phase boundaries. On the one hand, the boundary at the higher temperature (T_{p2} in fig. 4.1) signals the freezing of the spins at the top of each tetrahedron and on the other hand, the boundary at the lower temperature (T_{p3}) is linked to the freezing of the three spins at the basis of the tetrahedron. The former is at higher temperatures due to stronger Zeeman splitting of the spin at the top than for those at the basis for all fields. The low-temperature regime below T_{p1} may be further characterized by the magnetic properties of the compounds (fig. 4.2): spin-ice phase at zero field, the kagome-ice phase at intermediate fields below the transition field H_c , and the saturated-ice phase (3-in/1-out) at fields higher than H_c . The critical field H_c is 0.9 T for $\text{Dy}_2\text{Ti}_2\text{O}_7$ [77] and 1.5 T for $\text{Ho}_2\text{Ti}_2\text{O}_7$ [68, 78]. At temperatures below approximately $T_c = 0.5$ K the magnetic transition at H_c is first order and seen as a jump

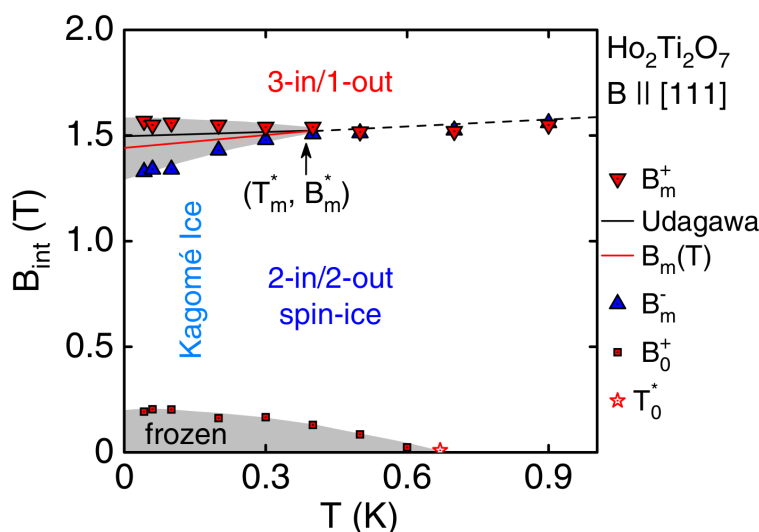


Figure 4.2.: Phase diagram of $\text{Ho}_2\text{Ti}_2\text{O}_7$ on the basis of magnetization measurements. Reproduced from [68].

in the magnetization. Above T_c , the magnetic transition is smoothed out to a crossover. Below H_c , there is a magnetization plateau, called the kagome-ice phase, that is well defined at low temperatures below T_c in the spin-ice phase. The transition from the spin-ice to the kagome-ice phase is also seen as a jump at very low fields from zero magnetization to the magnetization of the plateau. In the following, new magnetostriction and thermal-expansion data are presented and discussed on the basis of these phase diagrams.

4.2. Results for $\text{Dy}_2\text{Ti}_2\text{O}_7$

In this section, I present the thermal-expansion and magnetostriction results of $\text{Dy}_2\text{Ti}_2\text{O}_7$ I obtained in a wide temperature range from 0.3 K to 300 K and in fields up to 3 T. The thermal-expansion data are shown in figs. 4.3 and 4.4. The magnetostriction data are shown in fig. 4.5.

Thermal expansion At first, I measured the zero-field thermal-expansion shown in fig. 4.3, i.e., the relative expansion of the sample in dependence of the temperature. The crystal expands monotonously from 2 to 273 K by $\Delta L/L = 2.3 \times 10^{-3}$. The thermal-expansion coefficient is not constant and increases over the complete measurement range. The slope is steepest at low temperatures and becomes smaller towards room temperature possibly becoming zero over room temperature. There is no sign of a phase transition of the lattice in this temperature range. The crystal symmetry is likely to remain the same pyrochlore structure over the entire temperature range measured.

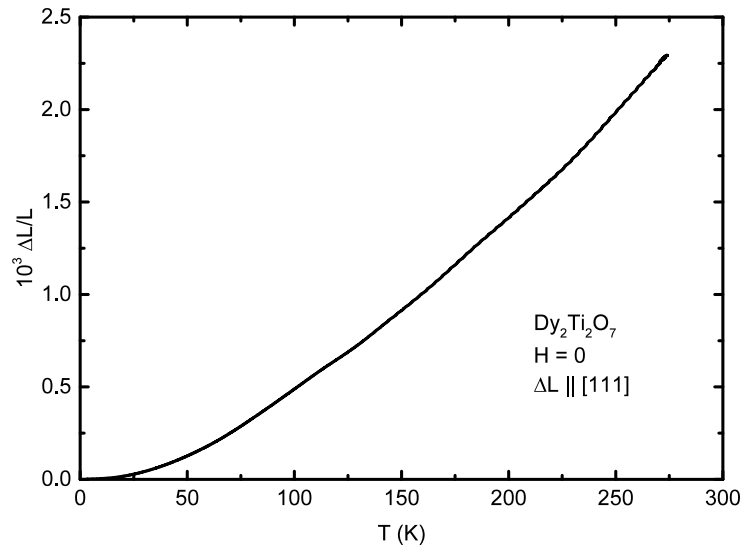


Figure 4.3.: Temperature dependence of the relative length change of $\text{Dy}_2\text{Ti}_2\text{O}_7$ (sample DTO5) in the VTI using the TAC.

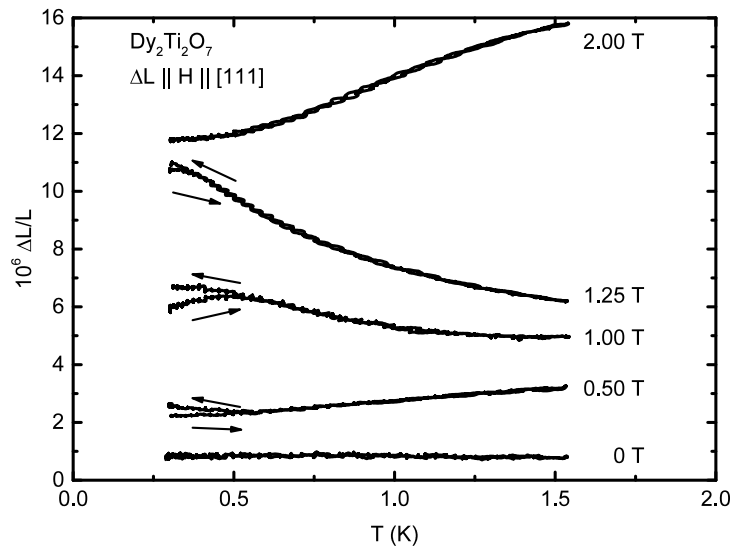


Figure 4.4.: Temperature dependence of the relative length change of $\text{Dy}_2\text{Ti}_2\text{O}_7$ (sample DTO2) between 0.3 and 1.5 K at various fields in longitudinal geometry. The given fields are not corrected for demagnetization.

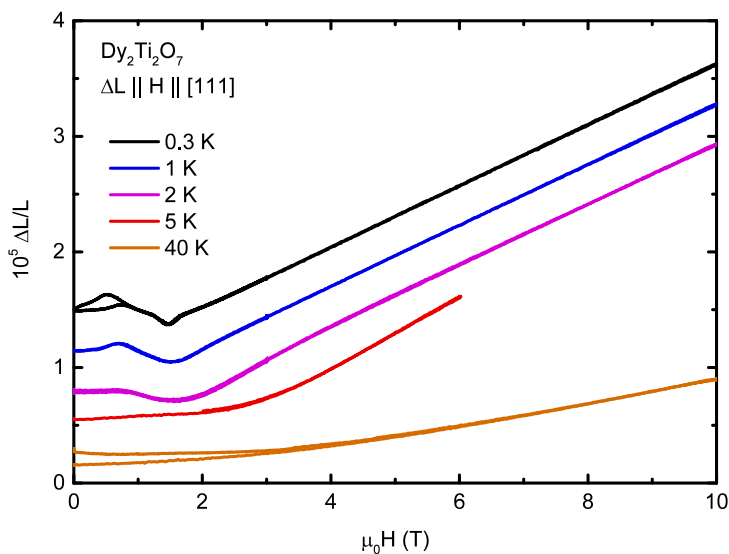


Figure 4.5.: Field dependence of the relative length change $\Delta L/L$ of $Dy_2Ti_2O_7$ (sample DTO2). The sample was glued to the sample holder of the TDC to exclude sample rotation by magnetic torque.

The zero-field thermal expansion at temperatures below 1.5 K is equally unremarkable as can be seen from the flat black curve in fig. 4.4, while the temperature dependence of $\Delta L/L$ in applied fields shows various features. The plot shows the relative expansion of the sample in dependence of the temperature in up- and downsweeps for various fields not corrected for demagnetization. The temperature was changed stepwise by 5% per step and stabilized for 3 min. The relative thermal expansion of $Dy_2Ti_2O_7$ in this temperature range is of the order of $\Delta L/L = 10^{-7}$ to 10^{-6} . For fields below 1 T the thermal relative length change between 0.3 and 1.5 K is smaller than $\Delta L/L = 2 \times 10^{-6}$, while above this field it more than doubles to $\Delta L/L = 4 \times 10^{-6}$. In general, the field dependence is complex: for low fields, below 0.5 T, and for the highest field of 2 T the lattice is monotonously expanding with temperature. For the intermediate fields of 1 T and 1.25 T the length change is negative over some range. The up-sweep (zero-field-cooled (ZFC)) and the down-sweep curve (field-cooled (FC)) differ at temperatures below 0.5 K for 0.5, 1 and 1.25 T.

Magnetostriction The graphs displayed in fig. 4.5 show the relative length change of the sample in dependence of the external magnetic field at various temperatures between 0.3 and 40 K. In this temperature range, the magnetostrictive effects are of the order of $\Delta L/L = 10^{-5}$. For high temperatures above 5 K, the lattice does not strongly react to small fields below 3 T and expands linearly above. The low-temperature magnetostriction at 0.3, 1 K and 2 K resemble each other. The lattice expands in fields up to about 1 T and then

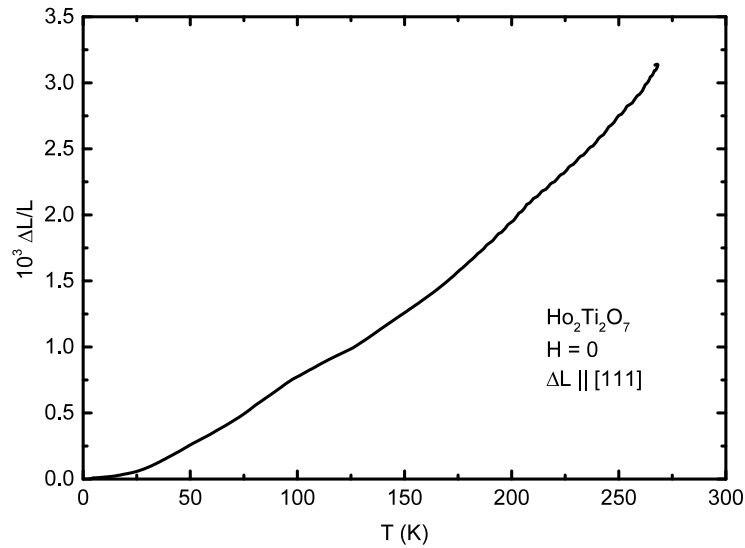


Figure 4.6.: Temperature dependence of the thermal expansion of $Ho_2Ti_2O_7$ (sample HTO1) measured by use of the VTI.

contracts reaching a minimum at 1.5 T. This maximum-minimum feature is characteristic for the spin-ices and will be considered especially in my simulation. At fields above 2 T the lattice expands linearly with an expansion coefficient of approximately $2.5 \times 10^{-6} T^{-1}$. At the lowest temperature (0.3 K) a hysteresis is opening below the maximum.

The results of this section are going to be discussed in section 4.5. In the next section, the results of the thermal-expansion and the magnetostriction measurements on $Ho_2Ti_2O_7$ are presented.

4.3. Results for $Ho_2Ti_2O_7$

In this section, the thermal-expansion and magnetostriction results of $Ho_2Ti_2O_7$ are presented. I obtained them in the same temperature and a similar field range as for $Dy_2Ti_2O_7$ in the previous section. This section organised into paragraphs presenting the thermal-expansion measurements with figs. 4.6 and 4.7, as well as the magnetostriction measurements with figs. 4.8 and 4.9.

Thermal Expansion The zero-field thermal expansion of $Ho_2Ti_2O_7$, shown in fig. 4.6, is very similar to the one of $Dy_2Ti_2O_7$ in fig. 4.3. The relative expansion between 2 K to 268 K is monotonous and positive with $\Delta L/L = 3 \times 10^{-3}$. The thermal-expansion coefficient α is larger by about 30 % for $Ho_2Ti_2O_7$ than for $Dy_2Ti_2O_7$. The general behavior of the the thermal-expansion coefficient is the same as for $Dy_2Ti_2O_7$: the rate-of-change largest at

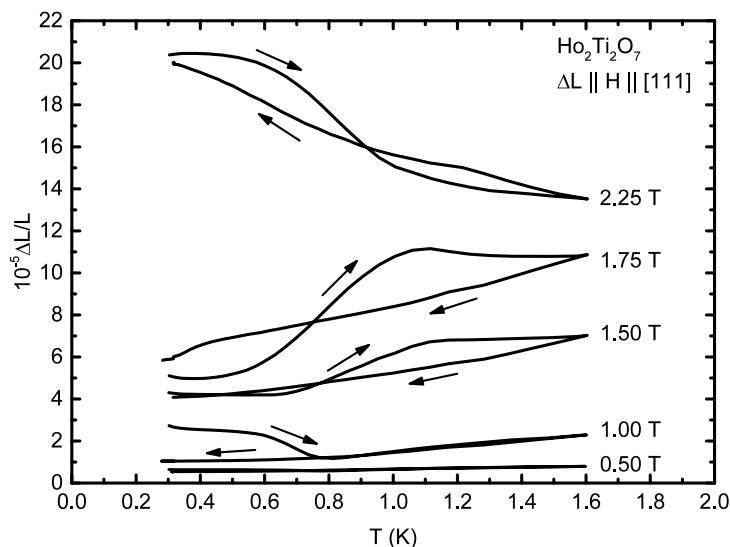


Figure 4.7.: The thermal expansion of $\text{Ho}_2\text{Ti}_2\text{O}_7$ measured by use of the 3 He cryostat at various fields. The field values are not corrected for demagnetization.

low temperatures and becomes smaller towards room temperature and may vanish over room temperature. I conclude from this high temperature thermal expansion measurement that $\text{Ho}_2\text{Ti}_2\text{O}_7$ does not undergo a structural phase transition in this temperature range.

The low-temperature thermal expansion, displayed in fig. 4.7, was measured in the same way as it was done for $\text{Dy}_2\text{Ti}_2\text{O}_7$ (fig. 4.4). In comparison with $\text{Dy}_2\text{Ti}_2\text{O}_7$ the thermal-expansion effects are stronger by about one order of magnitude: $\Delta L/L = 10^{-6}$ to 10^{-5} depending on the magnetic field. For fields up to 1.75 T, the thermal expansion is positive and is negative for 2.25 T. The up-sweep curve is flat for all fields and becomes steep at temperatures around 0.75 K; the down-sweep curve is rather linear. It was observed, that the time dependence of the relative expansion in the three minutes after each step shows an exponential behavior at high temperatures crossing over to a continuous curve without steps for temperatures below 0.9 K. Probably, slow dynamics keep the system at these low temperatures from reaching the equilibrium during the stabilization time of three minutes. This means that the relaxation time is around 3 min = 180 s at 0.9 K and increases strongly for temperatures below 0.9 K. In comparison to this, the $\text{Dy}_2\text{Ti}_2\text{O}_7$ sample did not show such strong thermal hysteresis.

Magnetostriction We shift our focus to the high-temperature magnetostriction data of $\text{Ho}_2\text{Ti}_2\text{O}_7$ displayed in fig. 4.8. The relative expansion of $\text{Ho}_2\text{Ti}_2\text{O}_7$ is shown in dependence of the external magnetic field at various temperatures (2.4, 5.9 and 22.8 K). The magnetostriction of $\text{Ho}_2\text{Ti}_2\text{O}_7$ is of the order of 1×10^{-5} at temperatures above 2 K, fig. 4.8. The

relative length change is larger for $\text{Ho}_2\text{Ti}_2\text{O}_7$ than for $\text{Dy}_2\text{Ti}_2\text{O}_7$ (fig. 4.5). The curve is flat around zero field and shows contraction with increasing field up to a temperature-dependent field H_{\min} , where the $\Delta L/L$ has a minimum. For fields higher than H_{\min} the crystal expands again. H_{\min} in $\text{Ho}_2\text{Ti}_2\text{O}_7$ is larger than the equivalent field in $\text{Dy}_2\text{Ti}_2\text{O}_7$, reflecting the stronger interactions among nearest-neighbor moments. Upsweep and down-sweep curves are identical and no hysteresis was observed.

Last, but not least, the longitudinal magnetostriction of $\text{Ho}_2\text{Ti}_2\text{O}_7$ at temperatures between 0.3 and 1.5 K is shown in fig. 4.9. The field was swept with a rate of 0.015 T min^{-1} . The relative length change is of the order of about $\Delta L/L = 10^{-4}$. This is a factor 20 larger than the magnetostriction of $\text{Dy}_2\text{Ti}_2\text{O}_7$; however, it is consistent with the high-temperature measurements above. The general behavior of the relative expansion is as follows: Sweeping up the field, the crystal expands up to a temperature-independent field of about 0.4 T. Then there is a contraction up to a field H_{\min} , followed by a strong expansion with a shoulder-like anomaly. The expansion does not cease with increasing field. In the downsweep measurement, I find generally the similar curve shape with certain differences. The shoulder-like anomaly does not precede the minimum at H_{\min} but follows it at a lower field. The field $H_{\min,\text{down}}$ in downsweep is lower than the field $H_{\min,\text{up}}$ at upsweep, leading to a hysteresis around H_{\min} . At low temperatures, there is another hysteresis opening below the shoulder-like anomaly at downsweep. The shoulder-like anomalies become smaller in magnitude with increasing field. Furthermore, the anomaly during downsweep is shifted to higher fields with increasing temperature, being possibly related to the slow relaxation dynamics at low temperatures. The second hysteresis that is only seen at low temperatures probably has its origin in the same slow dynamics. The hysteresis, displaying different $H_{\min,\text{up}}$ and $H_{\min,\text{down}}$ and different positions of the shoulder-like anomaly are separated by approximately 0.6 T, not entirely explainable by demagnetizing effects.

After pointing out the details of the measurements, I will discuss the results in the next section.

4.4. Simulation of the magnetostriction

In order to link my measurements to theory, I performed a mean-field calculation using the software bundle McPhase [79]. The steps of the calculation are stated here briefly to remind the reader of the detailed explanation in subsection 2.2.3. At first, I used McPhase to calculate the crystal-field parameters via a point-charge model, in order to construct the single ion Hamiltonian. Then, I diagonalized this Hamiltonian (eq. (2.1)) with McPhase and obtained the energy scheme of the rare-earth single ion in the crystal-

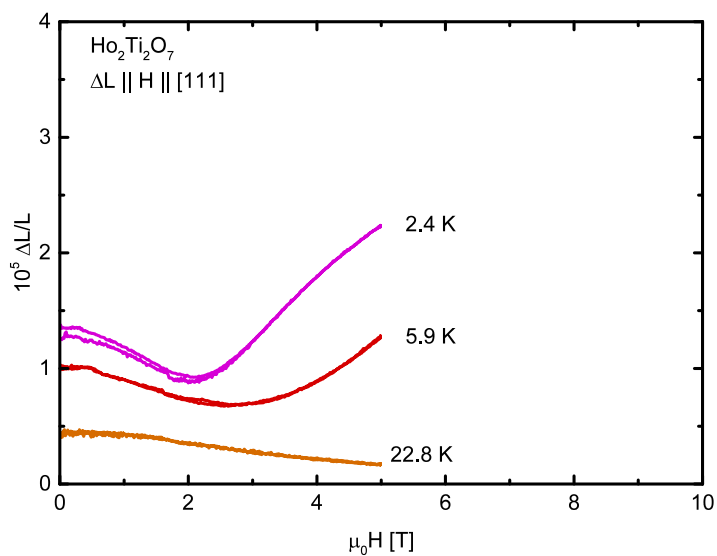


Figure 4.8.: Field dependence of the magnetostriction of $\text{Ho}_2\text{Ti}_2\text{O}_7$ (sample HTO2 glued to the sample holder in the TAC).

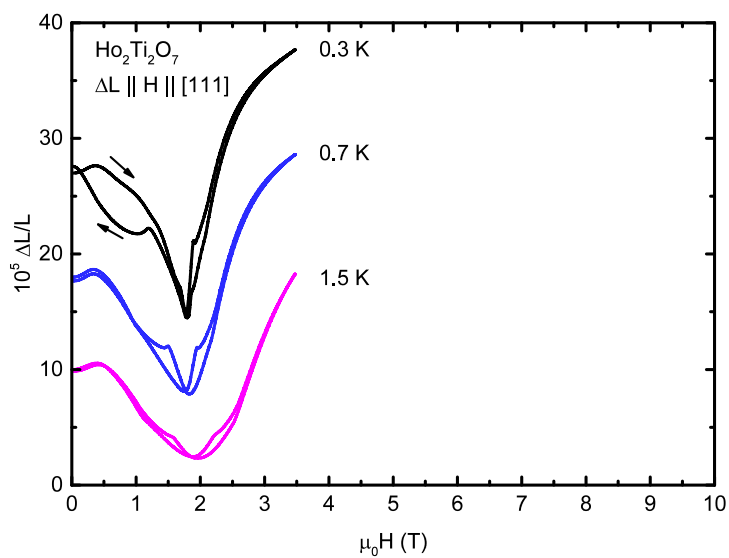


Figure 4.9.: The magnetostriction of $\text{Ho}_2\text{Ti}_2\text{O}_7$ (sample HTO2) measured by use of the ^3He cryostat at various temperatures at a slow sweep rate of 0.015 T min^{-1} .

Table 4.1.: The crystal-field parameters of $\text{Dy}_2\text{Ti}_2\text{O}_7$ from the point-charge model of the unstrained and the strained lattice, and from literature [40]. Values are given in meV.

Set	B_0^2	$10^3 B_0^4$	$10^3 B_3^4$	$10^5 B_0^6$	$10^5 B_3^6$	$10^5 B_3^6$
unstrained	-0.994	0.243	-8.26	0.0414	1.32	0.379
strained	-1.007	0.249	-8.13	0.0358	1.37	0.364
[40]	-0.20	-2.2	-19	0.66	-10.9	9.0

Table 4.2.: The crystal-field parameters of $\text{Ho}_2\text{Ti}_2\text{O}_7$ from the point charge model of the unstrained and the strained lattice, and from literature [40]. Values are given in meV.

Set	B_0^2	$10^3 B_0^4$	$10^3 B_3^4$	$10^5 B_0^6$	$10^5 B_3^6$	$10^5 B_3^6$
unstrained	-0.335	0.126	-4.26	-0.0445	-1.50	0.418
strained	-0.340	0.129	-4.20	-0.0383	-1.55	0.402
[40]	-0.068	-1.13	-10.1	-0.74	12.3	10.1

electric field in $\text{Dy}_2\text{Ti}_2\text{O}_7$ and $\text{Ho}_2\text{Ti}_2\text{O}_7$. Finally, I calculated the magnetization and the equilibrium strain (eq. (2.13)) with the estimated and approximated values explained in subsection 2.2.3. The two free parameters of the model are the nearest-neighbor exchange constant J and its distance dependence $\partial_r J$. I tried to answer two questions:

- What is the origin of the peak at the transition at 1.3 T?
- What is the origin of the high-field expansion?

I need the crystal-field parameters of the unstrained and the strained system; therefore I cannot use the parameters from literature [40, 42] which give only the parameters for the former. The point-charge model used for the calculation needs the crystal structure and a charge-screening factor as input. The crystal structure is given in the literature [32]. The screening factor is chosen such that the energy gap between the ground state and the first excited level of 21 meV for $\text{Dy}_2\text{Ti}_2\text{O}_7$ and 21.9 meV for $\text{Ho}_2\text{Ti}_2\text{O}_7$ as given in the literature [42]. I simultaneously fit the crystal field of $\text{Ho}_2\text{Ti}_2\text{O}_7$ and $\text{Dy}_2\text{Ti}_2\text{O}_7$ with the same screening factor of 0.117 for all charges. The gap to the first excited crystal field level corresponding to the crystal field parameters in table 4.1 for $\text{Dy}_2\text{Ti}_2\text{O}_7$ and table 4.2 are $E = 35$ meV for $\text{Dy}_2\text{Ti}_2\text{O}_7$ and $E = 13$ meV for $\text{Ho}_2\text{Ti}_2\text{O}_7$. Although the crystal field parameters are not the same as in the literature (tables 4.1 and 4.2) the wave functions of the ground states agree reasonably with the literature [40, 42]. The wave functions are given in the section A.9.

Simulation of Dy₂Ti₂O₇ I can reproduce the magnetization plateau of Dy₂Ti₂O₇ with my simulation. Figure 4.10 shows the magnetization calculated for the complete Hamiltonian (eq. (2.5)) with an exchange constant J chosen such that the transition would be around 0.9 T, i.e., $J = 0.005$ meV. Indeed, the magnetization plateau could be reproduced for the temperature of 0.3 K. At 0.3 K, the magnetization increases with a slope of approximately $1 \times 10^{-2} \mu_B/\text{T}$ after reaching the plateau at approximately $5 \mu_B/\text{Dy}$. The inset shows the magnetization curve for a temperature of 0.3 K up to complete polarization of the moments at $10 \mu_B$ for high fields of around 1000 T. At high temperatures of 10 K and 20 K no plateau is seen and the magnetization increases slowly to $5 \mu_B/\text{Dy}$. The high-temperature magnetization then continues to increase further in the same fashion as the magnetization at 0.3 K. High-field measurements on Ho₂Ti₂O₇ [66] although measured in a different direction show a similar increase of the magnetization. In my model, the increase of the averaged magnetic moment per ion comes from a mixing of crystal-field levels with higher magnetic moment in [1 1 1] into the ground level. The ions that are affected by this are located at the base of each tetrahedron.

In order to calculate the magnetostrictive effects I need the following parameters: The elastic constants are taken from ultrasound measurements [19]; in particular, they report $c_{11} = 355$ GPa, $c_L = 335$ GPa and $c_T = 92$ GPa (which are defined there). The relevant elastic parameters I need are c_{11} and c_{12} which can be derived from the above constants using eq. (2.15), I obtain $c_{11} - c_{12} = 194$ GPa needed for eq. (2.17). I use a unit cell with four tetrahedra per unit cell, i.e., $V = V_c/4$ with $V_c = a^3$; $a = 10.105$ Å denoting the lattice parameter. The prefactor of eq. (2.17), therefore, evaluates to $16/(3V_c(c_{11} - c_{12})) = 4.268 \times 10^{-6} \text{ meV}^{-1}$. The total magnetostriction can be separated into two effects: the crystal-field striction (CFS) calculated via:

$$\epsilon'_{\text{CFS}} = -\frac{16}{3V_c(c_{11} - c_{12})} \left(\sum_{s=1}^4 \sum_{l=0}^6 \sum_{m=-l}^l \left[\frac{B_l^m(\epsilon) - B_l^m(0)}{\epsilon} \right]_{\epsilon=0.01} \langle O_l^m \rangle \right). \quad (4.1)$$

and the exchange striction (ES) calculated via:

$$\epsilon'_{\text{ES}} = \frac{16}{3V_c(c_{11} - c_{12})} \frac{l}{8} \frac{\partial J}{\partial r} \left(\left[\langle \vec{J}_1 \vec{J}_2 \rangle + \langle \vec{J}_1 \vec{J}_3 \rangle + \langle \vec{J}_1 \vec{J}_4 \rangle + \langle \vec{J}_2 \vec{J}_1 \rangle + \langle \vec{J}_3 \vec{J}_1 \rangle + \langle \vec{J}_4 \vec{J}_1 \rangle \right] \right. \\ \left. - \left[\langle \vec{J}_2 \vec{J}_3 \rangle + \langle \vec{J}_2 \vec{J}_4 \rangle + \langle \vec{J}_3 \vec{J}_4 \rangle + \langle \vec{J}_3 \vec{J}_2 \rangle + \langle \vec{J}_4 \vec{J}_2 \rangle + \langle \vec{J}_4 \vec{J}_3 \rangle \right] \right). \quad (4.2)$$

with the symbols used in chapter 2.

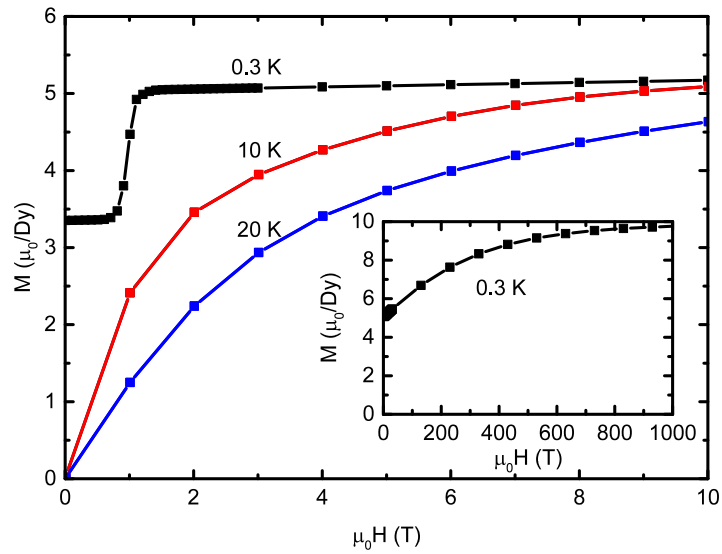


Figure 4.10.: McPhase simulation of the magnetization for $\text{Dy}_2\text{Ti}_2\text{O}_7$ at various temperatures. Inset: Magnetization curve at 0.3 K up to saturation at high fields.

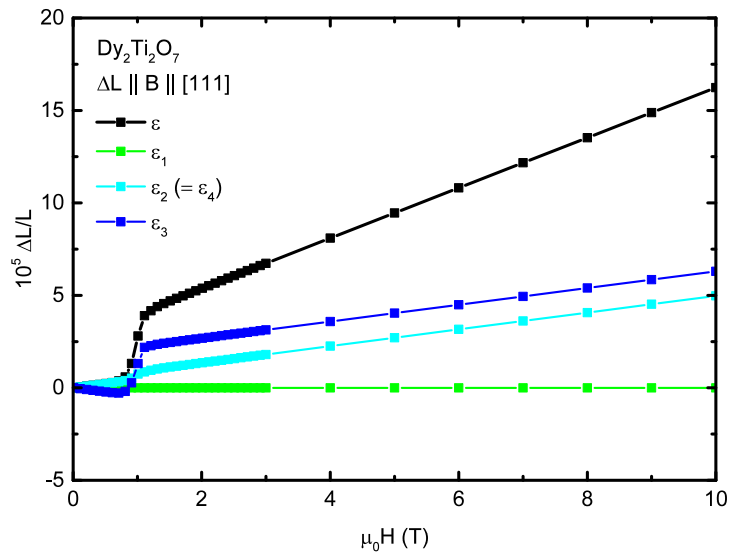


Figure 4.11.: McPhase simulation of the field dependence of the crystal-field striction (CFS) of $\text{Dy}_2\text{Ti}_2\text{O}_7$ at 0.3 K. The equilibrium strain ϵ due to CFS is shown in black. The contributions of each ion of a tetrahedron to the equilibrium strain ϵ_1 , ϵ_2 , ϵ_3 and ϵ_4 are shown in colors.

Let us now focus on the CFS of $\text{Dy}_2\text{Ti}_2\text{O}_7$, shown in fig. 4.11. In the graph, the contribution of each ion of a tetrahedron to the equilibrium strain and the total equilibrium strain are shown. ϵ_s denotes the contribution of the ion at vertex s of the tetrahedron: vertices 2, 3 and 4 are at the basis of the tetrahedron while vertex 1 is at the top, the apical vertex. In eq. (4.1), ϵ_s are given by the expression in the parentheses. The apical ion hardly contributes to the CFS, i.e., ϵ_1 is field independent, so we focus on the contribution of the ions at the basis. In general, there is an obvious transition at $H_c = 1$ T where the magnetic moment of ion 3 is flipped. Below the transition, the ion 3 gives a negative contribution to the equilibrium strain, while the other two give positive contributions. Still, at the transition, even the two ions that are not flipped show a jump of ϵ_i . Above the transition, all three ions at the basis give an equivalent contribution to the equilibrium strain. The resulting expansion coefficient of the total equilibrium strain ϵ above the transition is $\alpha_B = 1.36 \times 10^{-5} \text{ T}^{-1}$. In comparison, the experimental expansion coefficient of $\text{Dy}_2\text{Ti}_2\text{O}_7$ is approximately $2.5 \times 10^{-6} \text{ T}^{-1}$, i.e., a factor of 0.18 smaller than the simulation.

The other striction mechanism, the exchange striction (ES) in $\text{Dy}_2\text{Ti}_2\text{O}_7$ is discussed in the following paragraph. The ES contribution results from the mutual interaction of the magnetic moments \vec{J} on neighboring lattice sites and the dependence of the interaction strength on the distance. Equation (4.2) was used to calculate this contribution with the free parameter $l\partial_r J = 0.2 \text{ meV}$ to match orders of magnitude of the ES and the CFS. This parameter is linked to the change of the exchange constant J with distance. Remember, that the exchange constant $J = 0.005 \text{ meV}$ was chosen to match the transition from the kagome-ice to saturated-ice state. Figure 4.12 shows the ES at 0.3 K up to 20.3 K in the main graph in the low-field regime and in the inset up to 1000 T. At 0.3 K, the ES shows a jump at the transition field H_c from one plateau to another plateau. The jump is the result of the flip of the magnetic moment of ion 3 in the basis of each tetrahedron at the transition from the kagome-ice to the saturated-ice state. The higher temperature curves at 10.3 K and 20.3 K smoothly transit from their zero-field value to the intermediate field plateau observed at 0.3 K. At high fields of the order of 100 T, the three curves merge and increase smoothly, reaching saturation at fields of the order of 1000 T.

In the last step, the CFS and ES data are combined to obtain the total magnetostriction of $\text{Dy}_2\text{Ti}_2\text{O}_7$, shown in fig. 4.13. The competition of CFS and ES in the relative strength shown here leads to a peak-valley anomaly at the transition field. The magnetostriction for fields above the transition is dominated by the CFS and increases linearly with a slope $\alpha_B = 1.36 \times 10^{-5} \text{ T}^{-1}$. In comparison with the experimental data from fig. 4.5 (also shown in fig. 4.13) the simulation captures several features I also observed in experiment. Firstly, the high-field magnetostriction is linearly increasing in experiment as well as in the simulation;

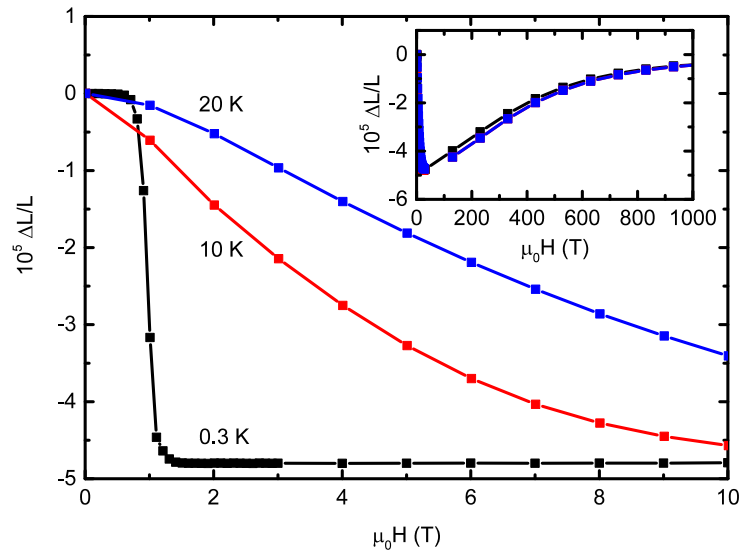


Figure 4.12.: McPhase simulation of the field-dependent ES for $Dy_2Ti_2O_7$ at various temperatures. Inset: ES at high fields up to 1000 T.

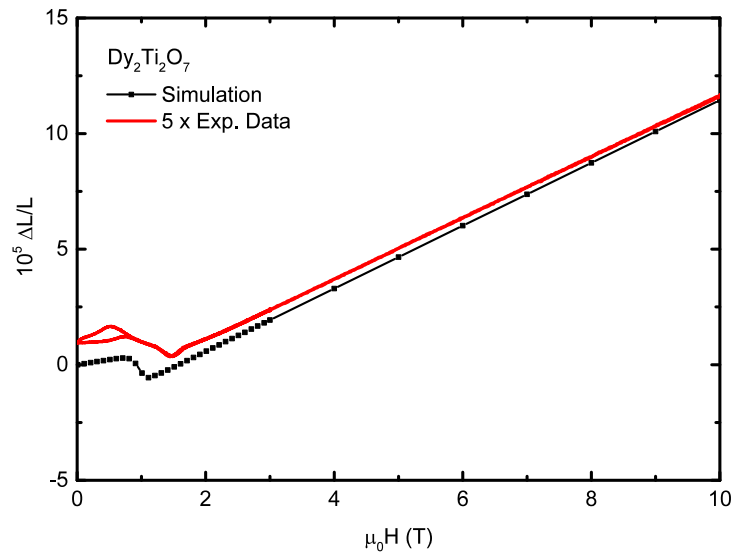


Figure 4.13.: McPhase simulation of the field-dependent total magnetostriction $\Delta L/L$ of $Dy_2Ti_2O_7$ at 0.3 K. $\Delta L/L$ is the sum of the CFS and ES shown in figs. 4.11 and 4.12. For comparison the magnetostriction data from the experiments shown in fig. 4.5 multiplied by 5 is shown, as well.

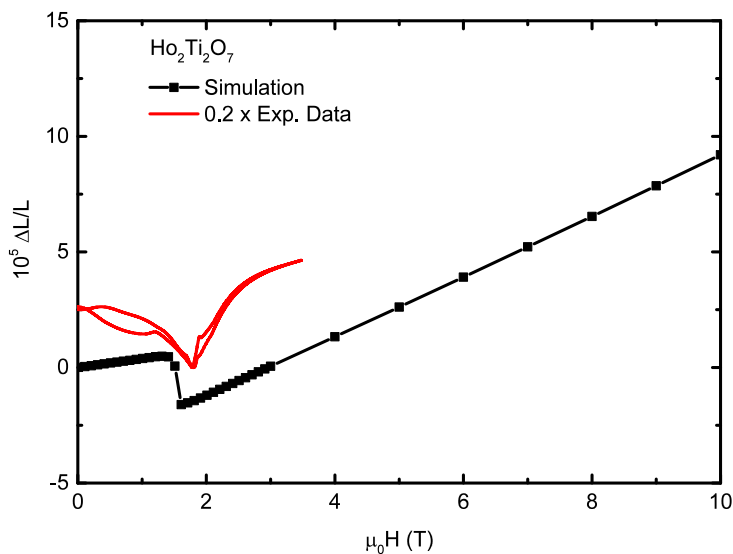


Figure 4.14.: McPhase simulation of the crystal-field and the exchange contribution to the total magnetostriction of $\text{Ho}_2\text{Ti}_2\text{O}_7$ at low temperature 0.3 K.

secondly, I find a contraction of the lattice after a maximum at the transition, the valley-peak anomaly in both, the experiment and the simulation. However, the experimental data is not corrected for demagnetization and, therefore, the transition is seen at a higher field than in the simulation. The absolute values of the modeled magnetostriction differ by a factor 5 compared to the experimental data. That means, that the difference between maximum and minimum in the peak-valley anomaly and the slope of the magnetostriction at high-fields are 5 times too large in simulation. The former could be solved by using $l\partial_r J = 0.04 \text{ meV}$ to match the peak-valley anomaly quantitatively; the latter would need a smaller magnetoelastic coupling $\partial_r B_l^m$ around one fifth of the current values. Possibly, a more elaborate modelling of the crystal field would help to close this quantitative gap between simulation and experiment at high-fields.

Simulation of $\text{Ho}_2\text{Ti}_2\text{O}_7$ For the calculation of $\text{Ho}_2\text{Ti}_2\text{O}_7$ I took the same steps explained for $\text{Dy}_2\text{Ti}_2\text{O}_7$. Since the results are quite similar, only the necessary calculation parameters are given and the total magnetostriction, i.e., the sum of the ES and CFS are shown. For $\text{Ho}_2\text{Ti}_2\text{O}_7$, the following values are used for this simple model calculation: The exchange constant $J = 0.007 \text{ meV}$ was chosen such that the magnetization shows a transition at 1.5 T; the value of $l\partial_r J = 0.28 \text{ meV \AA}^{-1}$. I take the elastic constants $c_{11} = 354 \text{ GPa}$, $c_L = 312 \text{ GPa}$ and $c_T = 113 \text{ GPa}$ from Erfanifam *et al.* [19] that result in $c_{11} - c_{12} = 197 \text{ GPa}$ using eq. (2.15). In general, the behavior of the calculated magnetostriction of $\text{Ho}_2\text{Ti}_2\text{O}_7$ is the same as the one of $\text{Dy}_2\text{Ti}_2\text{O}_7$. However, the agreement of the experimental and the

simulated magnetostriction is only qualitative, but similar to $\text{Dy}_2\text{Ti}_2\text{O}_7$. At the relevant field of around 1.7 T the experimental data and the simulation data of the magnetostriction show a minimum and an increasing lattice expansion at higher fields. The absolute values of the magnetostriction in the model and in the experiment do not match well and are a factor of five apart. Similar but opposite modifications as for the simulation of $\text{Dy}_2\text{Ti}_2\text{O}_7$ would be needed to reconcile the magnitude of the effects in simulation and experiment.

4.5. Discussion

Based on my measurements described in the previous sections I discuss several points to place this work in the current research. In particular, a) I compare my data to previous measurements of various physical properties to complement existing phase diagrams with the data of this work, and I discuss b) the hysteresis, c) the dynamical effects of the spin ices observed with other measurement techniques and d) the difference of the field-cooled and zero-field-cooled thermal expansion.

Comparison of $\text{Dy}_2\text{Ti}_2\text{O}_7$ and $\text{Ho}_2\text{Ti}_2\text{O}_7$ The high-temperature thermal expansion (figs. 4.3 and 4.6) is very similar for both compounds having approximately the same amplitude. Thermal-expansion coefficients of 10^{-5} K^{-1} at room temperature have been found for all rare-earth titanate pyrochlores [32]. This is consistent with the thermal-expansion coefficients found for the samples in this work. No sign of a structural transition could be found and it can be assumed that the lattice structure at low temperatures is the same as the one at room temperature. Likewise, the high-temperature magnetostriction data (figs. 4.5 and 4.8) for both samples show similar field-dependences; however, the magnetostriction is larger for $\text{Ho}_2\text{Ti}_2\text{O}_7$ than for $\text{Dy}_2\text{Ti}_2\text{O}_7$. The low-temperature magnetostriction is also similar in behavior (figs. 4.5 and 4.9) for both compounds showing a peak-valley anomaly in the field region where a change from the kagome-ice to the saturated-ice phase is expected. The magnetostrictive effect is larger for $\text{Ho}_2\text{Ti}_2\text{O}_7$ than for $\text{Dy}_2\text{Ti}_2\text{O}_7$, about one order of magnitude. The low-temperature thermal expansion in zero field is much smaller than $1 \times 10^{-6} \text{ K}^{-1}$ and almost constant in both cases, figs. 4.4 and 4.7. In field, however, both compounds show significant temperature dependences reflecting the strong field dependence of the relative length change of the lattice observed in magnetostriction measurements. The effects are about one order of magnitude larger for $\text{Ho}_2\text{Ti}_2\text{O}_7$ than for $\text{Dy}_2\text{Ti}_2\text{O}_7$ consistent with the magnetostriction measurements. The major difference between these two compounds is that Dy^{3+} is a Kramers ion, while Ho^{3+} is a non-Kramers ion. This may be the reason for the strong differences at low tempera-

tures. In summary, both compounds show very similar behavior in magnetostriction, as well as thermal expansion.

Comparison of the simulation with the experiment The simulation using McPhase has shown that the magnetostriction data of $\text{Dy}_2\text{Ti}_2\text{O}_7$ may be very well modeled taking into account crystal-field as well as exchange striction. Neither crystal-field nor exchange striction alone, model the magnetostriction measurements and only the competition of both mechanisms can describe the data. This is evidence that even though the crystal-field ground doublet is separated from the first excited level by a large gap of 200 K, the crystal field effects may not be neglected. However, the magnetostriction data of $\text{Dy}_2\text{Ti}_2\text{O}_7$ and the simulation differ by a factor of 5. A possible reason for the difference could be the simple modeling of the crystal-field effects with a point-charge model and a more elaborate model might help to close the gap.

Comparison with known phase diagrams Comparing my measurements to these observations from literature I can make several points. First of all, in zero field there is no sign of any transition at any temperature in the range from 0.3 K to 270 K. The mere change from a disordered spin structure to the spin ice structure, which would be expected at around 1.2 K, cannot be detected in dilatometry. In the magnetostriction and in thermal-expansion measurements in applied field anomalies linked to the changes of the spin structure can be found. The minima seen in magnetostriction for $\text{Dy}_2\text{Ti}_2\text{O}_7$ and $\text{Ho}_2\text{Ti}_2\text{O}_7$ at around 1.5 T (fig. 4.5) and 1.8 T (fig. 4.9), respectively, coincide with the phase transition in magnetization measurements when corrected for demagnetization. The gradual breaking of the spin-ice order may be seen as a decrease of the relative length with increasing temperature. While the magnetostriction measurements show similar qualitative behavior of $\text{Dy}_2\text{Ti}_2\text{O}_7$ and $\text{Ho}_2\text{Ti}_2\text{O}_7$ the large difference of the magnitudes of the effects in both compounds could not be explained. In my simulation, which I outlined earlier in this section, I could reproduce the peak-valley anomaly observed in $\text{Dy}_2\text{Ti}_2\text{O}_7$, fig. 4.13. The minimum at H_c is caused by the competition of crystal-field striction and exchange striction in comparable amplitude. The gradual relative expansion with magnetic field in the spin-ice and kagome-ice phase and in the saturated-ice phase is caused crystal-field striction alone.

Hysteresis Several groups have measured the thermal conductivity of the spin ices $\text{Dy}_2\text{Ti}_2\text{O}_7$ and $\text{Ho}_2\text{Ti}_2\text{O}_7$ [80–83]. The measurements are consistent with each other; therefore, I constrain myself to the discussion of the measurements of Scharffe *et al.* [80]. The field dependence of the thermal conductivity κ of $\text{Dy}_2\text{Ti}_2\text{O}_7$ at 0.4 K is shown in fig. 4.15.

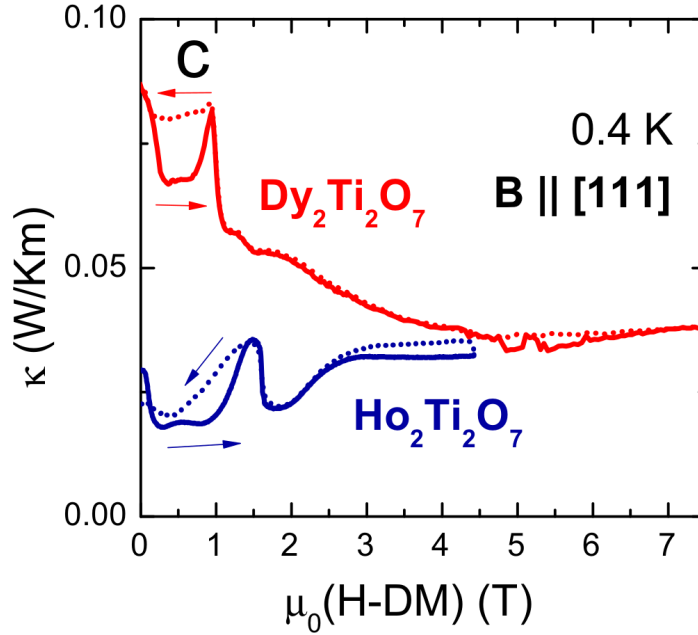


Figure 4.15.: Field dependence of the thermal conductivity of $Dy_2Ti_2O_7$ and $Ho_2Ti_2O_7$ showing a hysteresis in the kagome-ice region below 1 T in $Dy_2Ti_2O_7$ and 1.5 T in $Ho_2Ti_2O_7$. Reproduced from [80].

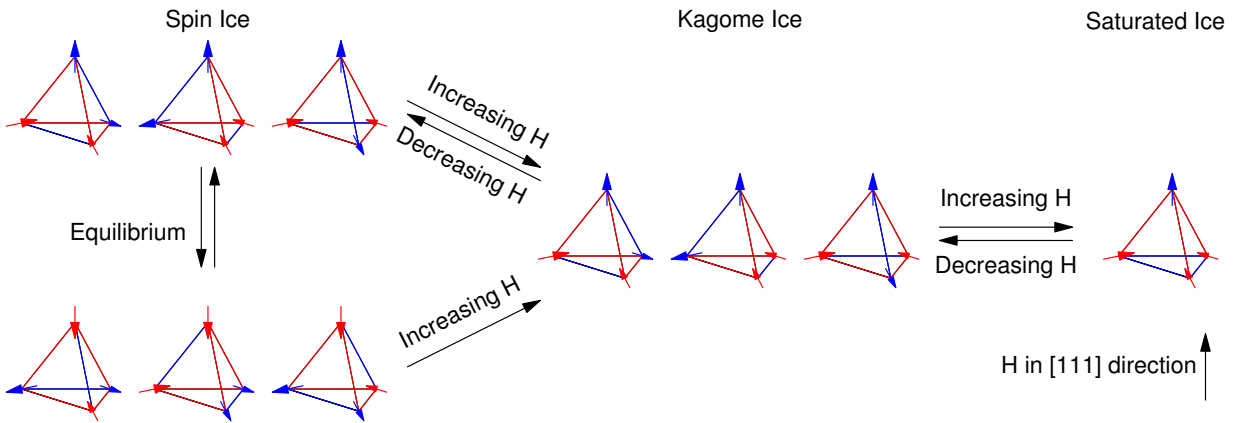


Figure 4.16.: Explanation of the hysteresis seen in the kagome-ice phase. The six spin-ice configurations go over into the kagome-ice configurations when increasing the field. Upon further increasing the field the long-range ordered saturated-ice phase is stabilized. Decreasing the field from there into the kagome ice phase is completely symmetric to the upswEEP. Decreasing the field back to zero the system only realizes a subset of the six possible spin-ice configurations. The remaining three configurations are reached through equilibration with temperature-dependent time-scale.

Sweeping up from zero-field there is a strong decrease of κ which plateaus from 0.3 to 0.7 T. Then rising again to peak at around 1 T and decrease with increasing field. In the downsweep, κ follows mostly the upsweep until the peak at 1 T and staying almost constant down to 0.2 T joining the upsweep curve down to zero field. The field dependence of κ of $\text{Ho}_2\text{Ti}_2\text{O}_7$ is very similar except for the critical fields and the behavior at fields higher than 1.5 T where κ peaks and, after going through a minimum, saturates at around the same value as the peak. In downsweep, κ does not stay constant below the critical field of 1.5 T but decreases steadily and joins the upsweep curve at around 0.2 T.

Using fig. 4.16, the phenomenological explanation for the hysteresis of the authors of Ref. [81] is the following: In the spin-ice state there are six possible states that satisfy the spin-ice rule that are all equally probable in equilibrium at zero field; left side of the figure. Increasing the magnetic field along $[1\ 1\ 1]$ direction favors order on the triangular sublattice of the apical spins while still satisfying the spin-ice rule with the spins on the kagome sublattice. Only three of the spin-ice states are favorable at these intermediate fields; middle part of fig. 4.16. A tetrahedron may thus be in two configurations: (a) the apical spin points along field direction; or (b) the apical spin points against field direction. In the configuration (a), no spin has to flip (top configurations of left part); while in configuration (b) the apical spin has to flip and another spin in the basis of the tetrahedron has to flip in order to satisfy the ice rule (bottom configurations of left part). The possible cause for the hysteresis is the existence of tetrahedra with both configurations during upsweep, whereas during downsweep only tetrahedra of configuration (a) exist. During upsweep tetrahedra in configuration (b) behave in a dynamic manner. At first, the apical spin flips in order to reduce its Zeeman energy at the expense of the exchange energy by creating an intermediate state of a tetrahedron with a 3-in-1-out or 1-in-3-out configuration. The tetrahedron can decrease its exchange energy by flipping one of the spins at its basis at the same time reducing Zeeman energy of this spin. The intermediate first step of this process maybe metastable and may be the reason for the hysteresis and the dynamic behavior during upsweep.

Increasing the field further also aligns the spins on the kagome plane to point along their local $[1\ 1\ 1]$ direction with positive projection on the magnetic field vector; right part of fig. 4.16. This breaks the spin-ice configuration and creates a long-range-ordered state of alternating 3-in-1-out and 3-out-1-in tetrahedra.

Decreasing the field from there flips again the one spin on the kagome sublattice, being the reverse of the process when sweeping up the field. Upon further decreasing the field to zero from the kagome-ice phase with three possible configurations down to the spin-ice phase does not recover immediately the equilibrium of equal population of all six possible

spin-ice configurations. Depending on the fluctuation time scale of the system, which is very slow at temperatures below 1 K, the system may remain out of equilibrium for a long time. It should also be noted that in order to recover those spin-ice states, which have the apical spin point against the field direction, two spin flips are needed to satisfy the spin-ice rule: one flip of the apical spin and one flip of a spin in the basis. In conclusion, there are two hysteretic regions that may be explained with this microscopic picture: Firstly, a hysteretic region around the transition from the spin-ice to the kagome-ice state found in magnetization at low fields between 0 T and 0.25 T [77]. During upsweep the system leaves the equilibrium and during the downsweep it has to relax back to equilibrium, which might open the hysteresis. Secondly, the hysteretic region in the kagome-ice phase observed in the thermal conductivity measurement and in my magnetostriction measurements at 0.3 K for both $Dy_2Ti_2O_7$ and $Ho_2Ti_2O_7$ (figs. 4.5 and 4.9). At the transition from spin-ice to kagome-ice state the system becomes out of equilibrium whereas at the transition from saturated-ice phase to kagome-ice it remains close to equilibrium. Even though, magnetostriction as a bulk characterization and the thermal conductivity as a transport characterization are not easily compared, there seems to be a common cause for the hysteresis, which might be the explanation above.

Dynamic effects In order to link the known phase diagrams (figs. 4.1 and 4.2) to the magnetoelastic properties, I finish the with ultrasound measurements by Erfanifam *et al.* [19]. They have found interesting dynamical magnetoelastic behavior in $Dy_2Ti_2O_7$, I comment on later in a separate paragraph, and a first order transition at H_c . The low-field transition is not observable. In $Ho_2Ti_2O_7$ no first order transitions are observed in the ultrasound measurements, instead a broad maximum at 1 T and a broad minimum at 2 T followed by a steady increase of the ultrasound velocity with higher fields was measured. Effectively, no difference between the ultrasound velocity at 0.29 K and 1.5 K could be found.

Dynamic effects in $Dy_2Ti_2O_7$ were already observed with other measurement techniques: for instance, as rapid changes of the magnetization called avalanches [84, 85] and transient changes of the ultrasound velocity [86]. Especially, since the ultrasound measurements probe the magnetoelastic properties of the system it might be expected to find similar effects also in magnetostriction measurements. At low temperatures and slow sweep rates, the dynamic effects in the ultrasound were visible as shark-fin-shaped peaks for $Dy_2Ti_2O_7$. These were attributed to avalanches of magnetic monopoles running through the lattice and releasing heat and raising the temperature. Due to the sensitivity of the ultrasound velocity on the temperature the heating and cooling were visible in the experiments. However, in

my dilatometric measurements no such dynamic effects were seen for $\text{Dy}_2\text{Ti}_2\text{O}_7$ at any sweep rate. On the one hand, this is probably due to the weak thermal expansion at these low temperatures, as can be seen in fig. 4.4. On the other hand, the temperature of the sample was also well fixed because of thermalization with the big mass of the dilatometer cell. From measurements of the magnetocaloric effect of $\text{Dy}_2\text{Ti}_2\text{O}_7$ [87] an estimate of the temperature change of around 0.5 K can be obtained. In any case this does not seem enough to cause significant thermal expansion.

Difference between upsweep and downsweep thermal expansion Both, $\text{Ho}_2\text{Ti}_2\text{O}_7$ and $\text{Dy}_2\text{Ti}_2\text{O}_7$, show a difference in thermal expansion measurement during increasing and decreasing temperature. For $\text{Dy}_2\text{Ti}_2\text{O}_7$, the upsweep and downsweep curves meet at around 0.6 K and are identical above that temperature; for $\text{Ho}_2\text{Ti}_2\text{O}_7$, the upsweep and downsweep curves are very different from each other, suggesting dynamics far from equilibrium. In particular the strong change of the relative expansion at 0.6 K in $\text{Ho}_2\text{Ti}_2\text{O}_7$ at all fields hints to the strong spin freezing below that temperature. In the next chapter, I will discuss this in detail.

5. Dynamic magnetoelastic properties of $\text{Dy}_2\text{Ti}_2\text{O}_7$ and $\text{Ho}_2\text{Ti}_2\text{O}_7$

In this chapter, I highlight a dynamic effect of the spin ices $\text{Dy}_2\text{Ti}_2\text{O}_7$ and $\text{Ho}_2\text{Ti}_2\text{O}_7$ which I have measured as slow lattice relaxation. Both spin ices, $\text{Dy}_2\text{Ti}_2\text{O}_7$ and $\text{Ho}_2\text{Ti}_2\text{O}_7$, were probed with the field-quench sequences shown in section 3.3. After a quick change of the magnetic field, the field quench, the lattice changed quickly and then a slow relaxation to some equilibrium lattice expansion followed. In section 5.1, these new results for $\text{Dy}_2\text{Ti}_2\text{O}_7$ and $\text{Ho}_2\text{Ti}_2\text{O}_7$ are presented. In view of existing theoretical predictions and other measurements these results are discussed in section 5.2.

5.1. Results

This section begins with a paragraph showing that lattice relaxations indeed occur in the spin-ice compounds $\text{Dy}_2\text{Ti}_2\text{O}_7$ and $\text{Ho}_2\text{Ti}_2\text{O}_7$. I used sequence A for $\text{Dy}_2\text{Ti}_2\text{O}_7$ and sequence B for $\text{Ho}_2\text{Ti}_2\text{O}_7$ to probe for relaxation effects with similar results. In the following subsections, I show more details of the relaxation times separately for $\text{Dy}_2\text{Ti}_2\text{O}_7$ and $\text{Ho}_2\text{Ti}_2\text{O}_7$ in sections 5.1.1 and 5.1.2, respectively.

Occurrence of lattice relaxation – Sequence A and B For $\text{Dy}_2\text{Ti}_2\text{O}_7$, I used sequence A, stepping the field up and down in steps of 0.5 T and waiting time of 30 or 60 min, to obtain an overview of the occurrence of lattice-relaxation effects. Typical relaxation data for $\text{Dy}_2\text{Ti}_2\text{O}_7$ in longitudinal and transverse geometry are shown in fig. 5.1 for various temperatures. These plots display the lattice expansion in dependence of time; panel (a) shows the measurements in longitudinal geometry, panel (b) the ones for the transverse geometry. The magnetic field was changed from 1.25 T down by 0.5 T and then stabilized for 30 min at 0.6 K and for 1 h at lower temperatures. The general behavior can be very well illustrated for the data taken at 0.3 K in fig. 5.1 (a). During the quick field sweep, the lattice contracts quickly, but after the field reaches its final value and does not change anymore, the lattice still continues to contract very slowly even after 1 h. In compari-

son with that, shown in the same panel, the lattice change stops after about 10 min at 0.6 K. The relaxation is slower at lower temperatures. The same trend is also seen in the transverse-geometry experiment shown in fig. 5.1 (b). The noise level in the transverse measurement smaller than in the longitudinal geometry because of the sample geometry with larger width and small thickness (table 3.3) Most of the measurements were performed in longitudinal geometry which are presented further below.

In the case of Ho₂Ti₂O₇, I used sequence B, sweeping the field up to 2.5 T and stepping down in steps of 0.5 T and waiting time of 30 or 60 min, to probe the relaxation effects in a first investigation. An example of the result of such an experiment is displayed in fig. 5.2 for various temperatures. The figure shows the time dependence of the lattice expansion, after changing the magnetic field quickly from 1.0 T to 0.5 T similar as in fig. 5.1 for Dy₂Ti₂O₇. Clearly, a slow relaxation is visible over a period of 60 min at 0.3 K. Compared to the relaxation at 0.5 K and 0.7 K it is much slower.

In the following subsections, I will explain more details of the results of the relaxation measurements on Dy₂Ti₂O₇ and Ho₂Ti₂O₇ in subsection 5.1.1 and subsection 5.1.2, respectively.

5.1.1. Results for Dy₂Ti₂O₇

The analysis of the results was done in the following steps. In order to get more insight into the relaxation effects, I needed some model to fit for the relaxation time. From the overview measurements it was apparent that some exponential decay law might be adequate to fit the data, but the exact form is not a priori known. Therefore, I used a very-long-time relaxation measurement to determine the relaxation law. In subsequent studies using sequences A-E, described in the experimental section 3.3, I investigated the relaxation under various conditions.

Very-long-time relaxation In order to get an idea what kind of decay law was adequate to fit the data best, I performed an experiment with a very long time of over 9 h after a quick field sweep to monitor the time dependence of the relative length change of the sample. The field was swept from 1.25 T to 0.75 T at a temperature of 0.3 K; this is shown in fig. 5.3. Possible models would be a simple exponential decay with one relaxation time, and a stretched exponential decay:

$$(\Delta L/L)(t) = (\Delta L/L)(t_0) + Ae^{-(t-t_0)/\tau}, \quad (5.1)$$

$$(\Delta L/L)(t) = (\Delta L/L)(t_0) + Ae^{-((t-t_0)/\tau)^\beta}, \quad (5.2)$$

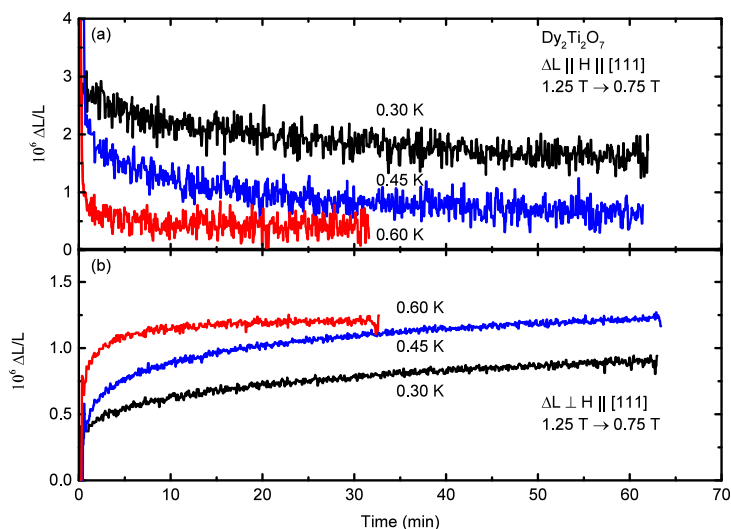


Figure 5.1.: Time dependence of the relative sample length of $\text{Dy}_2\text{Ti}_2\text{O}_7$ after sweeping the field quickly from 1.25 to 0.75 T at various temperatures (a) in longitudinal geometry $H \parallel \Delta L/L$ (excerpt of a measurement using sequence B) and (b) in transverse geometry $H \perp \Delta L/L$ (excerpt of a measurement using protocol A)

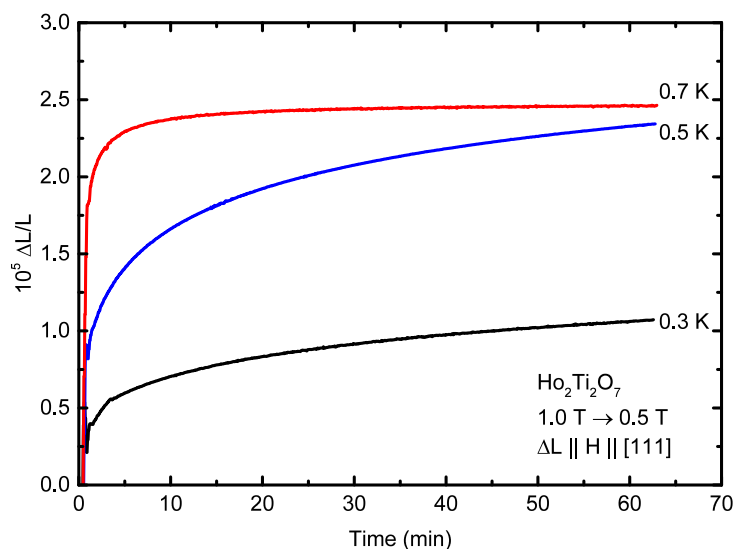


Figure 5.2.: Time dependence of the relative sample length of $\text{Ho}_2\text{Ti}_2\text{O}_7$ after sweeping the field quickly from 1 to 0.5 T (excerpt of protocol B).

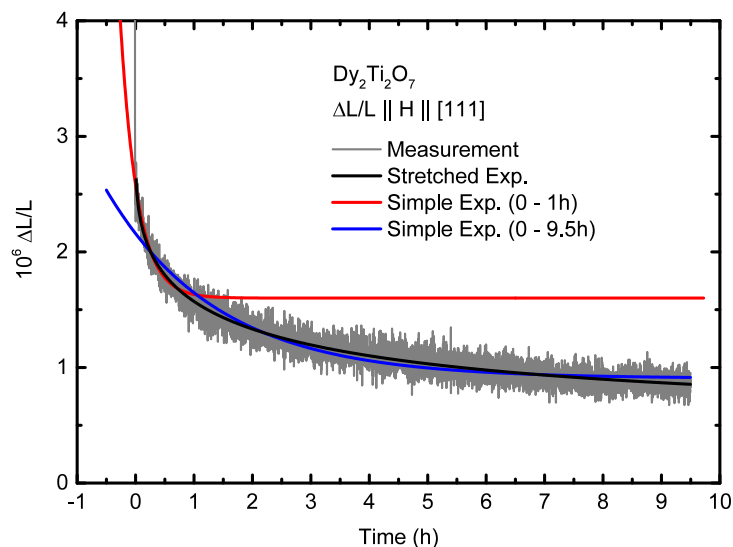


Figure 5.3.: Experiment with a long time of monitoring the relaxation after a quick field sweep from 1.25 to 0.75 T in a measurement using a sequence of type B.

where τ is the relaxation time and β an exponent. For both decay equations, t_0 was fixed to the end of the field change and the curve described with the free parameters $(\Delta L/L)(t_0)$, A and τ for both equations and additionally β for the stretched exponential fit. The parameters were found by a least-squares algorithm. In fig. 5.3 the long-time relaxation data are shown together with a stretched-exponential, a simple exponential describing the data in the first hour after the field sweep and a simple exponential describing all the data after the field sweep. It can be seen that the both simple exponentials deviate significantly from the data either in the beginning or in the end (red and blue curve in fig. 5.3). A simple exponential decay does not well describe the lattice relaxation and the relaxation time I extract using this assumption may not be accurate. The next more complex decay equation is the stretched exponential, where the exponent β is introduced. This model is motivated by two points: Firstly, the observation that the exponential-decay fit for 1 h saturates too early and should be stretched over longer times. Secondly, the idea that the decay of possible excitations in the sample might be obstructed by their mutual interactions as is put forward by theoretical investigations of the spin-ice model [62, 88]. The parameters of the stretched exponential describing the data best are the exponent $\beta = 0.4$ and a relaxation time $\tau = 5500$ s. Due to the high time consumption only one very-long-time measurement was done and the other measurements had to be performed on shorter timescales. I could still get good estimates of the relaxation time τ by fixing β to the well-determined value of 0.4.

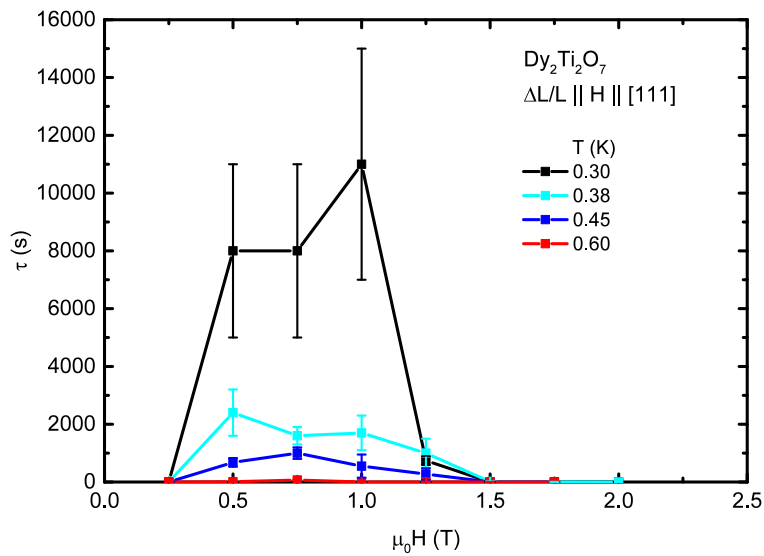


Figure 5.4.: Field dependence of the relaxation times of $\text{Dy}_2\text{Ti}_2\text{O}_7$ in experiments using sequences A and B at various temperatures.

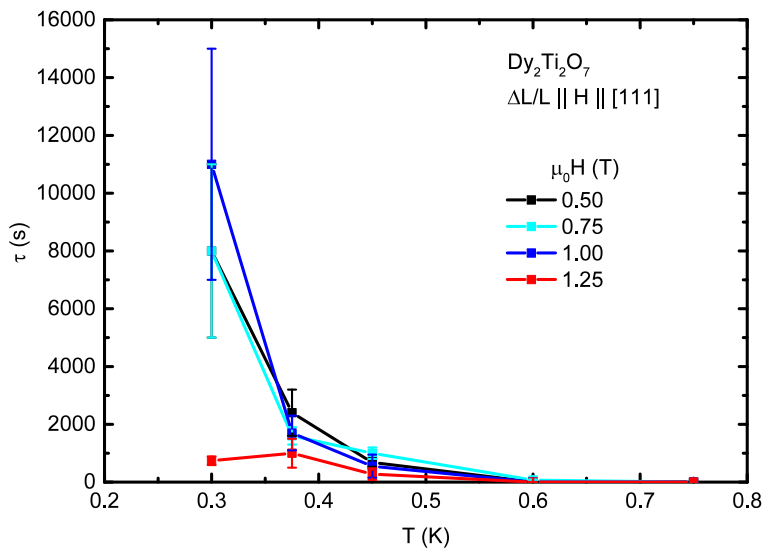


Figure 5.5.: Temperature dependence of the relaxation times of $\text{Dy}_2\text{Ti}_2\text{O}_7$ in experiments using sequences A and B at various fields of 0.5 to 1.25 T.

Quenches to and within the kagome-ice phase – Sequence A and B Sequence A in the down-stepping phase and sequence B set the system to the saturated-ice phase in the beginning and followed by a sweeping the field down in several steps from there. That means that the relaxation times at 0.5 T and 0.75 T are not reached in one step from the saturated-ice phase. For the measurements at 0.3 K the waiting time was chosen to 7200 s (2 h), for 0.38 K and 0.45 K it was waited for 3600 s (1 h) and for 0.6 K only 1800 s (30 min). I obtained the relaxation times from these sequences by fitting the stretched exponential function using eq. (5.2) with $\beta = 0.4$ (obtained from the very-long-time relaxation experiment) and t_0 fixed to the end of the field sweep. The error bars were determined by fixing τ_0 to other values around checking whether the data could be described with another set of A and $\Delta L/L(t_0)$ with this new τ_0 . The difference to the largest τu_0 for which this was possible is the error of τ_0 . Figure 5.4 shows the field dependence of the relaxation time of Dy₂Ti₂O₇. A lattice relaxation could not be observed at fields below 0.25 T and above 1.25 T. The longest relaxation times were measured in the field region between 0.5 and 1.0 T and a fast relaxation at 1.25 T. The time scale of the relaxation are hours for 0.3 K and few minutes at 0.6 K. Relaxation is, therefore, only observed in the kagome-ice region below the ordered high-field phase, the saturated-ice phase [69, 89].

Figure 5.5 shows the temperature dependence of the relaxation times at those field where long relaxation times were measured, compare with fig. 5.4. The relaxation times increase strongly with decreasing temperature for the fields between 0.5 to 1.0 T. Above 0.75 K, no relaxation could be found. This matches approximately the spin-freezing temperature of Dy₂Ti₂O₇ 0.5 K [63].

Quenches from the saturated-ice phase to kagome-ice phase – Sequence C In another experiment, with quench sequence C, the field was quickly swept down from the high-field phase at 1.5 T into the spin-ice or kagome-ice phase below 1.2 T. The time-dependence of the relaxation after the field quench is shown in fig. 5.6. Lattice relaxation can be clearly seen for fields above and equal to 0.4 T. For the final fields below 0.4 T, the crystal reaches its equilibrium length at the end of the quench, while for the fields above 0.4 T the crystal contracts after the quench slowly to its new equilibrium length.

The relaxation times τ measured in this experiment at 0.3 K and at 0.55 K are shown in fig. 5.7. In general, τ is much larger at 0.3 K than at 0.55 K in accordance with the previous measurements. For 0.55 K τ is of the order of 100 s, and For 0.3 K it is 0 below 0.4 T and reaches values of the order of 5000 s above, i.e., much more than one hour. At 1.2 T an accurate estimate of the relaxation is difficult to obtain since the amplitude of

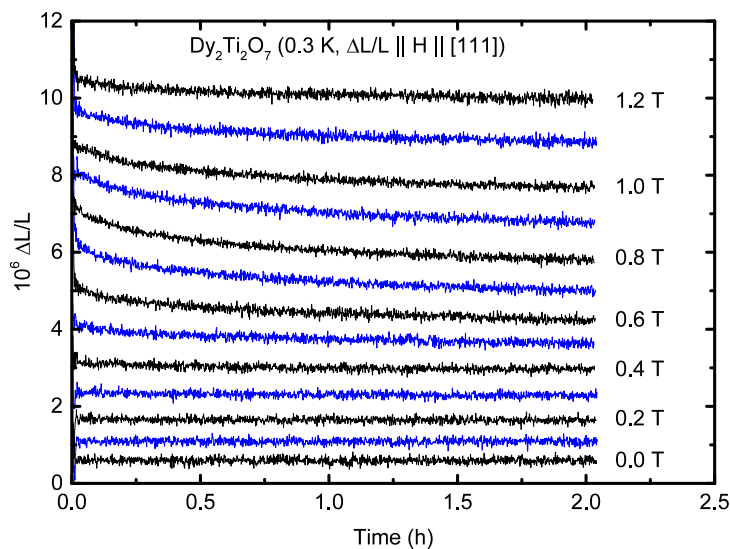


Figure 5.6.: Time dependence of the relative length change of $\text{Dy}_2\text{Ti}_2\text{O}_7$ after stabilizing the field at 1.5 T and then sweeping to a field from 0 to 1.2 T. The curves are shifted relative to each other.

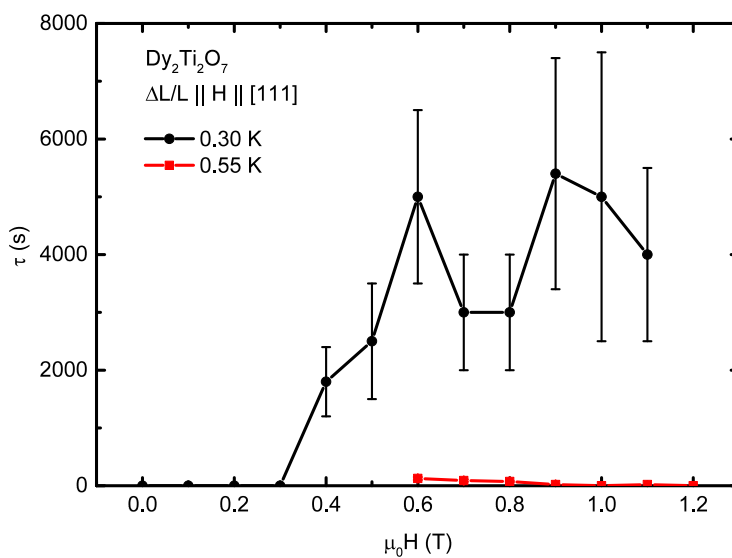


Figure 5.7.: The field dependence of the relaxation times of the lattice relaxations of $\text{Dy}_2\text{Ti}_2\text{O}_7$ shown in fig. 5.6.

the length change is much smaller compared to, for instance, at 0.8 T. In general, this experiment gives similar results as were already shown in fig. 5.4.

Quenches within the kagome-ice phase – Sequence D In this experiment, used Sequence D, one single field sweep from a chosen initial field by 0.5 T was performed. Figure 5.8 shows the field dependence of several of these sequences at 0.3 K with initial field of 1.1, 1.3, and 1.5 T. That means, in this experiment I also stabilize the system in the hysteretic region of the kagome-ice phase. In the graph, the colored curves are the relaxation measurements. They are overlaid on a point cloud of the magnetostriction of $Dy_2Ti_2O_7$ between 0 and 2.5 T during up- and downsweep. The upsweep curves of the slowly swept magnetostriction measurements and the quickly swept sequences are identical, showing that the upsweep magnetostriction is independent of the sweep rate. That means that the time scale of the dynamical processes during upsweep is much faster than the time scale of the sweep rate of 0.2 T/min. But at the final upsweep field, where the system is stabilized, the lattice expands slowly after reaching an initial field in the hysteresis, so there is dynamics with time scales slower than the 0.015 T/min of the magnetostriction measurement. Sweeping the field down quickly, the relative length changes less than during upsweep; in effect, it follows the magnetostriction data during downsweep obtained in the experiment with slow sweep rate. Finally, the lattice relaxes towards the middle of the hysteresis. The relaxation time is of the same order as in the previous measurements with sequence A, B and C.

Small Quench steps – Sequence E In a final experiment using sequence E (sweeping up and down the field in steps of 0.1 T within 6 s) length changes with similar relaxation times as with big step sizes were observed. Figure 5.9 displays the slow magnetostriction measurements at 0.3 K overlaid with a selection of measurements using sequences of type E with different starting fields. The relaxation was visible in the region from 0.5 T up to 1.4 T in both, upsweep quenches and downsweep quenches. However, the relaxation does not significantly leave the point cloud of the magnetostriction measurement and enters the hysteresis only slightly (red curve). In summary, the relaxation effects are observable for also for small step sizes and the relaxation time does not depend on the step size.

Phase diagram Finally, I assemble the relaxation times of the quench experiments of sequences A and B (quench steps of 0.5 T) from fig. 5.4 in a phase diagram of temperature and internal field (corrected for demagnetization effects), fig. 5.10. The internal field is calculated from the external field and the modeled magnetization via eq. (C.10). In

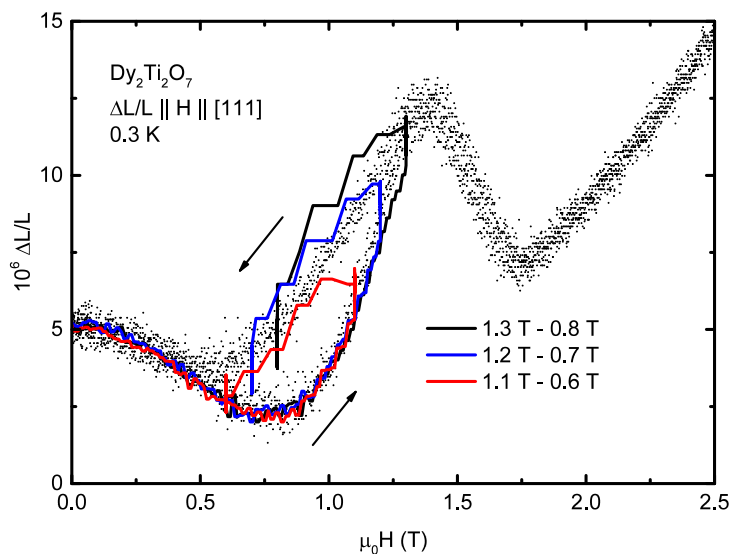


Figure 5.8.: Field dependence of the relative length change of $\text{Dy}_2\text{Ti}_2\text{O}_7$. The points show the magnetostriction data measured with a slow sweep rate of 0.015 T min^{-1} at 0.3 K . The lines show the magnetostriction measured at a fast upswEEP rate of 0.2 T min^{-1} to a field of 1.1, 1.2, and 1.3 T at 0.3 K . Then the field was swept down by 0.5 T at a rate of 1 T min^{-1} .

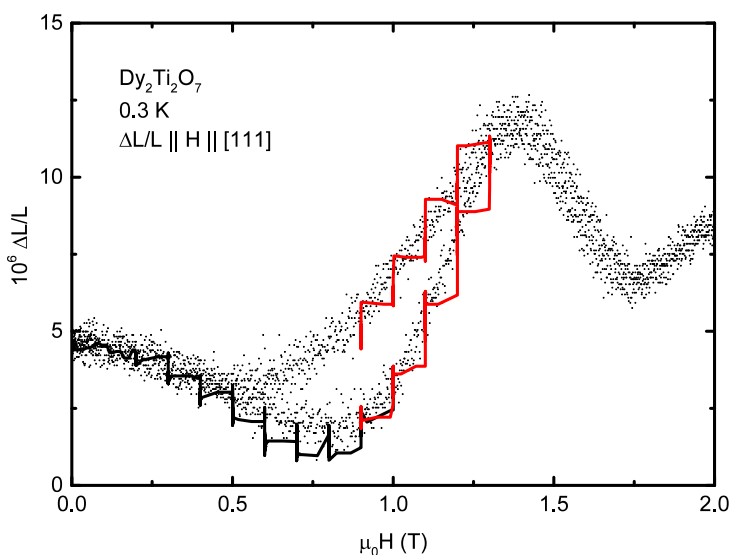


Figure 5.9.: Field dependence of the relative length change of $\text{Dy}_2\text{Ti}_2\text{O}_7$ in quench experiments with small quench steps (lines) compared to the slowly swept magnetostriction curve (dots). All data were taken at 0.3 K . The line curves show the magnetostriction curve at a fast upswEEP rate of 0.2 T min^{-1} to the initial field, then the field is quenched down in steps of 0.1 T at a rate of 1 T min^{-1} : from 0.2 T to 1 T (black) 0.9 T to 1.3 T down to 0.9 T (red).

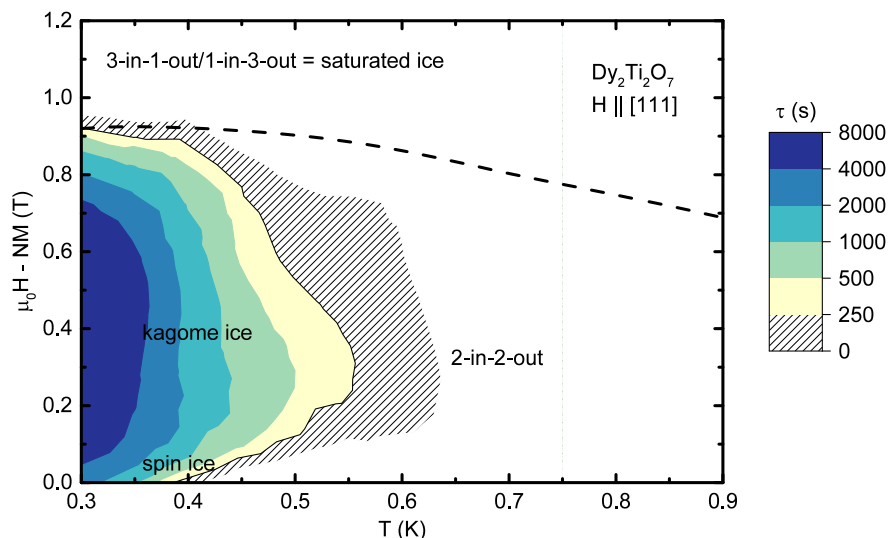


Figure 5.10.: Contour plot of the relaxation time in the phase space of temperature and internal field $\mu_0 H - NM$ (N is demagnetizing factor and M the magnetization) with long relaxation times in blue and short relaxation fading to lighter colors. The relaxation times are taken from the quench experiments of sequences A and B summarized in fig. 5.4. Note the exponential scale of the color scale from no relaxation in the white regions and increasing relaxation times to darker blue tones. For comparison, transitions extracted from specific-heat and magnetization data [69] are included as dashed line.

comparison with the phase diagram, fig. 4.1, extracted from specific heat and magnetization data [69], it can be seen that the lattice relaxation are observed below the transition from kagome-ice to saturated-ice phase (dashed line). The region of measureable relaxation times extends to a maximal temperature of around 0.65 K, the spin freezing temperature [90]; at higher temperatures no relaxation was observed. The longest relaxation times are found in the kagome-ice phase at low temperatures.

Summary of the results of the relaxation times I summarize the data with the following bullet points:

- The lattice relaxation follows a stretched-exponential law.
- The relaxation is seen in longitudinal and transverse magnetostriction.
- The relaxation is only seen in the region of the spin-ice and kagome-ice phase.
- The relaxation time is strongly temperature dependent and is not observed above the spin-freezing temperature of 0.65 K.

In the next section the results obtained for relaxation measurements at $\text{Ho}_2\text{Ti}_2\text{O}_7$ are described.

5.1.2. Results for $\text{Ho}_2\text{Ti}_2\text{O}_7$

In order to prove that $\text{Ho}_2\text{Ti}_2\text{O}_7$ shows relaxation effects similar to $\text{Dy}_2\text{Ti}_2\text{O}_7$ I conducted experiments with quench sequences of type A and B. The sequence A was employed as explained in section 3.3 and for sequence B the step size was chosen as 0.25 T instead of 0.1 T. In the beginning of this chapter, in fig. 5.2, I show that the lattice of $\text{Ho}_2\text{Ti}_2\text{O}_7$ indeed relaxes with long relaxation times after fast field sweeps. The curves at low temperatures and low fields can be fit with the stretched-exponential function, used also for the relaxation of $\text{Dy}_2\text{Ti}_2\text{O}_7$, eq. (5.2).

Kinks in the measurement At the lowest temperatures of 0.3 K in various fields the relaxation starts out quickly until there is a change of the relaxation time to higher values, i.e., slower relaxation, seen as a kink in the curve, fig. 5.11; a similar behavior is also seen at 0.4 and 0.5 K. The occurrence of this feature at several temperatures and various fields suggests that it is connected to some intrinsic effect and dynamics. However, the kink does not always happen at the same time after a quench for one specific temperature, as seen for example in fig. 5.11 for 0.3 K at 0.75 T. There is a trend that the change of the relaxation time happens earlier for higher temperatures, but this is not a strict rule as can be seen at 0.75 T for the two curves measured at 0.3 K having a kink earlier or later than the curve at 0.4 K. These features probably appear at all temperatures; but for higher temperatures it can happen already during the field quench so that it is not observable. The slowing down of the dynamics at the kink may be attributed to pinning of monopoles to defects in the lattice that act as pinning centers as discussed in [91]. A direct consequence of these kink features is that they make it difficult to obtain accurate estimates of the relaxation time and especially the values extracted from the measurements at 0.3 K are probably too low.

Relaxation times For the analysis of the lattice relaxation, I fixed t_0 and extracted τ and β just as for $\text{Dy}_2\text{Ti}_2\text{O}_7$. In general, the best fit value of β is about 0.5; for a better comparison of the relaxation times, I fixed β to exactly 0.5 and fit the other parameters. However, for the short relaxation times at high temperatures or at high fields a simple exponential-decay equation can also describe the data. A simple exponential-decay equation is the limit of the stretched-exponential decay with $\beta = 1$. In an investigation of the magnetization dynamics, an increase of β with temperature from 0.65 at 0.6 K to 1 at

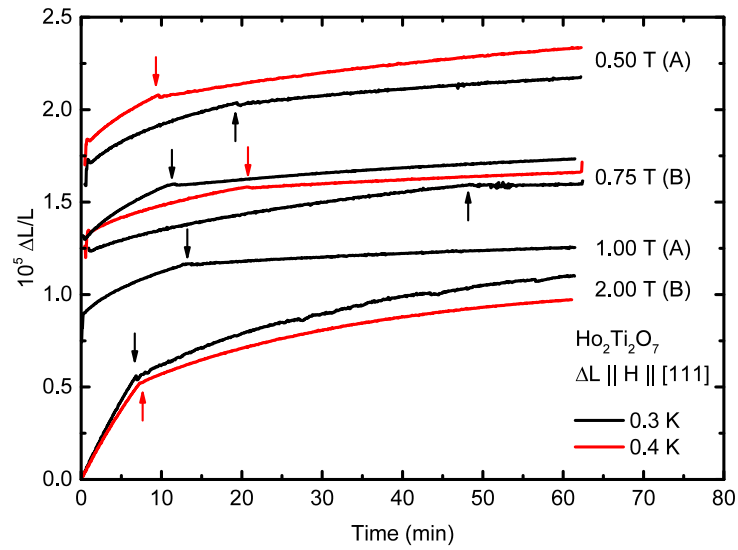


Figure 5.11.: Time-dependence of the relative length change after a quick field sweep down to fields of 0.5, 0.75, 1 and 2 T, either in an experiment using sequence A or B specified in the parentheses. Change of the relaxation times are seen as kinks in the curves and marked by arrows. The curves are offset with respect to each other.

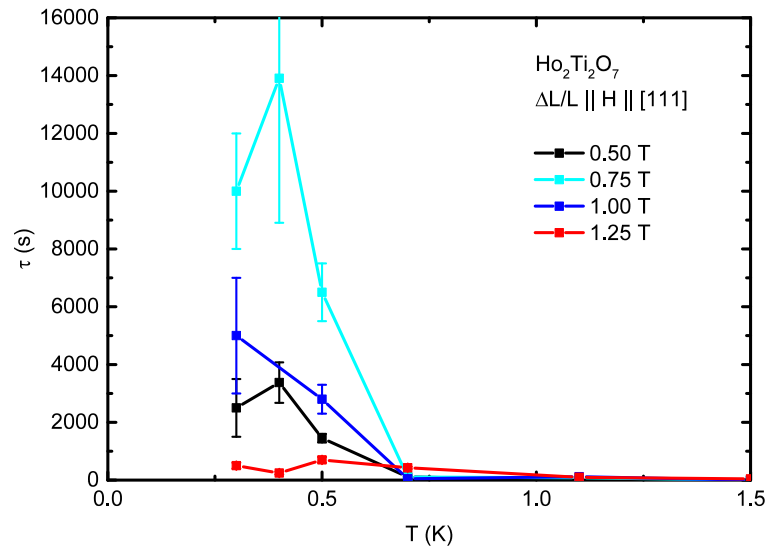


Figure 5.12.: Lattice relaxation times of $Ho_2Ti_2O_7$ in quench protocol A in dependence of the temperature after quenching down to fields of 0.5 to 1.25 T in a step of 0.5 T.

0.9 K was found [92]. In my dilatometric measurements, the data do not admit to confirm the values of β given in the magnetization measurements.

The temperature-dependence of the relaxation time is shown in fig. 5.12. The typical time scale of the relaxation changes from hours (more than 3600 s) at temperatures below 0.5 K to 600 s (10 min) at 0.7 K and to around 60 s (1 min) and shorter at 1.1 and 1.5 K. Highest relaxation times were found for fields between 0.5 T and 1.25 T. As explained above the estimation of the relaxation times at 0.3 K and 0.4 K is especially difficult, because of the kink feature where the relaxation time changes. The relaxation time is strongly temperature dependent and decreases with increasing temperature.

Figure 5.13 shows the field-dependence of the relaxation time of $\text{Ho}_2\text{Ti}_2\text{O}_7$ measured after fast field reductions in steps of 0.5 T per step using the quench protocol A. The relaxation time increases from 0 to 0.75 T and decreases again with higher fields until no relaxation with exponent $\beta = 0.5$ is seen at fields above 1.75 T. In summary, long relaxation times are found in the kagome-ice and spin-ice phase similar as for $\text{Dy}_2\text{Ti}_2\text{O}_7$.

Measurements of the relaxation time of $\text{Ho}_2\text{Ti}_2\text{O}_7$ with a smaller step size of the fast field sweeps of 0.25 T show similar results as for steps of 0.5 T showing the robustness of the result.

Phase diagram Figure 5.14 summarizes the relaxation times from figs. 5.12 and 5.13 and additional data sets not shown there in a phase diagram of temperature and internal field (demagnetization effects taken into account). The region where long relaxation times are observed was below 0.8 K and below an internal field of 1.5 T. This is the region of the kagome-ice and spin-ice phase with 2-in-2-out configurations. The region of where a relaxation is observed reaches to higher magnetic fields than for $\text{Dy}_2\text{Ti}_2\text{O}_7$, compare with fig. 5.10. This is consistent with the higher critical field for the transition from the kagome-ice to the saturated-ice phase [68] and signifies the larger magnetic interactions between the rare-earth ions.

Summary I would like to summarize the data for $\text{Ho}_2\text{Ti}_2\text{O}_7$ as I did for $\text{Dy}_2\text{Ti}_2\text{O}_7$. Lattice relaxation after fast field sweeps could be found in the low temperature regime below 0.8 K. The relaxation is strongly temperature-dependent with longer relaxation times at lower temperatures and highest at around 0.75 T; this corresponds with the kagome-ice phase. Additional features in the relaxation were found as kinks where the relaxation drastically changed its relaxation time. However, this effect is not exactly reproducible and happens after an unpredictable time interval after the field sweep. These time intervals are usually longer for lower temperatures.

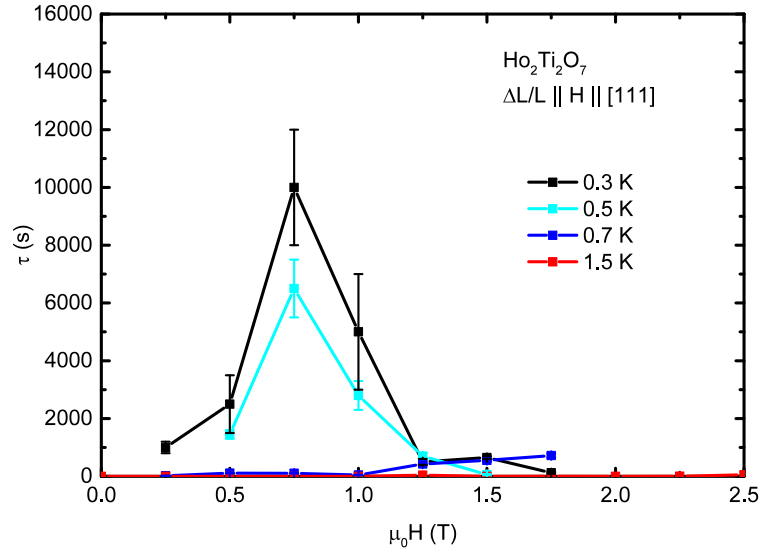


Figure 5.13.: Lattice relaxation times of $\text{Ho}_2\text{Ti}_2\text{O}_7$ in quench protocol A in the quenching down by 0.5 T.

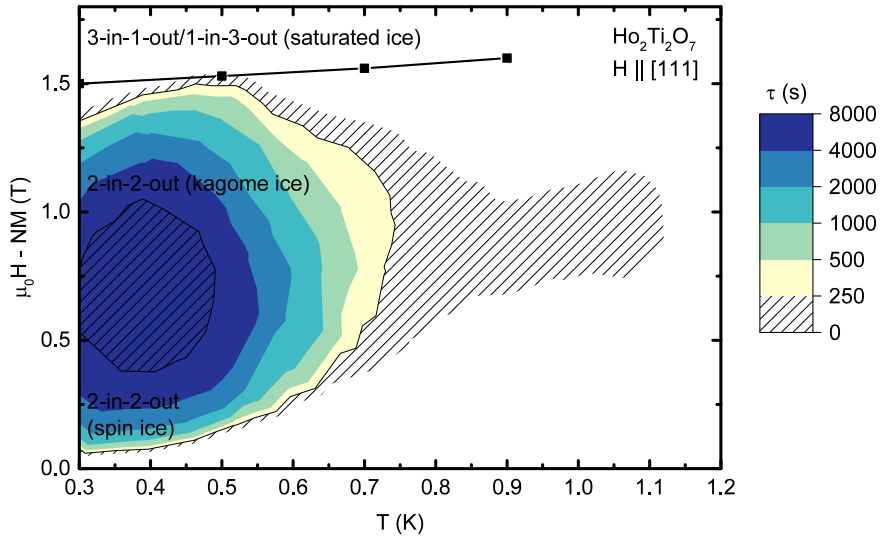


Figure 5.14.: Contour plot of the relaxation time of $\text{Ho}_2\text{Ti}_2\text{O}_7$ in the phase space of temperature T and internal field $\mu_0 H - NM$ (with N the demagnetizing factor and M the magnetization). The relaxation times are taken from the relaxation experiments using the sequence A shown in fig. 5.13 and additional data sets. Note the exponential scale of the color scale from no relaxation in the white regions and increasing relaxation times to darker blue tones. The transition to the saturated-ice state observed in the magnetization data published in [68] is included in the graph, as well.

5.2. Discussion

Possible parasitic thermal effects In view of the absence of publications on lattice relaxation effects I discuss possible parasitic effects that could look like intrinsic effects but are actually wrong measurements. At first, I consider thermal effects that either heat or cool the sample and the relaxation would just be the thermal expansion during an exponential creep to the equilibrium temperature. The temperature change might be due to some effect of the TDC. Therefore, I checked in additional measurements whether the empty cell would show relaxation effects. This was not the case. Consequently, the relaxation is an effect of the combination of the sample and the cell. Another spurious effect would be that the cell and the sample might change temperature during the quench experiment and expand or contract thermally. This might be due to eddy currents in the dilatometer cell caused by the fast change of the magnetic flux increasing its temperature in fast down and upsweep alike. I would expect $\Delta L/L$ to be positive and always a relaxation to shorter lengths. This is not what I observed. A last mechanism might be heating or cooling of the sample due to adiabatic demagnetization. The temperature would increase at upsweep and decrease at downsweep [87, 93]. However, such an effect is not likely since the sample is in good thermal contact with the dilatometer cell and should hardly change temperature. Therefore, I exclude that the observed relaxation is caused by thermal effects of the sample.

Possible parasitic torque effects In the appendix I discuss the possibility of torque acting on the sample if the field is not properly aligned along the [1 1 1] axis. In this case, the relaxation effects would rather be a measurement of the magnetic torque rotating the sample, which would appear as relative length change. The measurement results would be related to the anisotropic magnetization of the sample, instead of an intrinsic magnetoelastic property. I exclude, this for two reasons. First, I made a control measurement with the sample tightly glued to the screw fixing the sample in the TDC. Since the screw does not move with respect to the frame of the TDC which itself does not move with respect to the magnetic field, the the sample also is fixed relative to the magnetic field. This suppresses the rotation of the sample due to torque. I measured the same lattice relaxation effects as without gluing the sample, which is evidence for the relaxation being a real magnetoelastic effect. Secondly, the rotation of the sample would appear as an unphysical large magnetostrictive effect in the order of several percent, instead of 10^{-5} as was measured. Therefore, the relaxation effects I observed are indeed intrinsic magnetoelastic effects.

Dynamics of the spin ices The dynamic behavior in spin ice has been modeled in theory with the dynamics of the monopole excitations of 3-in-1-out tetrahedra in the ground state configuration of 2-in-2-out tetrahedra [61, 62]. An increase of the time scales of these dynamics has been found in these simulations. Likewise, the increase of the time scale of the internal dynamics has been observed in several different measurements on spin ice such as ac susceptibility [64, 90, 94–102], magnetization [85, 96, 103], magnetocaloric effect [87], ultrasound velocity [86], thermal conductivity [82] and heat capacity [104]. All of these methods show slow dynamics at temperatures below 1 K in the same order of magnitude as the lattice relaxation and have probably the same origin. It should be noted, that my method can probe especially well the kagome-ice phase where magnetization measurements would not see any change and, hence, no relaxation. Thermal quench experiments, where the temperature should be reduced quickly at zero field from above 1 K to below 0.5 K are experimentally challenging and are not likely to show dynamic effects because the thermal expansion is too weak at zero field. Theoretical studies on the monopole dynamics have been conducted for such thermal quenches [61]. In conclusion, the field quench experiments are the most elegant way to observe lattice dynamics in the spin-ice compounds and connect them to the monopole dynamics.

Origin of the slow dynamics The slow dynamics seen in various methods that use changing fields, such as ac susceptibility, magnetization or my dilatometric experiments are connected to the slow monopole annihilation dynamics after fast field sweeps [62]. The microscopic picture is that monopole-antimonopole pairs (3-in-1-out and 1-in-3-out configurations) on neighboring tetrahedra form stable bound pairs, that can neither annihilate nor move away from each other due to mutual interaction. Therefore, the monopole mobility or spin-flip rate is reduced. Consequently, the probability of the annihilation of monopoles is suppressed and it takes a long time for this process to happen. Additionally, monopole movement (spin flips) might be suppressed at defect sites of the lattice slowing down the intrinsic dynamics [91]; this was used to explain the difference between the long-time thermal relaxation in specific-heat measurements of the authors of [104] and their absence in measurements of other groups [105, 106].

6. Effects of the lattice on the magnetic properties of spin-ice studied via silicon substitution in $\text{Dy}_2\text{Ge}_{2-x}\text{Si}_x\text{O}_7$

In this chapter, I present a study of the influence of partially substituting the ion on the B site by a second ion. The parent compound investigated is $\text{Dy}_2\text{Ge}_2\text{O}_7$ and the substitution study is made with Si on the B site. The general idea behind this investigation is that by changing the lattice parameter a variation of the magnetic interactions in the pyrochlore might lead to another ground state than the spin-ice state or to a spin-ice ground state with different interactions between monopole excitations. The synthesis of pyrochlores with only Si on the B site is beyond the technical feasibility with state-of-the-art methods and may not be possible at all. Therefore, only partial substitution of SI on the B site is possible with the downside of introducing lattice disorder into the system.

This chapter reproduces the current status of a manuscript accessible on a preprint server [31] and submitted for publication; it is organized as follows. In section 6.1 I give more details on the background and motivation of this study building on the foundations given in section 3.2 in Part I. Then, I give the details of the experimental setup and the samples in section 6.2. Finally the results are presented in section 6.3 and discussed in section 6.4.

6.1. Background: Substitution dependence of the magnetic interactions

Lattice dependence of the effective nearest-neighbor interaction In the spin-ice compounds the main interactions between nearest-neighbor ions is the exchange interaction and the dipolar interaction. The exchange interaction between nearest-neighbor Dy^{3+} ions is conveyed via superexchange over oxygen. This superexchange depends strongly on the overlap of orbitals and, therefore, on the distance between ions. Hence, there is a strong

dependence of the nearest-neighbor exchange constant J_{nn} on the lattice parameter. Likewise, the dipolar interaction between nearest neighbor Dy^{3+} is also strongly dependent on the lattice parameter, although differently than J_{nn} , as shown in eq. (3.13). Thus, reducing the distance between the Dy ions changes the relative strengths of the dipolar versus the exchange interactions, D_{nn} and J_{nn} , respectively. The total effective interaction $J_{\text{eff}} = D_{\text{nn}} + J_{\text{nn}}$ is reduced shifting the compound closer to the phase boundary separating the spin-ice and AFM phase in the dipolar spin-ice model [54], see fig. 6.1. This principal phase diagram was proven experimentally by substituting the Ti on the B site of $\text{Dy}_2\text{Ti}_2\text{O}_7$ with a different ion with smaller or larger ionic radius, namely Ge or Sn, respectively [30].

Stability of the pyrochlore lattice As was pointed out in section 3.2, there is a limited region of stability for combinations of B site ions with Dy on the A site [28]. At ambient pressure, stable pyrochlores can be realized for ratios $1.36 < r_a/r_b < 1.71$ [6]. For comparison, the ratio of the ionic radii for Dy^{3+} on the A site and Ti^{4+} , Ge^{4+} , and Si^{4+} on the B site are 1.70, 1.94, and 2.57, respectively. Under high hydrostatic pressure during synthesis, the stability range can be extended towards smaller r_b and also $\text{Dy}_2\text{Ge}_2\text{O}_7$ can be synthesized. The resulting pyrochlores persist metastable also under ambient pressure conditions. The next challenge is to synthesize a material with an even smaller B -site ion than Ge, such as Si. However, to grow such a pyrochlore would need pressures beyond what is currently possible technologically. Therefore, only partial substitution of Si for Ge has been achieved; at the same time as reducing the lattice constant of the compound, also disorder is introduced.

Lattice disorder While disorder is well discussed in terms of order-by-disorder effects in connection to quantum-spin-ice candidates [107], disorder in the spin-ice pyrochlores is discussed in view of slow monopole dynamics [88, 108] or the absence of the residual Pauling entropy [106]. Importantly, various kinds of lattice defects [109] should be taken into account when dealing with these compounds, such as vacancies (particularly of oxygen [108]) and stuffing, i.e., inserting A site ions on the B site [110–112]. Specifically, stuffing would induce magnetic ions on the nonmagnetic B -site sublattice; likewise, oxygen vacancies would change the oxidation states of neighboring ions changing their magnetic state. Disorder reduces the symmetry and, therefore, influences the crystal electric field perturbatively, possibly introducing transverse exchange couplings and increasing the quantum character of the spin-ice ground state.

6.2. Experimental

Sample preparation and quality Polycrystalline Dy germanate, $\text{Dy}_2\text{Ge}_2\text{O}_7$, and polycrystalline silicone-substituted $\text{Dy}_2\text{Ge}_{2-x}\text{Si}_x\text{O}_7$ samples with $x = 0.02, 0.08,$ and 0.125 were synthesized by Mathis Antlauf, TU Bergakademie Freiberg, similar as described previously [29, 113]. He confirmed the phase purity via SEM/EDX analysis (Carl Zeiss LEO 1530) for all samples and via x-ray powder diffraction at the ALBA synchrotron light source in Barcelona, Spain, for $\text{Dy}_2\text{Ge}_2\text{O}_7$ and by using a Seifert diffractometer (FPM URD6) in symmetric Bragg-Brentano-Geometry with Cu anode for $\text{Dy}_2\text{Ge}_{2-x}\text{Si}_x\text{O}_7$ with $x = 0.02, 0.08$ and 0.125 . The sintered polycrystals are of dark to light-gray color, as fig. 6.2 shows for the crystal with $x = 0.02$.

The determination of the crystal quality was also done by Mathis Antlauf. The diffraction data of unsubstituted Dy germanate confirmed the cubic pyrochlore structure ($Fd\bar{3}m$, 227) with a lattice constant of $a = 9.930 \text{ \AA}$, which is in excellent agreement with the literature data ($a = 9.929 \text{ \AA}$ [29]). Rietveld refinements show that the pyrochlore structure can well describe the diffraction patterns of $\text{Dy}_2\text{Ge}_{1.98}\text{Si}_{0.02}\text{O}_7$, $\text{Dy}_2\text{Ge}_{1.92}\text{Si}_{0.08}\text{O}_7$ and $\text{Dy}_2\text{Ge}_{1.875}\text{Si}_{0.125}\text{O}_7$ (the latter is shown in fig. 6.3) with lattice constants $a = 9.924 \text{ \AA}$, 9.912 \AA and 9.906 \AA , respectively. For these samples, the best fit was achieved by assuming a statistical substitution of Ge with Si on the B site of the pyrochlore structure with exactly the Si concentration of the starting-material mixtures. In particular, Si is not interstitially incorporated into the crystal. There were no signs for chemical inhomogeneities or additional phases in XRD or SEM investigations (fig. 6.3).

Magnetic and thermodynamic measurements of $\text{Dy}_2\text{Ge}_{2-x}\text{Si}_x\text{O}_7$ I performed magnetization measurements of all $\text{Dy}_2\text{Ge}_{2-x}\text{Si}_x\text{O}_7$ using a commercial SQUID magnetometer (MPMS) and a vibrating-sample magnetometer in magnetic fields up to 7 T. Magnetic ac-susceptibility measurements were performed by Tino Gottschall and Jacob Hornung (Dresden High-Magnetic-Field Laboratory, Helmholtz-Zentrum Dresden-Rossendorf) in a compensated coil-pair susceptometer at frequencies ranging from 4 to 1293 Hz down to a temperature of 0.3 K using a commercial ^3He system. The temperature was measured with a RuO_2 resistance thermometer for the ac-susceptibility measurements. The heat capacity of $\text{Dy}_2\text{Ge}_2\text{O}_7$ and $\text{Dy}_2\text{Ge}_{1.875}\text{Si}_{0.125}\text{O}_7$ was measured by Tino Gottschall and Jonas Gronemann (Dresden High-Magnetic-Field Laboratory, Helmholtz-Zentrum Dresden-Rossendorf) in a ^3He sorb-pumped cryostat using the relaxation-time method and a carefully calibrated RuO_2 thermometer.

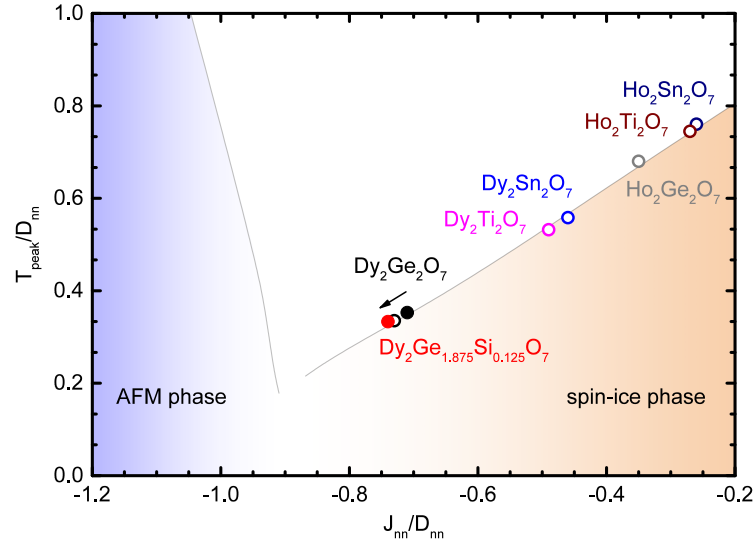


Figure 6.1.: Phase diagram of the dipolar spin-ice model including the positions of several spin-ice compounds and the phase boundaries of the antiferromagnetic (AFM) and the spin-ice phase. Literature values are shown as open circles, filled symbols stand for the samples from this work. J_{nn} and D_{nn} denote the exchange and dipolar interaction between nearest neighbors, respectively. T_{peak} denotes the temperature of the peak in the heat capacity associated with the spin-ice phase (adapted from Zhou *et al.* [30]).

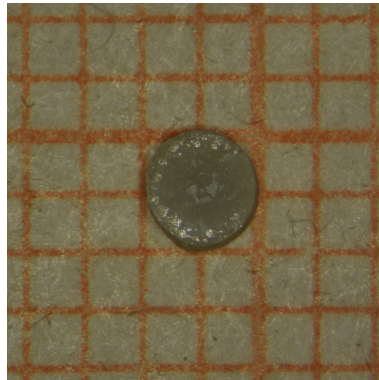


Figure 6.2.: $\text{Dy}_2\text{Ge}_{2-x}\text{Si}_x\text{O}_7$ sample with $x = 0.02$ synthesized by Mathis Antlauf.

6.3. Results

Magnetization In fig. 6.4, the magnetization per Dy ion of the sample series is shown as a function of magnetic field measured at 5 K and consistent with the literature data of the analogue compound $\text{Dy}_2\text{Ti}_2\text{O}_7$ [114]. The field dependence of the magnetization is well described by a powder-averaged Boltzmann distribution of non-interacting paramagnetic Ising spins (dash-dotted curve) resulting in a magnetic moment of $5 \mu_B$ at saturation while the Heisenberg model (no anisotropy) or the case of XY anisotropy would result in a magnetization much larger than measured. It should be noted that the magnetization values at the maximum field do not systematically depend on the Si concentration. The deviations can be attributed to the use of polycrystalline samples which, due to the growing process, may contain a degree of texture which is not visible in the diffractograms. However, the low scattering of the measuring points shows the accuracy of the magnetization measurements. For the calculation of the D_{nn} the value of $10 \mu_B$ for the free moment was used. The Curie-Weiss temperature θ_{CW} of our $\text{Dy}_2\text{Ge}_2\text{O}_7$ sample is close to zero and consistent with the literature value[30]; the difference of θ_{CW} of the Si containing samples compared to $\text{Dy}_2\text{Ge}_2\text{O}_7$ is within the accuracy of the measurement of approximately ± 0.5 K.

ac susceptibility To detect distinct differences, we will focus our investigation for the remainder of this article on pure Dy germanate and the sample with the highest Si substitution, $\text{Dy}_2\text{Ge}_{1.875}\text{Si}_{0.125}\text{O}_7$. Figure 6.5(a) shows the real (χ') and imaginary part (χ'') of the ac susceptibility of the substituted and unsubstituted sample for three exemplary frequencies. The distinct frequency dependence is visible especially in χ'' . Both samples show sharp maxima which shift towards higher temperatures and smear out continuously at higher frequencies. At 16 Hz, $\text{Dy}_2\text{Ge}_{1.875}\text{Si}_{0.125}\text{O}_7$ has a peak temperature of 580 mK being about 50 mK lower than for $\text{Dy}_2\text{Ge}_2\text{O}_7$. Furthermore, it is observed that the increase of the peak temperature at higher frequencies is much less pronounced in the substituted compound. Demagnetization effects should not influence our following qualitative discussion, even though they can cause deviations of the measured susceptibility, for the absolute values as well as for the peak positions[97, 102]. They should cause similar changes for the equally shaped $\text{Dy}_2\text{Ge}_2\text{O}_7$ and $\text{Dy}_2\text{Ge}_{1.875}\text{Si}_{0.125}\text{O}_7$ samples; however, an analytical determination of the demagnetization factor for our disc-shaped samples is not possible.

Based on the ac-susceptibility results, the spin dynamics can be investigated further. At the peak temperature T_P of the imaginary part χ'' at a given attempt frequency f , the spin-relaxation time τ is related to f via $\tau = 1/2\pi f$. In fig. 6.5(b), the spin-relaxation time is plotted vs. the inverse of the temperature T_P . $\text{Dy}_2\text{Ge}_2\text{O}_7$ has two linear regions;

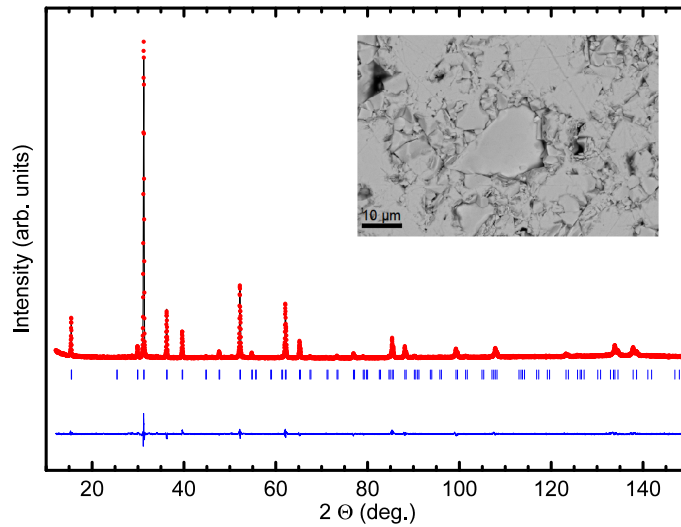


Figure 6.3.: Powder-diffraction pattern and Rietveld-difference plot for $\text{Dy}_2\text{Ge}_{2-x}\text{Si}_x\text{O}_7$ with $x = 0.125$, fitted for this stoichiometry. Inset: SEM micrograph of the polished sample surface, revealing crystallite sizes of up to approximately 15 μm .

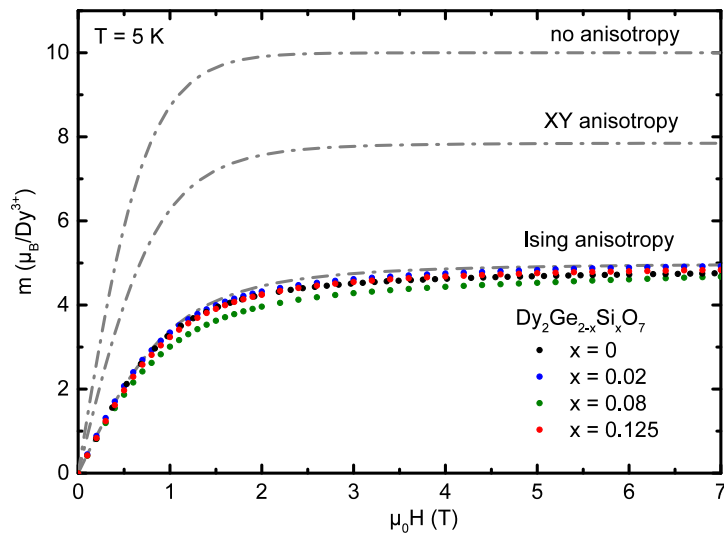


Figure 6.4.: Field dependence of the magnetization per dysprosium ion of $\text{Dy}_2\text{Ge}_{2-x}\text{Si}_x\text{O}_7$ with $x = 0, 0.02, 0.08$ and 0.125 at a temperature of 5 K. The symbols are measured values and the dash-dotted lines correspond to the powder-averaged Boltzmann distribution of spin-half spins with Ising anisotropy, XY anisotropy, and with no anisotropy, respectively.

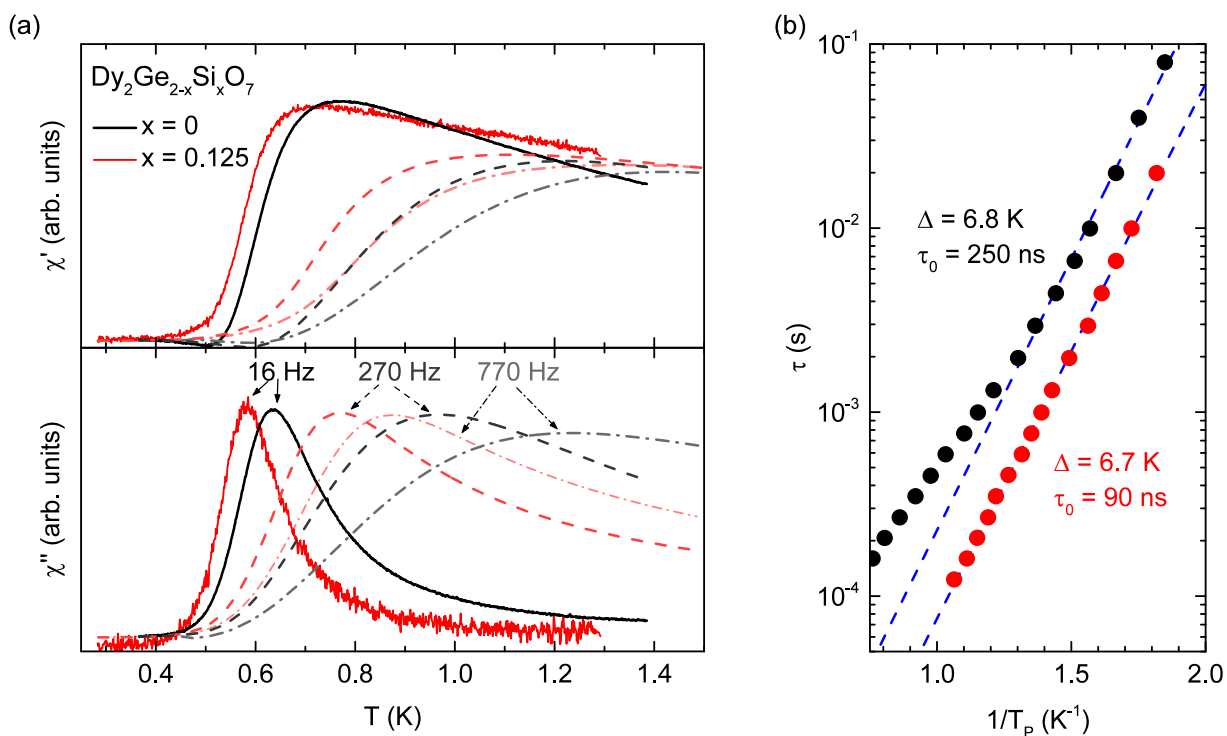


Figure 6.5.: (a) Real and imaginary part of the ac susceptibility χ' and χ'' of $\text{Dy}_2\text{Ge}_2\text{O}_7$ (black) and $\text{Dy}_2\text{Ge}_{1.875}\text{Si}_{0.125}\text{O}_7$ (red) at frequencies of 16 (solid), 270 (dashed), and 770 Hz (dash-dotted). (b) Spin-relaxation time $\tau = (2\pi f)^{-1}$ as a function of the inverse peak temperature T_P . Fits using the Arrhenius law with their respective energy barriers Δ are shown as dashed lines.

a high-temperature region above about 0.8 K that is less steep than the low-temperature region. In $\text{Dy}_2\text{Ge}_{1.875}\text{Si}_{0.125}\text{O}_7$ only one slope is found below 1 K. We focus our discussion on the low temperature region. At low measurement frequencies, the relaxation times seem to follow an Arrhenius law (dashed lines in fig. 6.5(b)):

$$\tau(T_P) = \tau_0 \exp\left(\frac{\Delta}{k_B T_P}\right). \quad (6.1)$$

The energy barriers Δ used to fit the data change only little, from 6.8(2) K to 6.70(5) K, due to the partial substitution of Ge by Si. Instead, the shift of the peak positions of χ'' from $\text{Dy}_2\text{Ge}_2\text{O}_7$ to $\text{Dy}_2\text{Ge}_{1.875}\text{Si}_{0.125}\text{O}_7$ mainly result in a change of the pre-exponential factor τ_0 from 250(50) ns to 90(10) ns due to the Si substitution. This pre-exponential factor is attributed to the spin-tunneling rate between the two Ising states and should be determined by the systems CEF level scheme and the transverse fields acting on the flipping spin[60, 115]. The reduction of τ_0 with substitution of Ge by Si is not surprising, as it decreases also with decreasing lattice constant from $\text{Dy}_2\text{Sn}_2\text{O}_7$ to $\text{Dy}_2\text{Ti}_2\text{O}_7$ [116].

Due to the similar shape of the samples, demagnetization effects are unlikely to alter the qualitative observation of a reduction of the pre-exponential factor from $\text{Dy}_2\text{Ge}_2\text{O}_7$ to $\text{Dy}_2\text{Ge}_{1.875}\text{Si}_{0.125}\text{O}_7$.

Apart from the influence of the mere lattice contraction, however, the random distribution of Si and Ge on the B site may contribute to this reduction. Possibly, the lowering of the local site symmetry influences the Ising character of the single ion inducing transverse exchange coupling[50] as perturbation of the dominant Ising interaction. Such transverse exchange coupling might reduce τ_0 as proposed in other rare-earth compounds with spin-ice character[117].

Specific heat measurements The magnetic specific heat c_{mag} of $\text{Dy}_2\text{Ge}_2\text{O}_7$ and the Si-substituted sample, $\text{Dy}_2\text{Ge}_{1.875}\text{Si}_{0.125}\text{O}_7$, in external fields up to 4 T is shown in fig. 6.6. The unsubstituted sample has a peak in the heat capacity at a temperature of 0.84(1) K, determined by a phenomenological fit, whereas the substituted compound has a slightly reduced peak position of 0.80(1) K and an increased peak height. Since this work deals with polycrystalline samples, as does Ref. [30], the peak height can be influenced by factors both in production and measurement. However, a rise of the peak height in the substituted sample fits into the picture of a smaller $J_{\text{nn}}/D_{\text{nn}}$ [54].

This Schottky-like peak is associated to spin-freezing and establishment of the spin-ice state[57]. Even though the peak temperature is shifted only by a small amount, it is a strong hint that the substitution of Si leads to a shift towards the boundary between spin-ice and AFM phase in the phase diagram (fig. 6.1). At temperatures above the peak position, both compounds show almost the same specific heat; above 10 K the phononic contribution becomes dominant. Measurements up to 30 K are used to determine this contribution in order to extrapolate it to the low-temperature specific heat. The magnetic specific heat is the total specific heat minus the phononic contribution. The feature in the specific heat of $\text{Dy}_2\text{Ge}_{1.875}\text{Si}_{0.125}\text{O}_7$ at about 3 K could indicate the possible presence of a minority phase that was not visible in the XRD studies. Furthermore, a broadening of the specific-heat peak of the substituted material towards lower temperatures compared to $\text{Dy}_2\text{Ge}_2\text{O}_7$ can be seen. However, in an ideal spin-ice with smaller $J_{\text{nn}}/D_{\text{nn}}$ than $\text{Dy}_2\text{Ge}_2\text{O}_7$ we would rather expect a narrowing of the specific-heat peak[54]. The origin for this broadening could be related to the random occupation of the Si and Ge atoms on the B site altering the bond environments. A distribution of bond environments might result in a distribution of exchange constants broadening the Schottky-like specific-heat peak.

In magnetic fields, the peak in the specific heat is broadened and shifted to higher temperatures compared to zero field which is an expected behavior for this anomaly [57,

Table 6.1.: Lattice parameters and selected magnetic parameters to insert $\text{Dy}_2\text{Ge}_2\text{O}_7$ and $\text{Dy}_2\text{Ge}_{1.875}\text{Si}_{0.125}\text{O}_7$ in the phase diagram (fig. 6.1).

x	a (Å)	D_{nn} (K)	$c_{\text{mag}}(T_{\text{peak}})$ ($\text{J mol}_{\text{Dy}}^{-1} \text{K}^{-1}$)	T_{peak} (K)	$J_{\text{nn}}/D_{\text{nn}}$	J_{eff} (K)
0	9.930	2.40	3.02	0.84	-0.71	0.69
0.125	9.906	2.42	3.07	0.80	-0.74	0.63

118, 119]. The additional features that arise in field are also observed in Ref. [57] and may be attributed to the polycrystalline nature of the samples[119]. Additional explanations are given in Ref. [120] by simulation methods. A definite conclusion could only be drawn with data obtained from single crystals.

The magnetic entropy was calculated from c_{mag}/T by integrating downwards from the temperature at which the curves with and without field overlap and fixing the plateaus at this value. The entropy data of $\text{Dy}_2\text{Ge}_2\text{O}_7$ and $\text{Dy}_2\text{Ge}_{1.875}\text{Si}_{0.125}\text{O}_7$ at zero field, 1, 2 and 4 T are compared in fig. 6.7. The magnetic entropy of $\text{Dy}_2\text{Ge}_2\text{O}_7$ and $\text{Dy}_2\text{Ge}_{1.875}\text{Si}_{0.125}\text{O}_7$ shows a similar functional behavior. In external magnetic fields of 1 T and higher, the entropy of the ground state is recovered (fig. 6.7). This behavior in an external field is typical for a spin-ice [52, 57, 119] since the external magnetic field lifts the degeneracy of the ground state. The value of the ground-state entropy with $1.62 \text{ J mol}_{\text{Dy}}^{-1} \text{K}^{-1}$ (unsubstituted) and $1.31 \text{ J mol}_{\text{Dy}}^{-1} \text{K}^{-1}$ falls somewhat short of the Pauling entropy of $1.69 \text{ J mol}_{\text{Dy}}^{-1} \text{K}^{-1}$ of the ideal spin ice on a perfect crystal. The same arguments as for the peak height and width apply for this reduction, as well.

To place the new material in the phase diagram, we determined c_{mag} and T_{peak} from fig. 6.6 and calculated the other values in table 6.1 as explained in the following. We determined the dipolar interaction constant by the common estimation:

$$D_{\text{nn}} = \frac{5}{3} \frac{\mu_0 g^2 \mu^2}{4\pi r_{\text{nn}}^3}, \quad (6.2)$$

with the moment assumed from the theoretical value of $g\mu = 10 \mu_{\text{B}}$ and $r_{\text{nn}} = \sqrt{2}a/4$ (a lattice constant) being the distance between two Dy^{3+} ions. Here, we used the lattice constants determined at 300 K from the x-ray diffractograms to be consistent with other publications[30, 121]. Measurements of the thermal expansion of singlecrystalline samples of the isostructural compounds $\text{Dy}_2\text{Ti}_2\text{O}_7$ and $\text{Ho}_2\text{Ti}_2\text{O}_7$ down to low temperatures of about 1 K confirm that the assumed relations are largely retained, . The reduction of the lattice constant of the Si-substituted sample, thus, leads to a slight increase of D_{nn} from 2.40 to 2.42 K. However, the increase of the strength of the exchange interaction,

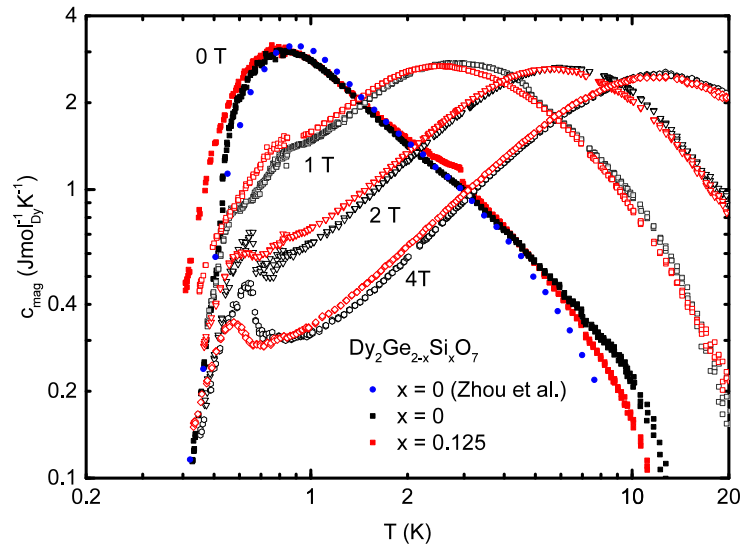


Figure 6.6.: Temperature dependence of the magnetic specific heat c_{mag} per mole Dy of the $\text{Dy}_2\text{Ge}_2\text{O}_7$ and $\text{Dy}_2\text{Ge}_{1.875}\text{Si}_{0.125}\text{O}_7$ samples in black and red symbols, respectively. The zero-field data is marked by full symbols and the data at 1, 2 and 4 T by empty symbols. Specific heat data for $\text{Dy}_2\text{Ge}_2\text{O}_7$ from Zhou *et al.* [30] (blue) have been included for comparison.

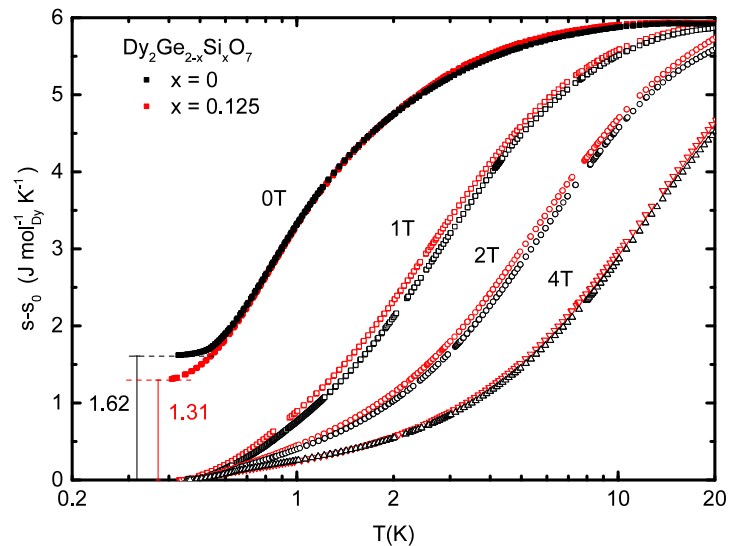


Figure 6.7.: Temperature dependence of the molar entropy of $\text{Dy}_2\text{Ge}_2\text{O}_7$ (black) and $\text{Dy}_2\text{Ge}_{1.875}\text{Si}_{0.125}\text{O}_7$ (red) at zero field (filled) and 1, 2 and 4 T (empty).

J_{nn} , is more pronounced. Following the approach firstly described by den Hertog and Gingras [54] for $\text{Dy}_2\text{Ti}_2\text{O}_7$ and $\text{Ho}_2\text{Ti}_2\text{O}_7$ and used in several publications[30, 52] for Dy and Ho pyrochlores including $\text{Dy}_2\text{Ge}_2\text{O}_7$ and $\text{Ho}_2\text{Ge}_2\text{O}_7$, J_{nn} can be graphically determined on the $T_{\text{peak}}/D_{\text{nn}}-J_{\text{nn}}/D_{\text{nn}}$ line in the phase diagram (fig. 6.1) as the intersection of the phase boundary between spin-ice and paramagnetic phase and the horizontal line with a specific ratio $T_{\text{peak}}/D_{\text{nn}}$. An increase of J_{nn} by 5% from $-1.70(5)$ K to $-1.79(5)$ K can be found. Therefore, the strength of the effective interaction $J_{\text{eff}} = D_{\text{nn}} + J_{\text{nn}}$ is reduced from $0.69(3)$ K to $0.63(3)$ K by about 10%. The reduction of the effective interaction is consistent with the reduced energy scale of the monopole excitation as seen in the ac susceptibility data (fig. 6.5). We find that the activation energy $\Delta \approx -9J_{\text{eff}}$ agrees well with previous measurements on $\text{Dy}_2\text{Ti}_2\text{O}_7$ with $\Delta_{\text{Dy}_2\text{Ti}_2\text{O}_7} \approx -8.9J_{\text{eff}}$ [96, 97].

The value of J_{nn} can also be obtained from comparison of the value of specific-heat peak c_{peak} at the peak temperature with theoretical calculations[54]. The experimental value of c_{peak} is around 10% lower than would be expected from theory for an ideal spin-ice with $J_{\text{nn}}/D_{\text{nn}} = -0.71$ or -0.74 obtained above, which might be due to crystal imperfections. However, it is consistent with the value of previous measurements of the peak height of $\text{Dy}_2\text{Ge}_2\text{O}_7$ [30].

After careful consideration of Ref. [30], we come to the conclusion that the positioning of $\text{Dy}_2\text{Ge}_2\text{O}_7$ in the phase diagram (table 6.1) of that work is at the lower end of the possible region. While obtaining a similar value of T_{peak} they use a slightly higher value of D_{nn} . The fact that our $\text{Dy}_2\text{Ge}_{1.875}\text{Si}_{0.125}\text{O}_7$ sample has a lower $J_{\text{nn}}/D_{\text{nn}}$ than our $\text{Dy}_2\text{Ge}_2\text{O}_7$ as well as the sample investigated in Ref. [30] proves that the reduction of the effective interaction in this compound is significant.

6.4. Discussion

From these data, three conclusions are drawn.

Spin-ice characteristics of $\text{Dy}_2\text{Ge}_{2-x}\text{Si}_x\text{O}_7$: The XRD data show the high quality of the materials and confirm the pyrochlore structure with the Dy^{3+} ions at the A site and randomly distributed Ge and Si at the B site. The magnetization data are close to the expected curve of the powder-averaged paramagnetic Ising spins providing evidence for the Ising nature of the moments of the Dy^{3+} ions due to the strong crystal electric field also observed in other spin-ice pyrochlores[40]. The shape of the temperature-dependent ac susceptibility of Si-substituted Dy germanate resembles the ac susceptibility of the base compound and the well-studied spin-ice materials $\text{Dy}_2\text{Ti}_2\text{O}_7$ [94] and $\text{Dy}_2\text{Sn}_2\text{O}_7$ [122].

However, a substantial difference in the frequency dependence could be identified, which originates in a reduction of τ_0 . The specific heats of $\text{Dy}_2\text{Ge}_2\text{O}_7$ and $\text{Dy}_2\text{Ge}_{1.875}\text{Si}_{0.125}\text{O}_7$ have a similar shape at low temperatures also in accordance with previous measurements of the specific heat of the classical spin ices $\text{Dy}_2\text{Ti}_2\text{O}_7$ [123] and $\text{Ho}_2\text{Ti}_2\text{O}_7$ [70]. Another evidence for $\text{Dy}_2\text{Ge}_{1.875}\text{Si}_{0.125}\text{O}_7$ having spin-ice character is the residual entropy we observed. However, the residual entropy of $\text{Dy}_2\text{Ge}_{1.875}\text{Si}_{0.125}\text{O}_7$ is reduced compared to the Pauling entropy of the ideal spin-ice, possibly a side effect of the random distribution of Si and Ge on the B site of the pyrochlore lattice. In conclusion, the $\text{Dy}_2\text{Ge}_2\text{O}_7$ and $\text{Dy}_2\text{Ge}_{1.875}\text{Si}_{0.125}\text{O}_7$ samples, representing $\text{Dy}_2\text{Ge}_{2-x}\text{Si}_x\text{O}_7$, share several characteristic properties that are common among spin-ice materials.

Reduction of the effective nearest-neighbor interaction by 10 %: Zhou *et al.* [30] have found that substituting ions with smaller ionic radius on the B site of the Dy-pyrochlores $\text{Dy}_2\text{Sn}_2\text{O}_7$ and $\text{Dy}_2\text{Ti}_2\text{O}_7$ reduces the peak temperature of the magnetic specific heat. The authors linked this to a reduction of the effective interaction due to the reduction of the distance between neighboring Dy^{3+} ions using the $T_{\text{peak}}/D_{\text{nn}}-J_{\text{nn}}/D_{\text{nn}}$ phase diagram of the dipolar-spin-ice model[54]. Our XRD measurements confirm the reduced lattice constants in $\text{Dy}_2\text{Ge}_2\text{O}_7$ compared to $\text{Dy}_2\text{Ti}_2\text{O}_7$ [30]. The Si-substituted samples continue this trend towards a reduction of the lattice constants and the peak temperatures in the specific heat as well as in the ac susceptibility. Therefore, we argue, that in $\text{Dy}_2\text{Ge}_{2-x}\text{Si}_x\text{O}_7$ the competing dipolar and exchange interactions are even further increased compared to $\text{Dy}_2\text{Ge}_2\text{O}_7$. Since the increase of the exchange interaction is stronger than the increase of the dipolar interaction, the total effective interaction is reduced compared to $\text{Dy}_2\text{Ge}_2\text{O}_7$.

Influence of disorder on the spin-ice character A thorough study of the effects of disorder on the B site of the spin-ice pyrochlores is not possible with the samples in this paper. But still, the currently highly discussed influence of a stoichiometric or crystallographic disorder can be considered. It is known[124–126] that strong modification of the regular structure can lead to the elimination of frustration, the formation of magnetically ordered clusters or the loss of the Ising character in pyrochlore compounds. Quantum fluctuations can then have an increased effect and weaken the spin-ice character. Although the distribution in the Ge/Si system is random (could be checked by synchrotrons), the low Si content does not seem to be sufficient to eliminate the magnetic frustration in the Dy sublattice. Averaging over microscopically different areas mostly recovers the spin-ice properties of the system.

Part III.

Summary and Outlook

The concept of magnetic frustration is fundamental in modern solid-state physics having direct consequences in magnetically frustrated systems with rich magnetic phases hosting emergent excitations, such as the magnetic monopoles in the spin-ice systems. One important ingredient of frustration is the lattice that constrains the magnetic spins on it to a site anisotropy and inter-site coupling. Therefore, strong interactions between the magnetic system and the lattice are to be expected and investigating these interactions promises deeper insight into the mechanisms governing the physics of frustrated materials.

In this thesis, I have explained the causes of the strong frustration in some pyrochlore compounds with general formula $A_2B_2O_7$, and in particular the much investigated rare-earth titanate pyrochlores $R_2Ti_2O_7$. It is the interplay of strong axial anisotropy of the ground state of the rare-earth ions, in particular for $A = Dy$ and Ho , that is subjected to the strong crystal-electric field on the A site of the compound and the geometric constraints of the pyrochlore lattice of corner-sharing tetrahedra. Two of the most prominent examples of frustrated magnets in this class of materials are the spin-ice pyrochlores $Dy_2Ti_2O_7$ and $Ho_2Ti_2O_7$. These two compounds do not order down to lowest temperatures and are, thus, strongly frustrated. They host a highly degenerate magnetic ground state reminiscent of the structure of water ice, called spin ice, and the excitations on top of this ground state can be interpreted as magnetic monopoles. The term magnetic monopole is justified because between two such monopoles there is a Coulombic interaction repelling monopoles with the same charge and attracts monopoles with opposite charges.

My main contribution to the current research of the geometrically frustrated magnets is the study of the spin-lattice interaction in the classical spin-ice materials $Dy_2Ti_2O_7$ and $Ho_2Ti_2O_7$. In the case of the $Dy_2Ti_2O_7$ and $Ho_2Ti_2O_7$, I have investigated the dependence of the lattice on the magnetic order varied by means of an external magnetic field by dilatometric measurements with single crystals of the two compounds. Moreover, with fast-field-sweep procedures the out-of-equilibrium dynamics of the spin-ice, kagome-ice and saturated-ice phase were probed.

In the dilatometric study of the classical spin-ice compounds I have obtained the following new insights. In terms of the magnetostriction and thermal expansion $Dy_2Ti_2O_7$ and $Ho_2Ti_2O_7$ show qualitatively similar behavior, that seems to be independent of the Kramer or non-Kramers character of $Dy_2Ti_2O_7$ and $Ho_2Ti_2O_7$, respectively. The magnitude of the magnetostrictive effect deep in the spin-ice phase at 0.3 K is $\Delta L/L = 2 \times 10^{-5}$ and 2×10^{-4} for $Dy_2Ti_2O_7$ and $Ho_2Ti_2O_7$, respectively. Ignoring possible background signals, the shape of the magnetostriction curves are very similar, showing a peak-valley feature where the transition from the kagome-ice to the saturated-ice phase is expected. A hysteresis below the transition at lowest temperatures hints at a first order phase transition consistent

with previous experimental and theoretical findings. In numerical simulations using the McPhase software package, the experimental results could be qualitatively reproduced for $\text{Ho}_2\text{Ti}_2\text{O}_7$ and $\text{Dy}_2\text{Ti}_2\text{O}_7$. It turned out, that a magnetostrictive effect based solely on exchange striction cannot reproduce the experimental observation, instead, a combination of exchange striction and crystal-field striction is needed.

A second highlight of the dilatometric measurements of the spin-ice compounds is the observation of slow relaxation processes. For this the saturated-ice phase was stabilized in a high field at low temperatures, then the field was quickly swept down into the frustrated kagome-ice and spin-ice phases and the relative expansion of the crystal was monitored. At first, the lattice expanded or contracted quickly on the time scale of the field sweep rate but after the field was stabilized the lattice continued to expand or contract relaxing slowly to a metastable state with a stretched exponential law for both $\text{Dy}_2\text{Ti}_2\text{O}_7$ and $\text{Ho}_2\text{Ti}_2\text{O}_7$. The longest relaxation times were observed at lowest temperatures and in the field range where a hysteresis in the magnetostriction measurements was observed, i.e., below 0.8 T for $\text{Dy}_2\text{Ti}_2\text{O}_7$ and below 1.0 T for $\text{Ho}_2\text{Ti}_2\text{O}_7$. From the known phase diagrams I find that the region of longest relaxation coincides well with the kagome-ice phase. In that phase the relaxation time is of the order of hours. With increasing temperatures the time scale of the relaxation reduces to minutes at around 0.7 K corresponding to the spin-freezing temperature obtained from ac-susceptibility measurements.

In the second study I investigated the magnetoelastic coupling by varying the lattice constant and checking how the magnetic properties were changing. High-quality polycrystals of the pyrochlores $\text{Dy}_2\text{Ge}_{2-x}\text{Si}_x\text{O}_7$ with lattice constants down to 9.906 Å using the multi-anvil technique with pressures up to 16 GPa have been synthesized. The Ising nature of the moments of the Dy ions was confirmed by the field dependence of the static magnetization. Specific heat and ac susceptibility show the typical behavior of classical spin-ice compounds, namely a Schottky-like anomaly and residual entropy, and a frequency-dependent maximum, respectively. The reduction of the lattice reduces the effective interaction by about 10%. The most significant difference between the substituted and unsubstituted compounds was found in the frequency dependence of the ac-susceptibility signal, which mainly originates in a reduction of the pre-exponential factor τ_0 . However, a reduction of the energy scale of monopole excitations of 1.5% was observed as well, which underlines the finding of a reduced effective interaction. In conclusion, we showed, that silicon substitution is a possible way to change the ratio of dipolar and exchange interaction and, hence, synthesize spin-ice compounds with customized properties.

Giving a brief outlook on possible future research, I propose three ideas. One possibility to build on the measurements in this work would be to perform pulsed-field magne-

tostriction measurements of $\text{Dy}_2\text{Ti}_2\text{O}_7$ and $\text{Ho}_2\text{Ti}_2\text{O}_7$ with the fiber-Bragg-grating (FBG) technique. This technique is less sensitive than the capacitance dilatometry, but in this thesis I showed that the magnetostrictive effects are large enough to be detected with the FBG technique, especially at high-magnetic fields. In these measurements, the crystal-field striction could be investigated up to much higher fields and a further comparison to the McPhase model calculation would be possible.

Further, the magnetoelastic properties of other compounds of the class of rare-earth pyrochlores should be investigated by dilatometry. For example, in $\text{Nd}_2\text{Hf}_2\text{O}_7$ interesting non-equilibrium effects were observed associated to domain boundary dynamics; specifically, the feature observed in this compound is negative remanence magnetization. The magnetoelastic properties of these domain boundaries could probably be detected and their dynamics could be studied. In the pyrochlores with Gd on the A site, systems without orbital momentum could be studied. In these systems the total angular momentum consists purely of the spin momentum and is isotropic. This would broaden the perspective to more than the easy-axis systems studied in this thesis. Finally, much is done in the field of quantum spin ices [11, 107] such as $\text{Pr}_2\text{Hf}_2\text{O}_7$ and dilatometric measurements would help in characterizing the magnetoelastic properties of these new compounds.

Going away from the rare-earth pyrochlores, also other materials with a sublattice of corner-sharing tetrahedra, the spinels, were found. These compounds have the general chemical formula AB_2O_4 , where A and B are transition-metal ions. These compounds show rich phase diagrams [4] and investigation of these compounds would broaden the perspective from the focus on rare-earth ions to magnetic transition-metal ions.

Part IV.
Appendix

Appendix A.

Derivation of the formulas for the simulation of the magnetostriction

In this part of the appendix, the derivations of equations necessary for the formula of the equilibrium strain is collected.

A.1. The mean-field Hamiltonian

Given a Hamiltonian H_{TOT} that is a sum of a local Hamiltonian H_{SI}^i of a single ion at lattice site i and a second non-local Hamiltonian H_{EX}^i coupling the ion at lattice site i with the other ions at lattice site j . In section 2.1, the goal is to diagonalize such a Hamiltonian eq. (2.5):

$$H_{TOT} = \sum_i (H_{SI}^i + H_{EX}^i)$$

This problem is solved in [17] and specified to the case with H_{SI}^i and H_{EX}^i given in eqs. (2.1) and (2.4), respectively. The Hamiltonian H_{TOT} reads explicitly:

$$H_{TOT} = \sum_{i=1}^N H_{SI}^i - \frac{1}{2} \sum_{i=1}^N \sum_{j \in \text{NN}(i)} J_{ij} (|\vec{R}_j - \vec{R}_i|) \vec{J}_i \vec{J}_j,$$

where \vec{R}_i is the position of the lattice site i and the exchange constant depends on the distance vector between the two lattice sites i and j . This equation can be rewritten in

terms of an effective magnetic field \vec{H}_i at lattice site i , called the mean field composed by the fields from all spins at other lattice sites j :

$$H_{TOT} = \sum_{i=1}^N \left(H_{SI}^i - \vec{H}_i \vec{J}_i \right),$$

$$\text{with } \vec{H}_i = \frac{1}{2} \sum_{j \in \text{NN}(i)}^N J_{ij} (|\vec{R}_j - \vec{R}_i|) \langle \vec{J}_j \rangle,$$

where $\langle \vec{J}_j \rangle$ is the thermal expectation value of \vec{J}_j . Let ion i be situated at position s in unit cell k . The sum over i in the above equations splits into a sum over all positions s per unit cell and all unit cells k . Based on the observation, that the single-ion Hamiltonian H_{SI}^i has the same symmetry as the lattice, I suppose the mean field \vec{H}_i to have the same periodicity as the lattice, as well. In that case, the derivation can be confined further on a single unit cell and the mean field Hamiltonian H^{MF} :

$$H^{\text{MF}} = \sum_{s=1}^S \left(H_{SI}^s - \vec{H}_s \vec{J}_s \right), \quad (\text{A.1})$$

$$\text{with } \vec{H}_s = \frac{1}{2} \sum_{j \in \text{NN}(s)}^N J_{sj} (|\vec{R}_j - \vec{R}_s|) \langle \vec{J}_j \rangle, \quad (\text{A.2})$$

which is the mean-field Hamiltonian with the mean field \vec{H}_s given in section 2.1 with $J_{sj} (|\vec{R}_j - \vec{R}_s|) = J$ the same for all s and j . This Hamiltonian is solved in section 4.4 using the McPhase software bundle.

A.2. The general linear anisotropic stress-strain relation

Here, I introduce the linear stress-strain relation in its most general form:

$$\sigma = C \epsilon,$$

where C is a fourth-rank $3 \times 3 \times 3 \times 3$ tensor with 81 components linking the two second-order 3×3 tensors of the stress σ and the strain ϵ with each other.

Due to the symmetries of the strain and stress tensors, the components of the stiffness tensor in Cartesian coordinates are not independent from each other and the number of maximally 81 independent components is reduced to 21. In order to shorten the notation

of this equation in the component form in Cartesian coordinates, the tensors ϵ , σ and C are written as 6-component vectors and 6×6 matrix, respectively:

$$\begin{pmatrix} \sigma_{11} \\ \sigma_{22} \\ \sigma_{33} \\ \sigma_{23} \\ \sigma_{13} \\ \sigma_{12} \end{pmatrix} = \begin{pmatrix} C_{1111} & C_{1122} & C_{1133} & C_{1123} & C_{1113} & C_{1112} \\ & C_{2222} & C_{2233} & C_{2223} & C_{2213} & C_{2212} \\ & & C_{3333} & C_{3323} & C_{3313} & C_{3312} \\ & & & C_{2323} & C_{2313} & C_{2312} \\ & & & & C_{1313} & C_{1312} \\ & & & & & C_{1212} \end{pmatrix} \begin{pmatrix} \epsilon_{11} \\ \epsilon_{22} \\ \epsilon_{33} \\ 2\epsilon_{23} \\ 2\epsilon_{13} \\ 2\epsilon_{12} \end{pmatrix} \quad (\text{A.3})$$

with indices 1 to 3 corresponding to the Cartesian axes x , y and z , respectively.

In the shorter engineering or Voigt notation this is written as:

$$\begin{pmatrix} \sigma_1 \\ \sigma_2 \\ \sigma_3 \\ \sigma_4 \\ \sigma_5 \\ \sigma_6 \end{pmatrix} = \begin{pmatrix} C_{11} & C_{12} & C_{13} & C_{14} & C_{15} & C_{16} \\ & C_{22} & C_{23} & C_{24} & C_{25} & C_{26} \\ & & C_{33} & C_{34} & C_{35} & C_{36} \\ & & & C_{44} & C_{45} & C_{46} \\ & & & & C_{55} & C_{56} \\ & & & & & C_{66} \end{pmatrix} \begin{pmatrix} \epsilon_1 \\ \epsilon_2 \\ \epsilon_3 \\ \epsilon_4 \\ \epsilon_5 \\ \epsilon_6 \end{pmatrix} \quad (\text{A.4})$$

In the case of the cubic symmetry of the pyrochlore lattice, only 3 out of the 21 independent components remain independent: $C_{11} = C_{22} = C_{33}$, $C_{12} = C_{13} = C_{23}$ and $C_{44} = C_{55} = C_{66}$, while all other components are zero.

A.3. Perturbation of the magnetoelastic Hamiltonian for small arbitrary and trigonal strains

In section 2.2, the first-order approximation of the equilibrium strain (eq. (2.13)) of the magnetoelastic Hamiltonian (eq. (2.11)). In this section, I present the derivation of this expression in detail.

It will be advantageous to readjust the focus from the single-ion perspective to perspective of the unit cell of the crystal containing several single ions. In order to obtain the total Hamiltonian of the crystal we can either sum over all N ions or equivalently over all K unit cells containing S single ions. The index i of each ion can be represented by the two indices k and s representing particular unit cells and ions in a unit cell, respectively. The

formula is given by $i(k, s) = kS + s$. Given the elastic energy per unit cell and the number S of lattice sites in a unit cell with index k , the complete Hamiltonian can be written as:

$$H(\epsilon) = \sum_{k=1}^K \left(\sum_{s=1}^S \left(H_0 + H_1 + H_{SO} + H_{CEF}^{i(k,s)}(\epsilon) + H_{Ze} + H_{EX}^{i(k,s)}(\epsilon) \right) + E_{el}(\epsilon) \right).$$

For small strains, the strain-dependent contributions of the crystal-field and the exchange Hamiltonian can be approximated to first order:

$$\begin{aligned} H_{EX}^i(\epsilon) &= -\frac{1}{2} \sum_{j \in \text{NN}(i)} J(\epsilon) \vec{J}_i \vec{J}_j \\ &\approx H_{EX}^i(0) - \frac{1}{2} \sum_{j \in \text{NN}(i)} \sum_{st} \left[\frac{\partial J(\epsilon)}{\partial \epsilon_{st}} \right]_{\epsilon=0} \epsilon_{st} \vec{J}_{i(k,s)} \vec{J}_j, \\ H_{CEF}^i(\epsilon) &= \sum_{l=0}^{\infty} \sum_{m=-l}^l B_l^m(\epsilon) O_l^m \\ &\approx H_{CEF}^i(0) + \sum_{l=0}^{\infty} \sum_{m=-l}^l \sum_{st} \left[\frac{\partial B_l^m(\epsilon)}{\partial \epsilon_{st}} \right]_{\epsilon=0} \epsilon_{st} O_l^m, \\ E_{el} &= \frac{V}{2} \sum_{mnl} C_{mnl} \epsilon_{mn} \epsilon_{kl}. \end{aligned}$$

For small strain tensors ϵ we can approximate the magnetoelastic Hamiltonian by linearizing it around $\epsilon = 0$ in the form $H(\epsilon) = H(\epsilon = 0) + \delta H$. The perturbation Hamiltonian δH is given by:

$$\begin{aligned} \delta H &= \sum_{k=1}^K \left(\sum_{s=1}^S \sum_{st} \left(\sum_{l=0}^{\infty} \sum_{m=-l}^l \left[\frac{\partial B_l^m(\epsilon)}{\partial \epsilon_{st}} \right]_{\epsilon=0} \epsilon_{st} O_l^m - \right. \right. \\ &\quad \left. \left. - \frac{1}{2} \sum_{j=1, j \neq i}^N \left[\frac{\partial J(\epsilon)}{\partial \epsilon_{st}} \right]_{\epsilon=0} \epsilon_{st} \vec{J}_i \vec{J}_j \right) + \frac{V}{2} \sum_{mn} C_{mnst} \epsilon_{mn} \epsilon_{st} \right). \quad (\text{A.5}) \end{aligned}$$

In the trigonal strain mode with $-2\epsilon_{11} = -2\epsilon_{22} = \epsilon_{33} = \epsilon$, we can vastly simplify eq. (A.5) using the expression eq. (A.12) for the elastic energy from section A.7:

$$\begin{aligned} \delta H &= \epsilon \sum_{k=1}^K \left(\sum_{s=1}^S \left(\sum_{l=0}^{\infty} \sum_{m=-l}^l \left[\frac{\partial B_l^m(\epsilon)}{\partial \epsilon} \right]_{\epsilon=0} O_l^m - \right. \right. \\ &\quad \left. \left. - \frac{1}{2} \sum_{j=1, j \neq i}^N \left[\frac{\partial J(\epsilon)}{\partial \epsilon} \right]_{\epsilon=0} \vec{J}_i \vec{J}_j \right) + \frac{3}{4} V (c_{11} - c_{12}) \epsilon \right). \quad (\text{A.6}) \end{aligned}$$

For the equilibrium strain ϵ' , the operator δH acting on the ground state should give zero. It is sufficient to use the ground state ψ of the unperturbed Hamiltonian to calculate this, which is a result of first-order perturbation theory. The ground state is a product of the wavefunctions ψ_i at the lattice site i . So, for the trigonal equilibrium strain we obtain:

$$0 = \langle \psi | \delta H | \psi \rangle = \epsilon' \sum_{k=1}^K \left(\sum_{s=1}^S \left(\sum_{l=0}^{\infty} \sum_{m=-l}^l \left[\frac{\partial B_l^m(\epsilon)}{\partial \epsilon} \right]_{\epsilon=0} \langle \psi | O_l^m | \psi \rangle - \frac{1}{2} \sum_{j=1, j \neq i}^N \left[\frac{\partial J(\epsilon)}{\partial \epsilon} \right]_{\epsilon=0} \langle \psi | \vec{J}_i \vec{J}_j | \psi \rangle \right) + \frac{3}{4} V (c_{11} - c_{12}) \epsilon' \right). \quad (\text{A.7})$$

In a mean-field approach, where every unit cell is equivalent and has the same energy, the sum is zero if and only if the energy of each unit cell vanishes. Hence, the equilibrium strain is given by the requirement that the energy variation of the unit cell vanishes. From that, the equilibrium strain ϵ' can be obtained:

$$\epsilon' = -\frac{4}{3V(c_{11} - c_{12})} \sum_{s=1}^S \left(\sum_{l=0}^{\infty} \sum_{m=-l}^l \left[\frac{\partial B_l^m(\epsilon)}{\partial \epsilon} \right]_{\epsilon=0} \langle \psi | O_l^m | \psi \rangle - \frac{1}{2} \sum_{j=1, j \neq i(k', s)}^N \left[\frac{\partial J(\epsilon)}{\partial \epsilon} \right]_{\epsilon=0} \langle \psi | \vec{J}_{i(k', s)} \vec{J}_j | \psi \rangle \right). \quad (\text{A.8})$$

The magnetic field is included in this expression in form of the ground state ψ of the unperturbed system that contains the Zeeman interaction. Until now, the focus was on the equilibrium strain at zero temperature. In order to obtain the state at finite temperature the free energy needs to be calculated.

A.4. Free energy of the magnetoelastic system and equilibrium strain

Since I am also interested in the influence of the temperature on the striction I calculated the magnetic free energy F_m :

$$F_m = -k_B T \ln Z, \quad Z = \text{Tr}(e^{-H(\epsilon)/k_B T}) = \sum_i \langle \psi_i | e^{-H(\epsilon)/k_B T} | \psi_i \rangle,$$

where Z is the partition sum, k_B the Boltzmann constant, T the temperature, $H(\epsilon)$ the magnetoelastic Hamiltonian and ψ_i the eigenstates of the system at zero strain. The free

energy and the partition sum both can be approximated to first order in the same way as the Hamiltonian as $F_m(\epsilon) \approx F_m(0) + \delta F_m$ and $Z(\epsilon) \approx Z(0) + \delta Z$:

$$\begin{aligned}\delta F_m &= -(k_B T / Z^0) \delta Z \\ \delta Z &= -\frac{1}{k_B T} \langle \delta H \rangle = \sum_i \langle \psi_i | e^{-(H)/k_B T} (\delta H / k_B T) | \psi_i \rangle\end{aligned}$$

where $\langle \cdot \rangle$ denote the thermal average. In equilibrium, the variation of the free energy vanishes $0 = \delta F_m \propto \delta Z$, which is obviously true if $\langle \delta H \rangle = 0$; this yields a formula for the equilibrium strain ϵ' at finite temperatures similar to eq. (A.8):

$$\begin{aligned}\epsilon' &= -\frac{4}{3V(c_{11} - c_{12})} \sum_{s=1}^S \left(\sum_{l=0}^{\infty} \sum_{m=-l}^l \left[\frac{\partial B_l^m(\epsilon)}{\partial \epsilon} \right]_{\epsilon=0} \langle O_l^m \rangle - \right. \\ &\quad \left. - \frac{1}{2} \sum_{j=1, j \neq i}^N \left[\frac{\partial J(\epsilon)}{\partial \epsilon} \right]_{\epsilon=0} \langle \vec{J}_i \vec{J}_j \rangle \right), \quad (\text{A.9})\end{aligned}$$

which is the equation for the magnetoelastic properties at finite temperatures in the tetragonal strain mode.

A.5. Conversion between sets of elastic constants

The elastic constants c_{11} , c_L and c_T have linear relations to c_{11} , c_{12} (all explained in [19]):

$$\begin{pmatrix} c_{11} \\ c_L \\ c_T \end{pmatrix} = \frac{1}{3} \begin{pmatrix} 3 & 0 & 0 \\ 1 & 2 & 4 \\ 1 & -1 & 1 \end{pmatrix} \begin{pmatrix} c_{11} \\ c_{12} \\ c_{44} \end{pmatrix} \Leftrightarrow \begin{pmatrix} c_{11} \\ c_{12} \\ c_{44} \end{pmatrix} = \frac{1}{2} \begin{pmatrix} 2 & 0 & 0 \\ 1 & 1 & -4 \\ -1 & 1 & 2 \end{pmatrix} \begin{pmatrix} c_{11} \\ c_L \\ c_T \end{pmatrix} \quad (\text{A.10})$$

where I inverted the matrix, to obtain the needed relations. Thus, for the tetragonal strain mode I obtain the elastic constant:

$$c_{11} - c_{12} = \frac{1}{2}(c_{11} - c_L + 4c_T), \quad (\text{A.11})$$

which is used as parameter in the simulation of the magnetostriction of $\text{Dy}_2\text{Ti}_2\text{O}_7$ and $\text{Ho}_2\text{Ti}_2\text{O}_7$.

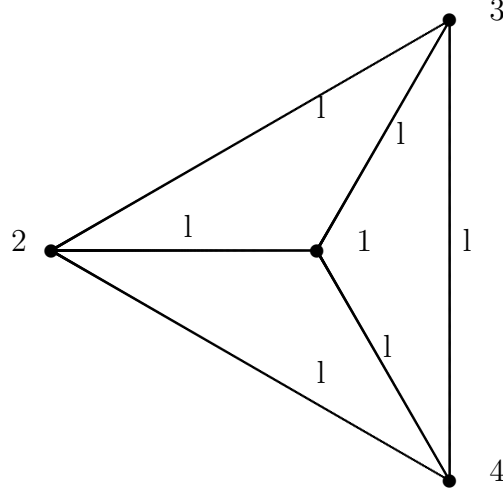


Figure A.1.: Point 1: $(0, 0, h)$, Point 2: $(-b, 0, 0)$, Point 3: $(b \cos 120, -b \sin 120, 0)$, Point 4: $(b \cos 120, b \sin 120, 0)$

A.6. Deformation of a tetrahedron in tetragonal strain

For the calculation of the exchange-striction mechanism, the effect of strain on the exchange interaction is modeled via:

$$\partial_\epsilon J_{ij} = \partial_r J_{ij} \partial_\epsilon r,$$

To calculate $\partial_\epsilon r$, I take a tetrahedron with vertex coordinates as shown in fig. A.1: $(0, 0, h)$, $(-b, 0, 0)$, $(b \cos 120, -b \sin 120, 0)$ and $(b \cos 120, b \sin 120, 0)$. Again, the tetragonal strain is given by $-2\epsilon_{11} = -2\epsilon_{22} = \epsilon_{33} = \epsilon$. The distance between vertices i and j is denoted by r_{ij} where vertex 1 is the top of the tetrahedron and the other three are in its basis:

$$\begin{aligned} r_{23} = r_{42} = r_{34} &= |(b \cos(120) - b \cos(120), -b \sin(120) - b \sin(120), 0)| \\ &= \sqrt{3}b \end{aligned}$$

$$r_{13} = r_{14} = r_{12} = \sqrt{h^2 + b^2} = \sqrt{h^2 + \frac{1}{3}l^2} = l \quad \Rightarrow \quad h = \sqrt{\frac{2}{3}}l$$

Using the notation $l = \sqrt{3}b$, we calculate the distances r'_{ij} between vertices i and j after application of the tetragonal strain in first order of ϵ :

$$\begin{aligned} r'_{23} = r'_{42} = r'_{34} &= |(0, (-b \sin(120) - b \sin(120))(1 + \epsilon_{22}), 0)| = l(1 - \frac{1}{2}\epsilon), \\ r'_{13} = r'_{14} = r'_{12} &= |(b(1 + \epsilon_{11}), 0, h(1 + \epsilon_{33}))| = l(1 + \frac{1}{2}\epsilon). \end{aligned}$$

In the description of the simulation of the static magnetostriction of the spin-ice pyrochlores I use these formulas.

A.7. Elastic energy in cubic symmetry for tetragonal strain

The simplest possible harmonic elastic energy expression is given by:

$$E_{\text{el}} = \frac{V}{2} \sum_{mnlk} c_{mnlk} \epsilon_{mn} \epsilon_{kl}$$

In the rest of this section, I use the index convention from section A.2. In the case of cubic symmetry, the elastic energy above can be written explicitly:

$$\begin{aligned} E_{\text{el}} &= \frac{V}{2} \sum_{mn} c_{mn} \epsilon_m \epsilon_n = \frac{V}{2} \left(\sum_{mm} c_{mm} \epsilon_m \epsilon_m + 2 \cdot \sum_{n>m} c_{mn} \epsilon_m \epsilon_n \right) \\ &= \frac{V}{2} (c_{11}(\epsilon_1^2 + \epsilon_2^2 + \epsilon_3^2) + 2c_{12}(\epsilon_1 \epsilon_2 + \epsilon_1 \epsilon_3 + \epsilon_2 \epsilon_3) + 2c_{44}(\epsilon_4^2 + \epsilon_5^2 + \epsilon_6^2)) , \end{aligned}$$

which can be split into the different strain modes: one hydrostatic, two trigonal and three shear strain modes:

$$\begin{aligned} E_{\text{el}} &= \frac{V}{2} \left(\frac{c_{11} + c_{12}}{3} (\epsilon_1 + \epsilon_2 + \epsilon_3)^2 + \right. \\ &\quad \left. + (c_{11} - c_{12}) \left(\frac{2}{3} (\epsilon_3 - \frac{1}{2}(\epsilon_1 + \epsilon_2))^2 + \frac{1}{2} (\epsilon_1 - \epsilon_2)^2 \right) + 2c_{44}(\epsilon_4^2 + \epsilon_5^2 + \epsilon_6^2) \right) \end{aligned}$$

In the tetragonal strain mode with $-2\epsilon_1 = -2\epsilon_2 = \epsilon_3 = \epsilon$ and $\epsilon_4 = \epsilon_5 = \epsilon_6 = 0$ only the first part of the tetragonal term survives and the elastic energy simplifies to:

$$E_{\text{el}} = \frac{3}{4} V (c_{11} - c_{12}) \epsilon^2 . \tag{A.12}$$

This expression is needed in the calculation of the magnetoelastic Hamiltonian.

A.8. Crystal field in the pyrochlore lattice

The crystal field Hamiltonian reads:

$$H_{CEF}^i = \sum_{l=0}^{\infty} \sum_{m=-l}^l B_l^m(i) O_l^m(i). \quad (\text{A.13})$$

In the symmetry of the pyrochlore lattice, the crystal field has only six independent components: B_2^0 , B_4^0 , B_4^3 , B_6^0 , B_6^3 and B_6^6 [16]. The corresponding Stevens operators O_l^m can be formulated in terms of the angular momentum operator \vec{J} , more specifically in terms of one cartesian component J^z of the vector \vec{J} and the ladder operators J_{\pm} . The wave functions $|j, m\rangle$ are eigenvectors of these operators and their actions on them are:

$$\vec{J}^2 |j, m\rangle = j(j+1) |j, m\rangle \quad (\text{A.14})$$

$$J^z |j, m\rangle = m |j, m\rangle \quad (\text{A.15})$$

$$J_{\pm} |j, m\rangle = |j, m \pm 1\rangle \quad (\text{A.16})$$

The Stevens operators are given by:

$$\begin{aligned} X &= \vec{J}^2 = J(J+1) \\ O_2^0 &= 3J_z^2 + X \\ O_4^0 &= 35J_z^4 - (30X - 25)J_z^2 + 3X^2 - 6X \\ O_6^0 &= 231J_z^6 - (315X - 735)J_z^4 + (105X^2 - 525X + 294)J_z^2 - 5X^3 + 40X^2 - 60X \\ O_4^3 &= \frac{1}{4} \left[(J_+^3 + J_-^3)J_z + J_z(J_+^3 + J_-^3) \right] \\ O_4^{-3} &= \frac{-i}{4} \left[(J_+^3 - J_-^3)J_z + J_z(J_+^3 - J_-^3) \right] \\ O_6^3 &= \frac{1}{4} \left[(J_+^3 + J_-^3)(11J_z^3 - (3X + 59)J_z) + (11J_z^3 - (3X + 59)J_z)(J_+^3 + J_-^3) \right] \\ O_6^{-3} &= \frac{-i}{4} \left[(J_+^3 - J_-^3)(11J_z^3 - (3X + 59)J_z) + (11J_z^3 - (3X + 59)J_z)(J_+^3 - J_-^3) \right] \\ O_6^6 &= \frac{1}{2} (J_+^6 + J_-^6) \\ O_6^{-6} &= \frac{-i}{2} (J_+^6 - J_-^6) \end{aligned}$$

The operators J_{\pm} couple the state m_J with a state with $m_{J\pm 1}$ and J_{\pm}^3 couple the state m_J with a state with $m_{J\pm 3}$.

A.9. Wave functions of the ground state of of the rare-earth ion in $\text{Dy}_2\text{Ti}_2\text{O}_7$ and $\text{Ho}_2\text{Ti}_2\text{O}_7$

In order to obtain the ground state of the mean-field Hamiltonian (eqs. (2.1), (2.6) and (2.7)) I use McPhase with the crystal field parameters from tables 4.1 and 4.2. For $\text{Dy}_2\text{Ti}_2\text{O}_7$, this yields the ground states of the rare-earth ion in the unstrained and strained crystal; for comparison, estimates of the ground state from literature [40, 42] are also given:

$$\begin{aligned}
 |\phi_0^\pm \rangle (\epsilon = 0) &= 0.9998|\pm \frac{15}{2} \rangle \pm 0.0201|\pm \frac{9}{2} \rangle \\
 |\phi_0^\pm \rangle (\epsilon = 0.02) &= 0.9998|\pm \frac{15}{2} \rangle \pm 0.0190|\pm \frac{9}{2} \rangle \\
 |\phi_0^\pm \rangle &= 0.981|\pm \frac{15}{2} \rangle \pm 0.190|\pm \frac{9}{2} \rangle - 0.022|\pm \frac{3}{2} \rangle \mp 0.037|\mp \frac{3}{2} \rangle \\
 &\quad + 0.005|\mp \frac{9}{2} \rangle \mp 0.001|\mp \frac{15}{2} \rangle \\
 |\phi_0^\pm \rangle &= 0.991|\pm \frac{15}{2} \rangle \mp 0.127|\pm \frac{9}{2} \rangle + 0.019|\pm \frac{3}{2} \rangle \\
 &\quad \mp 0.025|\mp \frac{3}{2} \rangle + 0.005|\mp \frac{9}{2} \rangle
 \end{aligned}$$

and for $\text{Ho}_2\text{Ti}_2\text{O}_7$ we get the corresponding ground states:

$$\begin{aligned}
 |\phi_0^\pm \rangle (\epsilon = 0) &= 0.9941|\pm 8 \rangle \pm 0.1081|\pm 5 \rangle + 0.0070|\pm 2 \rangle \\
 |\phi_0^\pm \rangle (\epsilon = 0.02) &= 0.9941|\pm 8 \rangle \pm 0.1079|\pm 5 \rangle + 0.0067|\pm 2 \rangle \\
 |\phi_0^\pm \rangle &= -0.979|\pm 8 \rangle \pm 0.189|\pm 5 \rangle - 0.014|\pm 2 \rangle \pm 0.070|\mp 1 \rangle \\
 &\quad - 0.031|\mp 4 \rangle \pm 0.005|\mp 7 \rangle \\
 |\phi_0^\pm \rangle &= 0.981|\pm 8 \rangle \mp 0.154|\pm 5 \rangle + 0.075|\pm 2 \rangle \mp 0.073|\mp 1 \rangle \\
 &\quad + 0.054|\mp 4 \rangle \mp 0.007|\mp 7 \rangle
 \end{aligned}$$

Appendix B.

Derivation of the formulas for the analysis of the magnetostriction and relative expansion data

In this part of the appendix, I collected the derivations of the equations used for the analysis of the magnetostriction and thermal-expansion data. Even though these equations can straightforwardly derived, not all steps are obvious and, hence, I decided to give the necessary information explicitly for the interested reader. Both dilatometer-cell designs, TDC and TAC, I used in this work are tilted-plate capacitors. The general formula for the dependence between capacity and gap width is derived for this case and then specified for the two designs.

B.1. The general tilted-plate capacitor

The formula used to calculate the change of the sample length was derived by Pott and Schefzyk [20] by solving the integral over a disk Ω with radius R :

$$C = \int_{\Omega} \frac{\epsilon_0}{d + cx} dx dy,$$

where c is the inclination of the upper plate with respect to the lower plate, ϵ_0 denotes the vacuum permittivity and d is the gap at the coordinate $x = 0$ in the center of the plate.

We transform the coordinate system (x, y) to (x', y') such that $cx' = d + cx$. The integral can then be solved using the tabulated integrals 248, 226 and 246 from Zwillinger [127]:

$$C = \frac{2\pi\epsilon_0 d}{c^2} \left(1 - \sqrt{1 - \frac{R^2 c^2}{d^2}} \right). \quad (\text{B.1})$$

This formula is fundamental to the derivation of the relative-expansion dependences used for the analysis of the magnetostriction and thermal-expansion measurements using the TDC and the TAC. These equations are given in section 3.1 and the equation for the TDC is derived in detail in the next paragraphs.

Equation (B.1) may be rewritten to be more easily usable for data analysis. For this, the following rearrangements of eq. (B.1) are used:

$$C = \frac{2\pi R\epsilon_0}{c\gamma} \left(1 - \sqrt{1 - \gamma^2} \right) \quad \text{with} \quad \gamma = \frac{Rc}{d} \quad (\text{B.2})$$

and equivalently:

$$\frac{Cc}{2\pi R\epsilon_0} = \frac{(1 - \sqrt{1 - \gamma})}{\gamma} \quad (\text{B.3})$$

The parameter c is the tilting of the upper capacitance plate with respect to the lower plate. In the case of the TDC, when the upper plate is pushed down by the expanding sample, it does not change its tilting due to the parallel suspension [128, 129] it is linked to. The plate can only move vertically and does not rotate [20, 23].

The parameter c is difficult to measure directly. It is easier to substitute it by the value of the capacitance C_{max} for almost touching capacitor plates for $\gamma = 1$ and rearrange eq. (B.2) in terms of this new parameter C_{max} . This value C_{max} is obtained for $c = \frac{d}{R}$:

$$C_{max} = \frac{2\pi\epsilon_0 R}{c} \quad (\text{B.4})$$

Evaluating $1 + (C/C_{max})^2$ using eqs. (B.3) and (B.4) and that c is constant for all d one obtains the gap distance d :

$$d = \frac{\epsilon_0\pi R^2}{C} \left[1 + \left(\frac{C}{C_{max}} \right)^2 \right] \quad (\text{B.5})$$

This is only valid, if the tilting of the upper plate with respect to the lower plate is constant for all d , which is not true for TAC. I also inverted eq. (B.2) for d using Mathematica giving :

$$d = \frac{\epsilon_0 \pi R^2}{C} + \frac{c^2}{4\pi\epsilon_0} C \quad (\text{B.6})$$

This equation is equivalent to eq. (B.5). There is a C^{-1} increase dominant when approaching 0, and asymptotically linear behavior at high C .

Ultimately, I am interested in the difference of two such gaps Δd normalized by the sample length L_S :

$$\frac{\Delta d}{L_S} = \frac{d_2 - d_1}{L_S} = \frac{\epsilon_0 \pi r^2}{L_S} \left(\frac{1}{C_2} \left[1 + \left(\frac{C_2}{C_{max}} \right)^2 \right] - \frac{1}{C_1} \left[1 + \left(\frac{C_1}{C_{max}} \right)^2 \right] \right) \quad (\text{B.7})$$

$$= \frac{\epsilon_0 \pi r^2}{L_S C_1 C_2} (C_1 - C_2) \left[1 - \frac{C_1 C_2}{C_{max}^2} \right]. \quad (\text{B.8})$$

Appendix C.

Effective spin-ice model

In this chapter, I use a simplified model of the magnetism of the spin-ice pyrochlores to calculate several physical properties. The most important result is that in the case of a magnetic field slightly misaligned with respect to the $[1\ 1\ 1]$ direction of the crystal strong magnetic torque is exerted on the sample. This might influence the measurement, but by performing several test measurements this effect could be excluded to play a role for the magnetostriction of $\text{Dy}_2\text{Ti}_2\text{O}_7$ and $\text{Ho}_2\text{Ti}_2\text{O}_7$ in this work, see subsection 3.3.2.

The complete Hamiltonian eq. (2.1) of the spin-ice pyrochlores can be split for low temperatures and low fields into a single-ion part H_{GS} fixing the ground state and the Zeeman H_{Ze} and exchange Hamiltonian H_{ex} that work on that ground state as perturbations:

$$H = H_0 + H_1 + H_{SO} + H_{CEF} + H_{Ze} + H_{ex} = H_{GS} + H_{Ze} + H_{ex}. \quad (\text{C.1})$$

For the spin ice compounds, $\text{Dy}_2\text{Ti}_2\text{O}_7$ and $\text{Ho}_2\text{Ti}_2\text{O}_7$ the single ion has a quasi-Ising ground state. In the following, it is assumed that all single-ions are in the ground state of the Hamiltonian H_{GS} so that the perturbation Hamiltonian may be projected into this subspace.

C.1. Low-temperature simple effective model of spin ice

In this section the effective model of spin ice is presented and used in the following sections to calculate torque effects on samples in a magnetic field slightly misaligned from the $[1\ 1\ 1]$ direction.

I use the effective Hamiltonian \mathcal{H} of one tetrahedron to describe the low-temperature magnetic properties of spin ice:

$$\mathcal{H} = \sum_{j>i=1}^4 \mathcal{J}(\vec{v}_i \cdot \vec{v}_j)(J_i J_j) - 10\mu_B \vec{B} \sum_{i=1}^4 J_i \vec{v}_i, \quad (\text{C.2})$$

where \mathcal{J} is the exchange constant, \vec{v}_i is the unit vector of the Ising axis of the spin i in the tetrahedron, J_i the spin state of the Ising spin, being -1 or 1 depending on whether the spin points out of or into the tetrahedron, respectively; \vec{B} is the magnetic-field vector. The Ising axes are distinct for the sublattices of the vertices of the tetrahedra:

$$\vec{v}_1 = \sqrt{1/3}[\bar{1}\bar{1}\bar{1}], \quad \vec{v}_2 = \sqrt{1/3}[\bar{1}11], \quad \vec{v}_3 = \sqrt{1/3}[1\bar{1}1], \quad \vec{v}_4 = \sqrt{1/3}[11\bar{1}]. \quad (\text{C.3})$$

Minimizing eq. (C.2) gives the magnetic ground state. The ground state is a mixture of the six states with two of the spins pointing in and the other two pointing out of the tetrahedron. The average magnetic moment of an ion in the tetrahedron in the ground state is given by:

$$\vec{m} = \frac{1}{4} \sum_{i=1}^4 10\mu_B J_i \vec{v}_i. \quad (\text{C.4})$$

At finite temperatures, I need to average over all states ψ (in this case $2^4 = 16$) with a Boltzmann factor as probability weight, to obtain the values for the magnetic moment of a tetrahedron:

$$\langle \vec{m} \rangle = \frac{1}{Z} \sum_{\psi} \left(\sum_{i=1}^4 10\mu_B J_i \vec{v}_i \right) e^{\langle \psi | \mathcal{H} | \psi \rangle / k_B T}, \quad \text{with} \quad Z = \sum_{\psi} e^{\langle \psi | \mathcal{H} | \psi \rangle / k_B T}, \quad (\text{C.5})$$

where Z denotes the partition sum of the system. The magnetic moment in direction of the magnetic field is given by

$$m_H = \vec{m} \cdot \frac{\vec{B}}{|B|}. \quad (\text{C.6})$$

From the magnetic moment, I easily calculate the (volume specific) magnetization by dividing the magnetic moment by the volume it occupies:

$$\vec{M} = N_{uc} \vec{m} / V_{uc}. \quad (\text{C.7})$$

In the case of pyrochlore, $N_{uc} = 16$ ions occupy the volume V_{uc} of one unit cell. The torque on a tetrahedron in a magnetic field is calculated via:

$$\vec{T} = \vec{m} \times \mu_0 \vec{H}. \quad (\text{C.8})$$

The global properties of a single crystal are very well approximated by the properties of a tetrahedron as it's smallest building block. In the next section this model is explored for the case of $\text{Dy}_2\text{Ti}_2\text{O}_7$, analogous results are valid for $\text{Ho}_2\text{Ti}_2\text{O}_7$.

C.1.1. Properties of a tetrahedron in a field in $[1\ 1\ 1]$ direction for $\text{Dy}_2\text{Ti}_2\text{O}_7$

For simplicity, the magnetic measurements of [67] are used to fix the only parameter of this model, $\mathcal{J} = -0.6\text{ meV}$ for $\text{Dy}_2\text{Ti}_2\text{O}_7$; this parameter influences the transition from the kagome-ice to the monopole-saturated state. As mentioned before, each tetrahedron has four ions with two possible states. Hence, there are $2^4 = 16$ possible configurations per tetrahedron. At first, I am interested in the probability to find a specific tetrahedron in one of the 16 states. Figure C.1 shows the probability of the seven states occupied at a temperature of 0.3 K in dependence of the magnetic field applied along $[1\ 1\ 1]$ direction (the other nine states are almost not occupied). There are six states with spin-ice configuration (two spins pointing in and two pointing out) and one state with three spins pointing in and one pointing out. At zero field, each of the 2-in-2-out states is equally probable. At small fields, the 2-in-2-out configurations with the spin with Ising axis \vec{v}_1 pointing out of the tetrahedron are stabilized, these are the states occupied in the kagome-ice phase. At high fields, there is only one configuration left; the 3-in-1-out with the \vec{v}_1 spin pointing out and all the others pointing into the tetrahedron. This is in accordance with the usual interpretation of the transitions of the spin-ice state in a field applied along $[1\ 1\ 1]$ direction.

The field dependence of the magnetic moment component in field direction m_H following eq. (C.5) at various temperatures in dependence of the magnetic field applied along $[1\ 1\ 1]$ direction is plotted in fig. C.2. At zero field the magnetization is zero, in accordance with figs. C.1 and C.7. At small fields, the 2-in-2-out configuration with the spin with Ising axis \vec{v}_1 is energetically favored; at high fields, the 3-in-1-out configuration is favored. However, only if the temperature is too low to excite also other states, the system exhibits the magnetization of the pure states. Therefore, only at low temperatures the characteristic two steps in the magnetization from zero over the intermediate plateau to the saturation magnetization are visible. At high temperatures, the transitions are washed out and the magnetization looks like a Brillouin function with a dent.

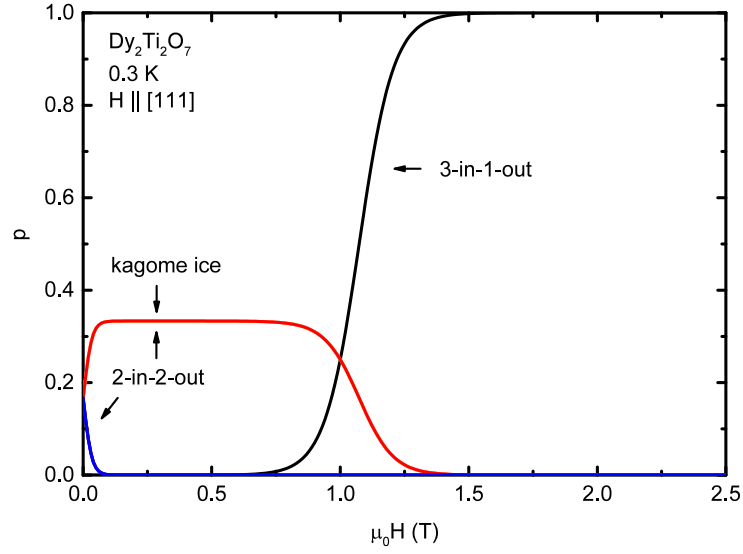


Figure C.1.: Field dependence of the distribution of tetrahedra on the states possible in a magnetic field applied along [1 1 1] direction. There are six states in the 2-in-2-out configuration, three of which compose the kagome-ice state, and one state with a 3-in-1-out configuration.

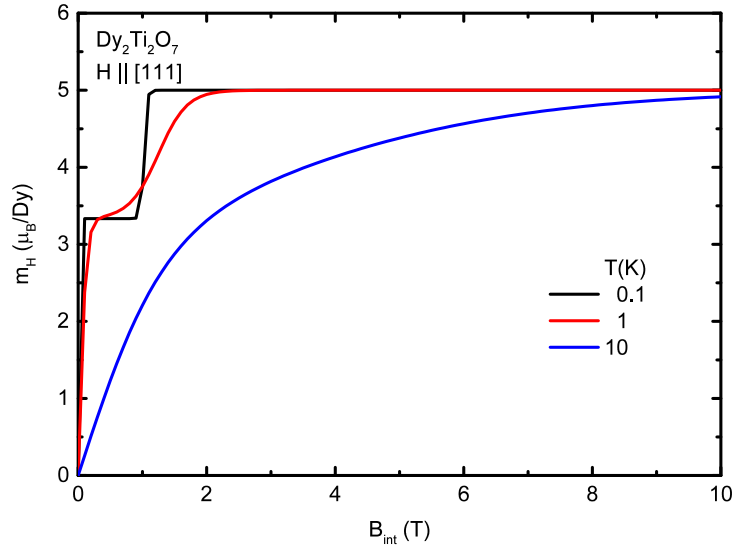


Figure C.2.: Field dependence of the magnetic moment per Dy atom for the model Hamiltonian, using eqs. (C.2) and (C.5) at various temperatures and the magnetic field applied along [1 1 1].

For the real crystal, the field inside a magnetic material differs from the external field due to demagnetizing effects. The formula for the internal field is given by:

$$B_{int} = B_{ext} - N * \mu_0 M(B_{int}), \quad (C.9)$$

$$M(B_{int}) = N_{uc} m_{uc}(B_{int}) / V_{uc}. \quad (C.10)$$

with m_{uc} being the magnetic moment per unit cell, V_{uc} being the volume per unit cell and N_{uc} the number of magnetic atoms per unit cell. By rewriting the former equation, one obtains:

$$B_{ext} = B_{int} + N * \mu_0 M(B_{int}). \quad (C.11)$$

In order to get the internal field in dependence of the external field, i.e., $B_{int}(B_{ext})$, eq. (C.11) is inverted. The magnetic moment m of $\text{Dy}_2\text{Ti}_2\text{O}_7$ depends on the internal magnetic field and has two jumps at low temperatures; one at low fields around 0.1 T and the other at around 0.9 T. So depending on the internal magnetic field the magnetic moment varies, which I denote with a factor x : $m = x \cdot \mu_B / \text{Dy}$. Using eq. (C.10), the volume-specific magnetization $\mu_0 M$ in $\text{Dy}_2\text{Ti}_2\text{O}_7$ is given by:

$$\mu_0 M = \mu_0 \frac{16x \cdot \mu_B / \text{Dy}}{1 \times 10^3 \text{ \AA}^3} = x \cdot 0.186 \text{ T}. \quad (C.12)$$

The factor x in this equation is obtained from fig. C.2. The field-dependence of the demagnetizing factor is displayed in fig. C.3.

In order to explore the phase diagram of this model, I define an order parameter ξ counting the spins pointing into a tetrahedron:

$$\xi = (S_1 + S_2 + S_3 + S_4 + 4) / 2. \quad (C.13)$$

Figure C.4(a) displays the temperature-field phase diagram of ξ of $\text{Dy}_2\text{Ti}_2\text{O}_7$. The spin-ice and kagome-ice phase is the phase-space area at low fields where $\xi = 2$ for the 2-in-2-out configuration. At high fields, the saturated monopole phase with $\xi = 3$ is reached.

The fluctuations of ξ have been calculated as $\langle (\Delta\xi)^2 \rangle$ and are shown in fig. C.4(b). The spin-ice phase is here clearly seen to be limited to low temperatures and low fields, where fluctuations of ξ are small. At a field of around 1 T, there is a transition marked by a small region of increased fluctuation. Above this transition, the saturated monopole phase is reached where spin fluctuations are small. Increasing the temperature at low fields, the system leaves the spin-ice region with little dynamics into a quasi-paramagnetic

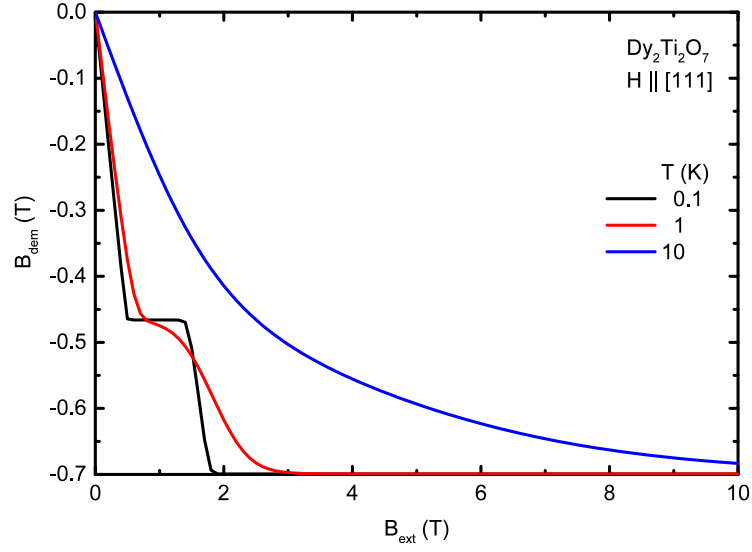


Figure C.3.: The demagnetization correction $B_{dem} = B_{int} - B_{ext}$ over the external magnetic field for various temperatures for $\text{Dy}_2\text{Ti}_2\text{O}_7$ with demagnetizing factor $N = 0.7$. We used eqs. (C.5) and (C.11) to plot this graph.

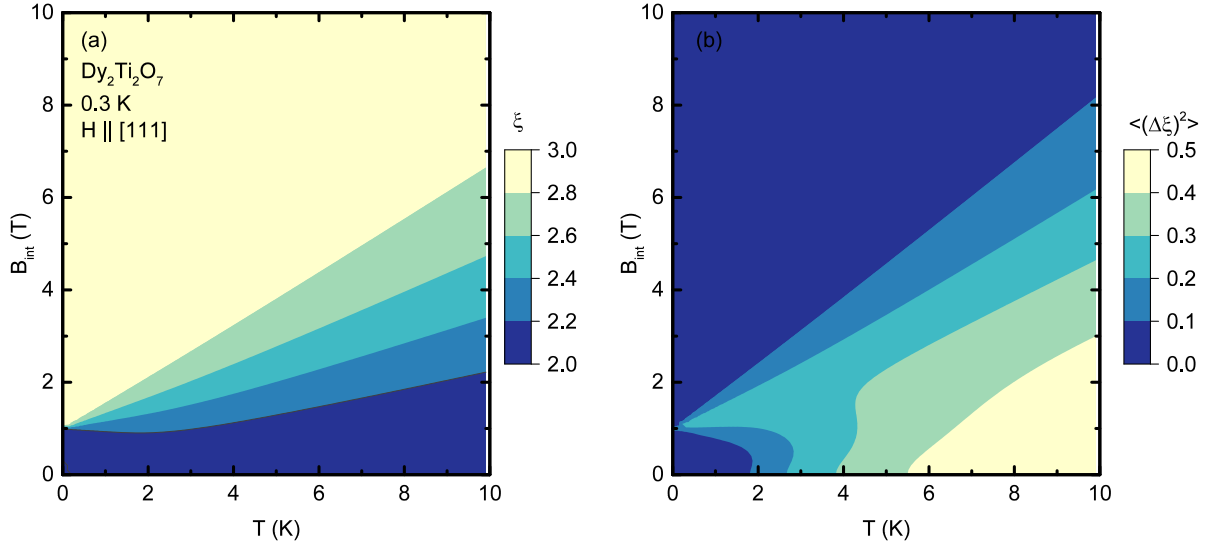


Figure C.4.: Plot of (a) the order parameter ξ and (b) the fluctuations of the order parameter ξ plotted in the temperature-field diagram.

region where the fluctuations become larger with increasing temperature. In this model the spin-ice region ends at around 1.75 K.

In the following, I present how several properties depend on the orientation of the magnetic field with respect to the sample. For this I introduce spherical coordinates (H, θ, ϕ) , with H denoting the amplitude of the magnetic field, θ being the inclination angle and ϕ the azimuthal angle. In order to have a good angular resolution in the graphs, I transform the coordinate system such that the $[1\ 1\ 1]$ direction is at the equator of the spherical coordinates at $\theta = \pi/2$. In accordance with other publications, I transform the z axis into the $[1\ 1\ \bar{2}]$ direction and the x axis into the $[\bar{1}\ 1\ 0]$ direction. Hence, the transformation matrix is:

$$\vec{H} = H \begin{pmatrix} -\sqrt{1/2} & \sqrt{1/3} & \sqrt{1/6} \\ \sqrt{1/2} & \sqrt{1/3} & \sqrt{1/6} \\ 0 & \sqrt{1/3} & -2\sqrt{1/6} \end{pmatrix} \begin{pmatrix} \sin(\theta) \cos(\phi) \\ \sin(\theta) \sin(\phi) \\ \cos(\theta) \end{pmatrix}. \quad (\text{C.14})$$

The orientation of the coordinate axes and the angles θ and ϕ are depicted in fig. C.5.

In order to verify, that this simple model captures the basic spin-ice physics I calculate the dependence of m_H (eq. (C.6)) on the inclination angle θ at 0.3 K and compare it to experiment [130]. The result of my calculation is shown in fig. C.6. In this plot, $\theta = \pi/2$ points in the $[1\ 1\ 1]$ direction, for $\theta \neq \pi/2$, passes through all directions in the $[1\ \bar{1}\ 0]$ plane: most importantly in direction of the $[1\ 1\ \bar{1}]$, $[0\ 0\ 1]$ and the $[1\ 1\ 0]$ direction. The $[0\ 0\ 1]$ direction is at $\theta \approx 2.5$ and the $[1\ 1\ 0]$ direction is at around $\theta \approx 1$ where m_H has the global and a local maximum, respectively. The $[1\ 1\ \bar{1}]$ direction is around $\theta \approx 0.3$ and equivalent to the $[1\ 1\ 1]$ direction at $\theta = \pi/2$ showing the same behaviour. At 1 T the magnetization starts to approach the saturation value and at $\theta = \pi/2$ a local maximum appears, whereas below the transition at around 0.9 T there is a local minimum of m_H at $\theta = \pi/2$. My calculation agrees well with the experimental data reported in the literature [130].

C.1.2. Properties of a tetrahedron in a field slightly off the $[1\ 1\ 1]$ direction

In this section, I show that a slight deviation of the magnetic field from the $[1\ 1\ 1]$ direction of the crystal can influence the measurements of various physical properties. This can be seen in fig. C.7 where the probability of the states of a tetrahedron is displayed for a magnetic field deviating by two degrees from the $[1\ 1\ 1]$ direction of the crystal. One of the three 2-in-2-out kagome-ice states is favored due to the deviation which leads to considerable transverse components of the magnetization vector perpendicular to the magnetic field. For the exactly aligned field no kagome-ice configuration is favored (fig. C.1) and the

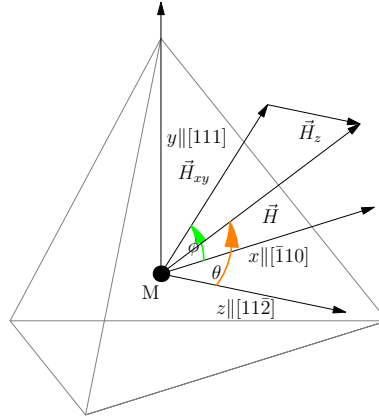


Figure C.5.: The notation of the coordinate axes and the angles θ and ϕ with respect to the tetrahedron.

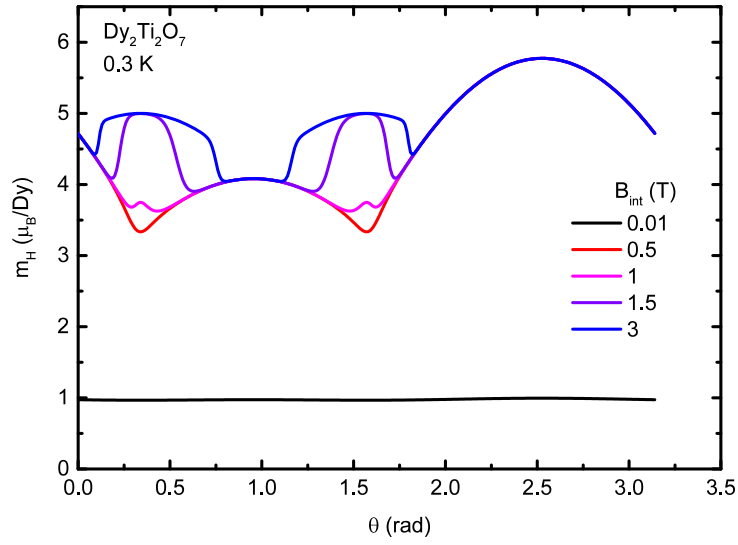


Figure C.6.: Angular dependence of the magnetization m_H along the magnetic field at 0.3 K at various fields. $\theta = \pi/2$ points along the $[1\ 1\ 1]$ direction and θ is the angle between $[1\ 1\ 1]$ and the field in the $\bar{1}\ 1\ 0$ plane. This graph is a slice of the graphs in fig. C.8 at $\phi = \pi/2$.

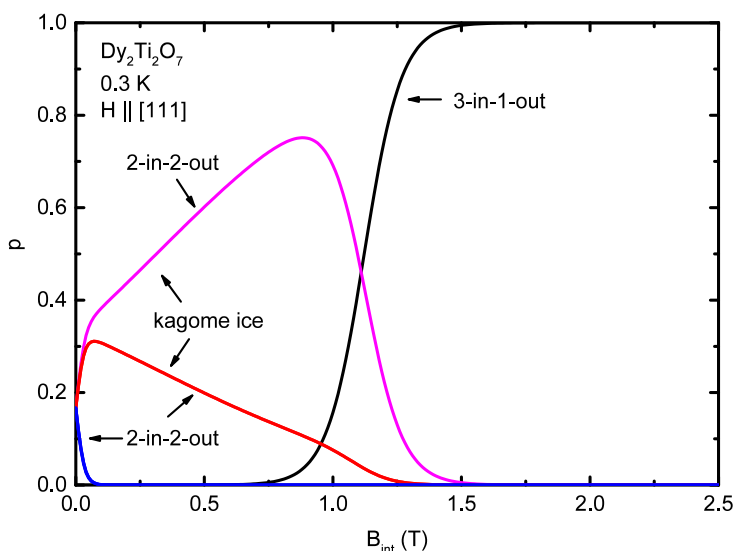


Figure C.7.: Field dependence of the distribution of tetrahedra on the states possible in a magnetic field deviating two degrees from the $[111]$ direction. As in fig. C.1 there are seven states occupied: six states in the 2-in-2-out configuration, three of which compose the kagome-ice state with one being favored due to the misalignment of the field, and one state with a 3-in-1-out configuration.

transverse field is zero. Components of the magnetization perpendicular to the magnetic field may result in a strong torque on the crystal. This effect may be important at low temperature where the magnetization plateau of the kagome-ice phase is well defined.

The plots in fig. C.8, shown for a fixed H , the value of the component of the magnetic moment m_H parallel to the magnetic field (eq. (C.6)) at each point (θ, ϕ) at the temperature of 0.3 K. The $[111]$ direction is located at $(\pi/2, \pi/2)$. There are several equivalent points in this graph, notably the four equivalent $[111]$ directions and the four reversed $[111]$ directions giving eight instable fix points below 0.9 T and stable fix points above 0.9 T; the second set are the equivalent $[100]$ directions with their reversed directions giving six equivalent stable fix points for all fields. At low fields of $\mu_0 H = 0.01$ T or 0.5 T (fig. C.8(a) and (b)), m_H has a minimum at the $[111]$ direction. That means, that energy can be gained at low fields by turning the tetrahedron out of its orientation. With increasing field strength up to 1 T the gradient of m_H around the equivalent $[111]$ directions becomes steeper, so that more energy can be gained by reorienting the tetrahedron, fig. C.8(c). When the field is so high that the saturation magnetization is reached, the local minimum at $[111]$ becomes a local maximum; consequently, small deviations from this direction decrease the Zeeman energy of the tetrahedron, fig. C.8(d)-(f). The easy axes are the $[100]$, $[010]$ and the $[001]$ directions for all field strengths. Last but not least, in the

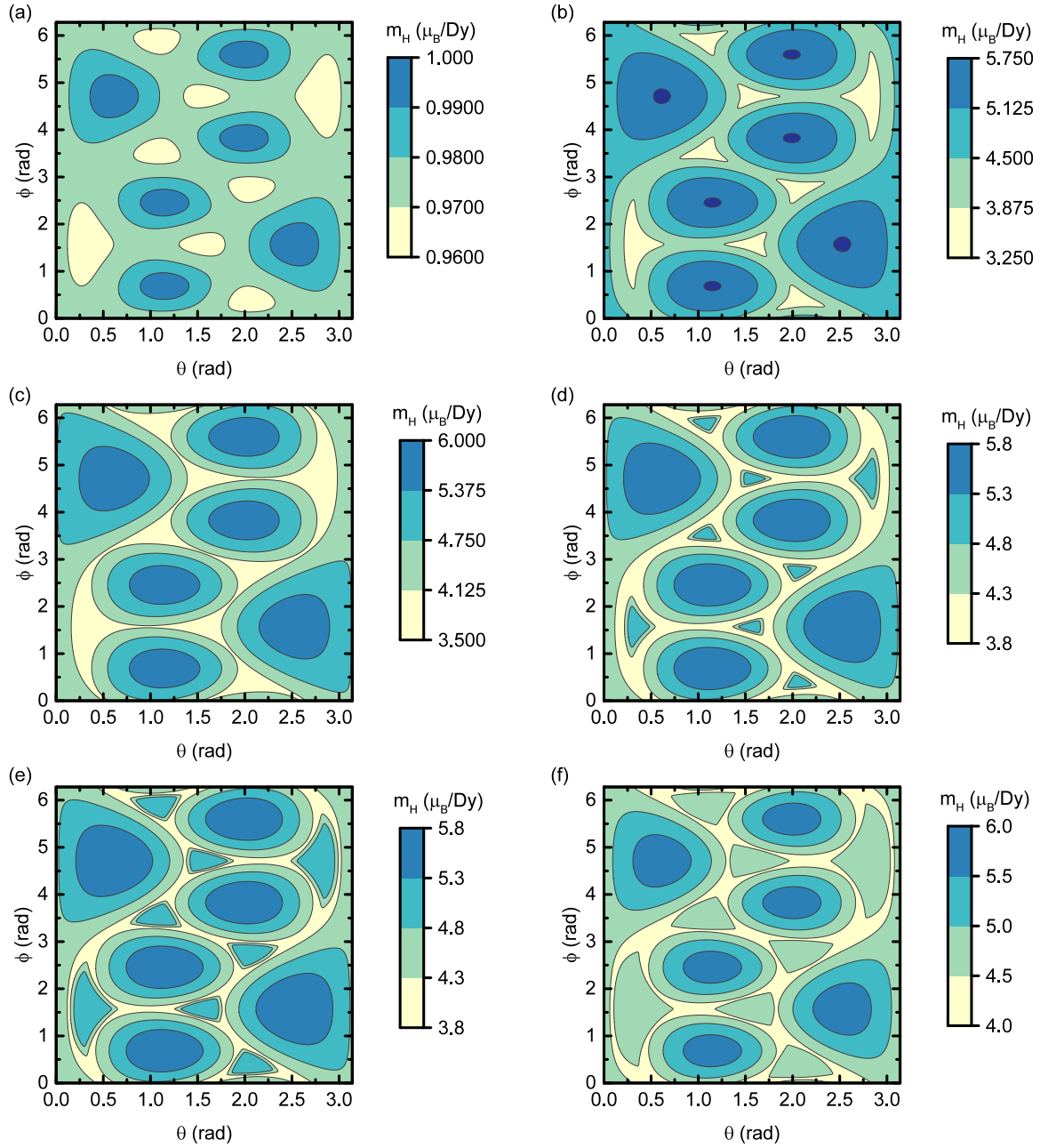


Figure C.8.: Contour plot of the parallel magnetic moment m_H at 0.3 K in dependence of the direction of the magnetic field given by the polar and azimuthal angles ϕ and θ , respectively. The $[111]$ direction is located at $\theta = \phi = \pi/2$; $[11\bar{2}]$ and $[\bar{1}10]$ directions are at the origin $\theta = \phi = 0$ and at $\theta = \pi/2, \phi = 0$, respectively. The magnetic field is different for the six plots being (a) 0.01, (b) 0.5, (c) 1, (d) 1.5, (e) 2 and (f) 3 T from left to right, top to bottom. The calculation was done via eqs. (C.2) and (C.5).

middle between neighboring equivalent $[1\ 1\ 1]$ direction there are saddle points of m_H , i.e., they are maxima on the line connecting the neighboring $[1\ 1\ 1]$ directions, but minima perpendicular to that line. To summarize, at low fields the $[1\ 1\ 1]$ direction is unstable to small deviations and at high fields it is stable.

Consequently, I am interested, how strong a torque would be if the field was not properly aligned with the $[1\ 1\ 1]$ direction. Such a torque could rotate the sample leading to an apparent sample length change independent of the inherent properties of the sample. The plots in fig. C.9 show the norm of the torque vector \vec{T} at each field direction (θ, ϕ) at a temperature of 0.3 K and fixed field strength H . In this plot, as in fig. C.8 the red dot is located at $(\pi/2, \pi/2)$ corresponding to the $[1\ 1\ 1]$ direction. Exactly at that point, the norm of \vec{T} is zero for all fields; however, the slope of the torque is large around that point for fields below the transition to the 3-in-1-out configuration, so that for small deviations there is considerable torque. From the magnetization data visualized in fig. C.8 it follows that the torque is directed so that it rotates the tetrahedron such that the field points less in the $[1\ 1\ 1]$ direction. The $[1\ 1\ 1]$ direction is an unstable fix point at small fields. There are in total eight points equivalent to the one marked by the red dot, given by the four equivalent $[1\ 1\ 1]$ directions and their opposite directions. Additionally, there are twelve unstable fix points at the equivalent $[1\ 1\ 0]$ directions and their reversed directions; these are located in the middle between the $[1\ 1\ 1]$ directions. At these points, the torque has a saddle point. The stable fix points, where the torque is zero because the magnetization is aligned along the magnetic field are the easy axes $[1\ 0\ 0]$, $[0\ 1\ 0]$ and the $[0\ 0\ 1]$ and their opposite directions. At fields higher than about 1 T the torque around the $[1\ 1\ 1]$ direction changes sign so that the tetrahedron is rotated into the $[1\ 1\ 1]$ direction. Therefore, the unstable fix points at $[1\ 1\ 1]$ and equivalent become stable at high fields. The easy axes $[1\ 0\ 0]$, $[0\ 1\ 0]$ and $[0\ 0\ 1]$ remain stable.

In order to gain a better understanding of what direction the torque will rotate the tetrahedron to, I computed the projection of the torque on the vector $\vec{e}_\phi = (\sqrt{1/2}, -\sqrt{1/2}, 0)$ for all directions in the $[\bar{1}\ 1\ 0]$ plane. This projection of the torque in ϕ direction is the part that leads to a rotation in the $[\bar{1}\ 1\ 0]$ plane, leading to a rotation changing θ . Depending on the value of $T_\theta = \vec{T} \cdot \vec{e}_\phi$ the angle θ changes: a positive T_θ decreases θ via a clockwise rotation of the tetrahedron (around \vec{e}_ϕ), a negative T_θ increases θ via a counterclockwise rotation. A point where T_θ changes sign from negative to positive is stable with respect to deviations in θ , a point where it crosses from positive to negative is unstable. Figure C.10 represents a slice from fig. C.9 along the $\phi = \pi/2$ line showing the dependence of T_θ on θ . It can be seen, that the fix point for $\theta \approx 2.5$ ($[0\ 0\ 1]$ direction) is stable for all fields, as is the one at around $\theta \approx 0.9$ ($[1\ 1\ 0]$ direction). The latter, however, is unstable with respect

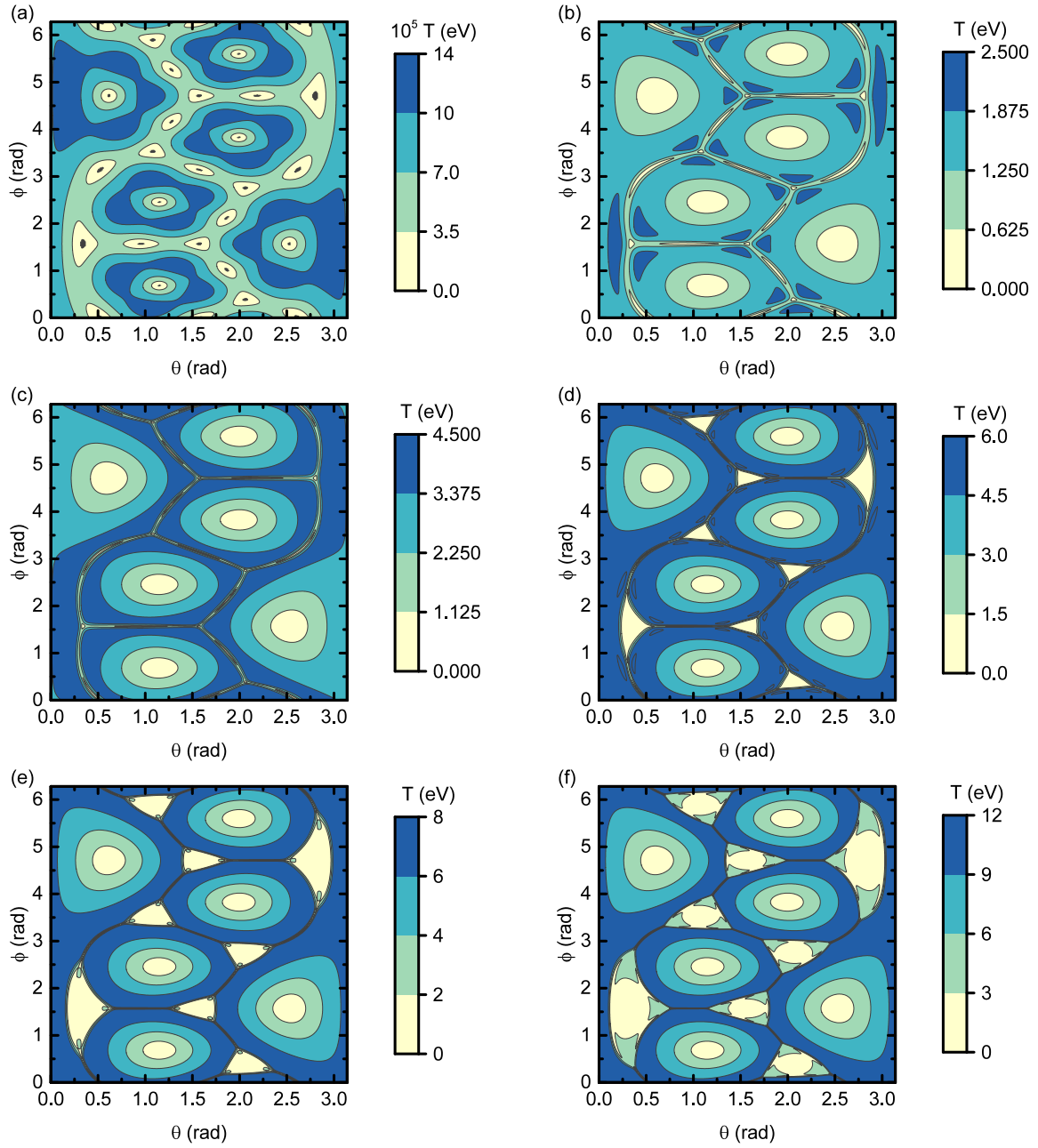


Figure C.9.: Contour plot of the norm of the torque $|T|$ (eq. (C.8)) at 0.3 K in dependence of the direction of the magnetic field given by the polar and the azimuthal angles ϕ and θ , respectively. The $[111]$ direction is located at $\theta = \phi = \pi/2$; $[11\bar{2}]$ and $[\bar{1}10]$ directions are at the origin $\theta = \phi = 0$ and at $\theta = \pi/2, \phi = 0$, respectively. The magnetic field is different for the six plots being 0.01, 0.5, 1, 1.5, 2 and 3 T from left to right, top to bottom.

to deviations in ϕ . The two points at $\theta = 0$ and $\theta \approx -1.2$ belong to equivalent [1 1 1] directions. These two points are unstable for $\mu_0 H = 0.5$ T and 1 T and stable for higher fields as was seen in the results of the calculation of the magnetization m_H (fig. C.6).

Finally, I investigated the field dependence of T_θ for a small positive deviation of two degrees in the inclination angle θ from the point $(\pi/2, \pi/2)$ corresponding to the [1 1 1] direction, that is $(\pi/2 + 2\pi/180, \pi/2)$ (fig. C.11). Positive values of T_θ decrease θ , i.e., would reduce the deviation, and negative values increase θ . i.e., enlarge the deviation. For low temperatures and low fields, there is a strong torque increasing the deviation that suddenly changes sign after the transition to the 3-in-1-out configuration then decreasing the deviation, compare with fig. C.7. At higher temperatures the torque becomes much smaller.

In the experiment, I am interested in the inherent properties of the compounds, I need to make sure that the torque on the sample does not lead to a rotation of the sample interfering with my measurements. Therefore, all external forces and torques on the sample should vanish. An estimation of the typical magnetic torque on a sample and a typical compensating torque exerted on the sample by the dilatometer cell are needed. A typical sample had a mass of the order of $m = 50$ mg and a length in the order of 1 mm; the molar mass of $\text{Dy}_2\text{Ti}_2\text{O}_7$ is $M = 532.73$ g mol⁻¹. Together with a typical torque of 1 T $\cdot \mu_B/\text{Dy}$ (compare with fig. C.11) I obtain the torque:

$$\begin{aligned} T_{\text{sample}} &= \frac{m}{M} N_A T_{\text{tetrahedron}} \\ &= \frac{6.022 \times 10^{23} \text{ mol}^{-1} 50 \text{ mg}}{532.73 \text{ g mol}^{-1}} \cdot 2 \times 1 \text{ T} \cdot 9.274 \times 10^{-24} \text{ Nm/T/Dy}_2\text{Ti}_2\text{O}_7 \\ &= 1.048 \times 10^{-3} \text{ N m}. \end{aligned}$$

The torque from the dilatometer spring (TDC) with a spring force of 3 N:

$$T = 3 \text{ N} \cdot 1 \text{ mm} = 3 \times 10^{-3} \text{ N m}.$$

Therefore, the magnetic torque is in the same order of magnitude as the torque from the spring force and could interfere with our measurements. I glued the sample to the frame of the dilatometer cell (TDC) in order to compensate for the torque in an additional way, see subsection 3.3.2. This seemed to be sufficient, since I measured realistic magnetostriction effects.

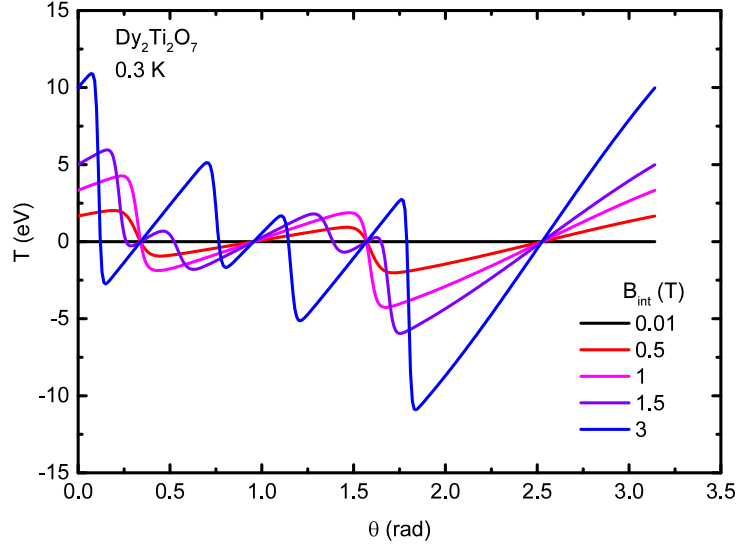


Figure C.10.: Angular dependence of $\vec{T} \cdot (\sqrt{1/2}, -\sqrt{1/2}, 0)$ at a temperature of 0.3 K at various fields. $\theta = \pi/2$ points along the $[111]$ direction and θ is the angle between $[111]$ and the field in the $[\bar{1}10]$ plane. $\theta = 0$ corresponding to the $[111]$ direction and θ is the angle between $[111]$ and the field in the $[\bar{1}10]$ plane.

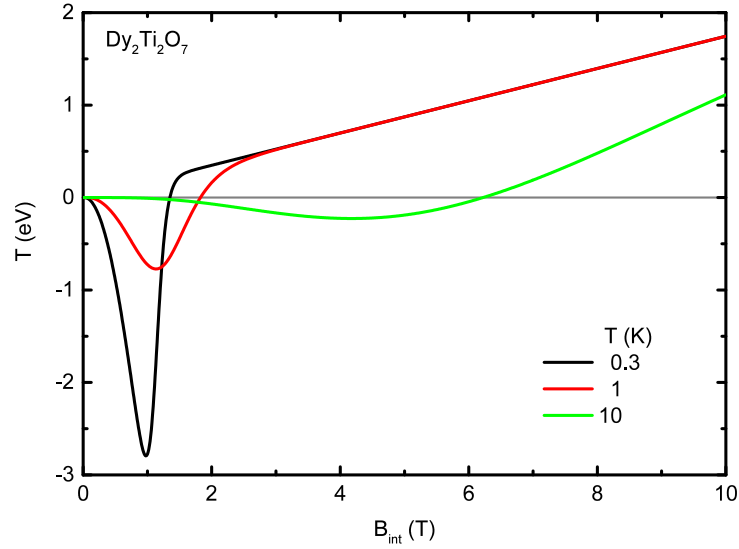


Figure C.11.: Field dependence of the torque projected on $\vec{e}_\phi = (\sqrt{1/2}, -\sqrt{1/2})$ using eqs. (C.2) and (C.4) (for zero temperature) and eq. (C.5) at finite temperatures. The field dependence is computed for $\theta = \pi/2 + 2\pi/180$ and $\phi = \pi/2$.

Bibliography

- [1] P. W. Anderson, Phys. Rev. **102**, 1008 (1956).
- [2] J. E. Greedan, J. Mater. Chem. **11**, 37 (2001).
- [3] A. Ramirez, Annu. Rev. Mater. Sci. **24**, 453 (1994).
- [4] J. Wosnitza, S. A. Zvyagin, and S. Zherlitsyn, Rep. Prog. Phys. **79**, 074504 (2016).
- [5] J. E. Greedan, J. Alloys Compd. **408-412**, 444 (2006).
- [6] J. S. Gardner, M. J. P. Gingras, and J. E. Greedan, Rev. Mod. Phys. **82**, 53 (2010).
- [7] L. Balents, Nature **464**, 199 (2010).
- [8] A. A. Zvyagin, Low Temp. Phys. **39**, 901 (2013).
- [9] C. Castelnovo, R. Moessner, and S. Sondhi, Annu. Rev. Condens. Matter Phys. **3**, 35 (2012).
- [10] F. K. K. Kirschner, F. Flicker, A. Yacoby, N. Y. Yao, and S. J. Blundell, Phys. Rev. B **97**, 140402(R) (2018).
- [11] M. J. P. Gingras and P. A. McClarty, Rep. Progr. Phys. **77**, 056501 (2014).
- [12] S. Zherlitsyn, S. Yasin, J. Wosnitza, A. A. Zvyagin, A. V. Andreev, and V. Tsurkan, Low Temp. Phys. **40**, 123 (2014).
- [13] M. Lines, Phys. Rep. **55**, 133 (1979).
- [14] T. Barron, J. Collins, and G. White, Adv. Phys. **29**, 609 (1980).
- [15] M. Doerr, M. Rotter, and A. Lindbaum, Adv. Phys. **54**, 1 (2005).
- [16] E. Bauer and M. Rotter, in *Properties and Applications of Complex Intermetallics* (WORLD SCIENTIFIC, 2009) pp. 183–248.

- [17] M. Rotter, M. D. Le, A. T. Boothroyd, and J. A. Blanco, *J. Phys.: Cond. Mat.* **24**, 213201 (2012).
- [18] M. Rotter, D. M. Le, J. Keller, L. G. Pascut, T. Hoffmann, M. Doerr, R. Schedler, P. Fabi, S. Rotter, M. Banks, and N. Klüver, *McPhase User Manual* (2013).
- [19] S. Erfanifam, S. Zherlitsyn, S. Yasin, Y. Skourski, J. Wosnitza, A. A. Zvyagin, P. McClarty, R. Moessner, G. Balakrishnan, and O. A. Petrenko, *Phys. Rev. B* **90**, 064409 (2014).
- [20] R. Pott and R. Schefzyk, *J. Phys. E Sci. Instrum.* **16**, 444 (1983).
- [21] M. O. Steinitz, J. Genossar, W. Schnepf, and D. A. Tindall, *Rev. Sci. Instrum.* **57**, 297 (1986).
- [22] M. Rotter, H. Müller, E. Gratz, M. Doerr, and M. Loewenhaupt, *Rev. Sci. Instrum.* **69**, 2742 (1998).
- [23] R. KÜchler, T. Bauer, M. Brando, and F. Steglich, *Rev. Sci. Instrum.* **83**, 095102 (2012).
- [24] F. R. Kroeger and C. A. Swenson, *J. Appl. Phys.* **48**, 853 (1977).
- [25] N. Mehboob, *Magnetostriction of $GdAg_2$, $PrFe_4As_{12}$, and $GdVO_3$ measured with a Capacitance Dilatometer*, Ph.D. thesis, Universität Wien, Wien (2009).
- [26] C. R. Wiebe and A. M. Hallas, *APL Materials* **3**, 041519 (2015).
- [27] M. . Subramanian, G. Aravamudan, and G. Subba Rao, *Prog. Solid State Chem.* **15**, 55 (1983).
- [28] R. Mouta, R. X. Silva, and C. W. A. Paschoal, *Acta Crystallogr. Sec. B* **69**, 439 (2013).
- [29] H. . Zhou, S. Bramwell, J. Cheng, C. Wiebe, G. Li, L. Balicas, J. Bloxsom, H. Silverstein, J. Zhou, J. Goodenough, and J. Gardner, *Nat. Commun.* **2**, 478 (2011).
- [30] H. D. Zhou, J. G. Cheng, A. M. Hallas, C. R. Wiebe, G. Li, L. Balicas, J. S. Zhou, J. B. Goodenough, J. S. Gardner, and E. S. Choi, *Phys. Rev. Lett.* **108**, 207206 (2012).

- [31] T. Stoeter, M. Antlauf, J. Gronemann, T. Hermannsdörfer, S. Granovsky, M. Schwarz, M. Doerr, H.-H. Klauss, E. Kroke, and J. Wosnitza, arXiv e-prints , arxiv:1809.01480 (2018), 1809.01480 .
- [32] J. M. Farmer, L. A. Boatner, B. C. Chakoumakos, M.-H. Du, M. J. Lance, C. J. Rawn, and J. C. Bryan, *J. Alloys Compd.* **605**, 63 (2014).
- [33] P. Santini, S. Carretta, G. Amoretti, R. Caciuffo, N. Magnani, and G. H. Lander, *Rev. Mod. Phys.* **81**, 807 (2009).
- [34] J. Jensen, *Rare Earth Magnetism*.
- [35] C.-G. Ma, M. Brik, D.-X. Liu, B. Feng, Y. Tian, and A. Suchocki, *J. Lumin.* **170**, 369 (2016).
- [36] K. W. H. Stevens, *Proc. Phys. Soc. Sec. A* **65**, 209 (1952).
- [37] H. Fieß, *International tables for crystallography* (Springer, Berlin, 2006).
- [38] B. R. Judd, *Proc. Roy. Soc. Lond. Math. Phys. Sci.* **227**, 552 (1955).
- [39] M. Hutchings, in *Solid State Physics*, Vol. 16 (Elsevier, 1964) pp. 227–273.
- [40] A. Bertin, Y. Chapuis, P. Dalmas de Réotier, and A. Yaouanc, *J. Phys.: Cond. Mat.* **24**, 256003 (2012).
- [41] B. Malkin, T. T. A. Lummen, P. H. M. van Loosdrecht, G. Dhahlenne, and A. R. Zakirov, *J. Phys.: Cond. Mat.* **22**, 276003 (2010).
- [42] M. Ruminy, E. Pomjakushina, K. Iida, K. Kamazawa, D. T. Adroja, U. Stuhr, and T. Fennell, *Phys. Rev. B* **94**, 024430 (2016).
- [43] L. F. Chibotaru and N. Iwahara, *New J. Phys.* **17**, 103028 (2015).
- [44] S. B. Lee, S. Onoda, and L. Balents, *Phys. Rev. B* **86**, 104412 (2012).
- [45] K. A. Ross, L. Savary, B. D. Gaulin, and L. Balents, *Phys. Rev. X* **1**, 021002 (2011).
- [46] S. Onoda and Y. Tanaka, *Phys. Rev. B* **83**, 094411 (2011).
- [47] M. Hermele, M. P. A. Fisher, and L. Balents, *Phys. Rev. B* **69**, 064404 (2004).
- [48] L. Savary and L. Balents, *Phys. Rev. Lett.* **108**, 037202 (2012).

- [49] Y.-P. Huang, G. Chen, and M. Hermele, *Phys. Rev. Lett.* **112**, 167203 (2014).
- [50] J. G. Rau and M. J. P. Gingras, *Phys. Rev. B* **92**, 144417 (2015).
- [51] S. T. Bramwell and M. J. Harris, *J. Phys.: Cond. Mat.* **10**, L215 (1998).
- [52] S. T. Bramwell, *Science* **294**, 1495 (2001).
- [53] R. Moessner, *Phys. Rev. B* **57**, R5587 (1998).
- [54] B. C. den Hertog and M. J. P. Gingras, *Phys. Rev. Lett.* **84**, 3430 (2000).
- [55] J. G. Rau and M. J. P. Gingras, *Nat. Commun.* **7**, 12234 (2016).
- [56] C. Castelnovo, R. Moessner, and S. L. Sondhi, *Nature* **451**, 42 (2008).
- [57] A. P. Ramirez, A. Hayashi, R. J. Cava, R. Siddharthan, and B. S. Shastry, *Nature* **399**, 333 (1999).
- [58] R. Moessner and S. L. Sondhi, *Phys. Rev. B* **68**, 064411 (2003).
- [59] S. V. Isakov, K. S. Raman, R. Moessner, and S. L. Sondhi, *Phys. Rev. B* **70**, 104418 (2004).
- [60] L. C. Jaubert and P. C. W. Holdsworth, *J. Phys.: Cond. Mat.* **23**, 164222 (2011).
- [61] C. Castelnovo, R. Moessner, and S. L. Sondhi, *Phys. Rev. Lett.* **104**, 107201 (2010).
- [62] S. Mostame, C. Castelnovo, R. Moessner, and S. L. Sondhi, *Proc. Natl. Acad. Sci. USA* **111**, 640 (2014).
- [63] H. Fukazawa, R. Melko, R. Higashinaka, Y. Maeno, and M. Gingras, *Phys. Rev. B* **65**, 054410 (2002).
- [64] K. Matsuhira, Y. Hinatsu, K. Tenya, and T. Sakakibara, *J. Phys.: Cond. Mat.* **12**, L649 (2000).
- [65] M. J. Harris, S. T. Bramwell, D. F. McMorrow, T. Zeiske, and K. W. Godfrey, *Phys. Rev. Lett.* **79**, 2554 (1997).
- [66] L. Opherden, T. Herrmannsdörfer, M. Uhlarz, D. I. Gorbunov, A. Miyata, O. Portugall, I. Ishii, T. Suzuki, H. Kaneko, H. Suzuki, and J. Wosnitza, *Phys. Rev. B* **99**, 085132 (2019).

- [67] K. Matsuhira, Z. Hiroi, T. Tayama, S. Takagi, and T. Sakakibara, *J. Phys.: Cond. Mat.* **14**, L559 (2002).
- [68] C. Krey, S. Legl, S. R. Dunsiger, M. Meven, J. S. Gardner, J. M. Roper, and C. Pfleiderer, *Phys. Rev. Lett.* **108**, 257204 (2012).
- [69] Z. Hiroi, K. Matsuhira, S. Takagi, T. Tayama, and T. Sakakibara, *J. Phys. Soc. Jpn.* **72**, 411 (2003).
- [70] S. T. Bramwell, M. J. Harris, B. C. den Hertog, M. J. P. Gingras, J. S. Gardner, D. F. McMorrow, A. R. Wildes, A. L. Cornelius, J. D. M. Champion, R. G. Melko, and T. Fennell, *Phys. Rev. Lett.* **87**, 047205 (2001).
- [71] T. Fennell, S. T. Bramwell, D. F. McMorrow, P. Manuel, and A. R. Wildes, *Nat. Phys.* **3**, 566 (2007).
- [72] H. Kadowaki, N. Doi, Y. Aoki, Y. Tabata, T. J. Sato, J. W. Lynn, K. Matsuhira, and Z. Hiroi, *J. Phys. Soc. Jpn.* **78**, 103706 (2009).
- [73] R. G. Melko and M. J. P. Gingras, *J. Phys.: Cond. Mat.* **16**, R1277 (2004).
- [74] R. G. Melko, B. C. den Hertog, and M. J. P. Gingras, *Phys. Rev. Lett.* **87**, 067203 (2001).
- [75] G. Balakrishnan, O. A. Petrenko, M. R. Lees, and D. M. Paul, *J. Phys.: Cond. Mat.* **10**, L723 (1998).
- [76] J. A. Osborn, *Phys. Rev.* **67**, 351 (1945).
- [77] T. Sakakibara, T. Tayama, Z. Hiroi, K. Matsuhira, and S. Takagi, *Phys. Rev. Lett.* **90**, 207205 (2003).
- [78] O. A. Petrenko, M. R. Lees, and G. Balakrishnan, *Phys. Rev. B* **68**, 012406 (2003).
- [79] M. Rotter, D. M. Le, J. Keller, L. G. Pascut, T. Hoffmann, M. Doerr, R. Schedler, P. Fabi, S. Rotter, and M. Banks, *McPhase Software Suite*.
- [80] S. Scharffe, G. Kolland, M. Valldor, V. Cho, J. Welter, and T. Lorenz, *J. Magn. Magn. Mater* **383**, 83 (2015).
- [81] G. Kolland, M. Valldor, M. Hiertz, J. Frielingsdorf, and T. Lorenz, *Phys. Rev. B* **88**, 054406 (2013).

- [82] S. J. Li, Z. Y. Zhao, C. Fan, B. Tong, F. B. Zhang, J. Shi, J. C. Wu, X. G. Liu, H. D. Zhou, X. Zhao, and X. F. Sun, *Phys. Rev. B* **92**, 094408 (2015).
- [83] C. Fan, Z. Y. Zhao, H. D. Zhou, X. M. Wang, Q. J. Li, F. B. Zhang, X. Zhao, and X. F. Sun, *Phys. Rev. B* **87**, 144404 (2013).
- [84] D. Slobinsky, C. Castelnovo, R. A. Borzi, A. S. Gibbs, A. P. Mackenzie, R. Moessner, and S. A. Grigera, *Phys. Rev. Lett.* **105**, 267205 (2010).
- [85] M. J. Jackson, E. Lhotel, S. R. Giblin, S. T. Bramwell, D. Prabhakaran, K. Matsuhira, Z. Hiroi, Q. Yu, and C. Paulsen, *Phys. Rev. B* **90**, 064427 (2014).
- [86] S. Erfanifam, S. Zherlitsyn, J. Wosnitza, R. Moessner, O. A. Petrenko, G. Balakrishnan, and A. A. Zvyagin, *Phys. Rev. B* **84**, 220404(R) (2011).
- [87] M. Orendáč, J. Hanko, E. Čížmár, A. Orendáčová, M. Shirai, and S. T. Bramwell, *Phys. Rev. B* **75**, 104425 (2007).
- [88] H. M. Revell, L. R. Yaraskavitch, J. D. Mason, K. A. Ross, H. M. L. Noad, H. A. Dabkowska, B. D. Gaulin, P. Henelius, and J. B. Kycia, *Nat. Phys.* **9**, 34 (2013).
- [89] R. Higashinaka, H. Fukazawa, K. Deguchi, and Y. Maeno, *J. Phys.: Cond. Mat.* **16**, S679 (2004).
- [90] J. Snyder, B. G. Ueland, J. S. Slusky, H. Karunadasa, R. J. Cava, and P. Schiffer, *Phys. Rev. B* **69**, 064414 (2004).
- [91] J. A. Bloxsom, *Thermal and Magnetic Studies of Spin Ice Compounds*, Ph.D. thesis, Universität College London, London (2016).
- [92] E. R. Kassner, A. B. Eyvazov, B. Pichler, T. J. S. Munsie, H. A. Dabkowska, G. M. Luke, and J. C. S. Davis, *Proc. Natl. Acad. Sci. USA* **112**, 8549 (2015).
- [93] H. Aoki, T. Sakakibara, K. Matsuhira, and Z. Hiroi, *J. Phys. Soc. Jpn.* **73**, 2851 (2004).
- [94] K. Matsuhira, Y. Hinatsu, and T. Sakakibara, *J. Phys.: Cond. Mat.* **13**, L737 (2001).
- [95] J. Snyder, B. G. Ueland, J. S. Slusky, H. Karunadasa, R. J. Cava, A. Mizel, and P. Schiffer, *Phys. Rev. Lett.* **91**, 107201 (2003).
- [96] K. Matsuhira, C. Paulsen, E. Lhotel, C. Sekine, Z. Hiroi, and S. Takagi, *J. Phys. Soc. Jpn.* **80**, 123711 (2011).

- [97] L. R. Yaraskavitch, H. M. Revell, S. Meng, K. A. Ross, H. M. L. Noad, H. A. Dabkowska, B. D. Gaulin, and J. B. Kycia, *Phys. Rev. B* **85**, 020410(R) (2012).
- [98] H. Takatsu, K. Goto, H. Otsuka, R. Higashinaka, K. Matsubayashi, Y. Uwatoko, and H. Kadowaki, *J. Phys. Soc. Jpn.* **82**, 104710 (2013).
- [99] J. Snyder, J. S. Slusky, R. J. Cava, and P. Schiffer, *Nature* **413**, 48 (2001).
- [100] G. Ehlers, A. L. Cornelius, M. Orendáč, M. Kajnakov, T. Fennell, S. T. Bramwell, and J. S. Gardner, *J. Phys.: Cond. Mat.* **15**, L9 (2003).
- [101] G. Ehlers, A. L. Cornelius, T. Fennell, M. Koza, S. T. Bramwell, and J. S. Gardner, *J. Phys.: Cond. Mat.* **16**, S635 (2004).
- [102] J. A. Quilliam, L. R. Yaraskavitch, H. A. Dabkowska, B. D. Gaulin, and J. B. Kycia, *Phys. Rev. B* **83**, 094424 (2011).
- [103] C. Paulsen, M. J. Jackson, E. Lhotel, B. Canals, D. Prabhakaran, K. Matsuhira, S. R. Giblin, and S. T. Bramwell, *Nat. Phys.* **10**, 135 (2014).
- [104] D. Pomaranski, L. R. Yaraskavitch, S. Meng, K. A. Ross, H. M. L. Noad, H. A. Dabkowska, B. D. Gaulin, and J. B. Kycia, *Nat. Phys.* **9**, 353 (2013).
- [105] S. R. Giblin, M. Twengström, L. Bovo, M. Ruminy, M. Bartkowiak, P. Manuel, J. C. Andresen, D. Prabhakaran, G. Balakrishnan, E. Pomjakushina, C. Paulsen, E. Lhotel, L. Keller, M. Frontzek, S. C. Capelli, O. Zaharko, P. A. McClarty, S. T. Bramwell, P. Henelius, and T. Fennell, *Phys. Rev. Lett.* **121**, 067202 (2018).
- [106] P. Henelius, T. Lin, M. Enjalran, Z. Hao, J. G. Rau, J. Altosaar, F. Flicker, T. Yavors'kii, and M. J. P. Gingras, *Phys. Rev. B* **93**, 024402 (2016).
- [107] J. G. Rau and M. J. P. Gingras, *Annu. Rev. Condens. Matter Phys.* **10**, 357 (2019).
- [108] G. Sala, M. J. Gutmann, D. Prabhakaran, D. Pomaranski, C. Mitchelitis, J. B. Kycia, D. G. Porter, C. Castelnovo, and J. P. Goff, *Nat. Mater.* **13**, 488 (2014).
- [109] G. D. Blundred, C. A. Bridges, and M. J. Rosseinsky, *Angew. Chem. Int. Ed.* **43**, 3562 (2004).
- [110] K. E. Arpino, B. A. Trump, A. O. Scheie, T. M. McQueen, and S. M. Koohpayeh, *Phys. Rev. B* **95**, 094407 (2017).

- [111] K. Baroudi, B. D. Gaulin, S. H. Lapidus, J. Gaudet, and R. J. Cava, *Phys. Rev. B* **92**, 024110 (2015).
- [112] G. C. Lau, B. D. Muegge, T. M. McQueen, E. L. Duncan, and R. J. Cava, *J. Solid State Chem.* **179**, 3126 (2006).
- [113] R. D. Shannon and C. T. Prewitt, *Acta Crystallogr. Sec. B* **25**, 925 (1969).
- [114] S. T. Bramwell, M. N. Field, M. J. Harris, and I. P. Parkin, *J. Phys.: Cond. Mat.* **12**, 483 (2000).
- [115] B. Tomasello, C. Castelnovo, R. Moessner, and J. Quintanilla, arXiv e-prints , arXiv:1810.11469 (2018).
- [116] K. Matsuhira, M. Wakeshima, Y. Hinatsu, C. Sekine, C. Paulsen, T. Sakakibara, and S. Takagi, *J. Phys. Conf. Ser.* **320**, 012050 (2011).
- [117] S. Gao, O. Zaharko, V. Tsurkan, L. Prodan, E. Riordan, J. Lago, B. Fåk, A. R. Wildes, M. M. Koza, C. Ritter, P. Fouquet, L. Keller, E. Canévet, M. Medarde, J. Blomgren, C. Johansson, S. R. Giblin, S. Vrtnik, J. Luzar, A. Loidl, C. Rüegg, and T. Fennell, *Phys. Rev. Lett.* **120**, 137201 (2018).
- [118] S.-Y. Kim, *J. Kor. Phys. Soc.* **65**, 970 (2014).
- [119] R. Higashinaka, H. Fukazawa, D. Yanagishima, and Y. Maeno, *J. Phys. Chem. Solid* **63**, 1043 (2002).
- [120] J. P. C. Ruff, R. G. Melko, and M. J. P. Gingras, *Phys. Rev. Lett.* **95**, 097202 (2005).
- [121] J. Xu, V. K. Anand, A. K. Bera, M. Frontzek, D. L. Abernathy, N. Casati, K. Siemensmeyer, and B. Lake, *Phys. Rev. B* **92**, 224430 (2015).
- [122] K. Matsuhira, Y. Hinatsu, K. Tenya, H. Amitsuka, and T. Sakakibara, *J. Phys. Soc. Jpn.* **71**, 1576 (2002).
- [123] R. Higashinaka, H. Fukazawa, K. Deguchi, and Y. Maeno, *J. Phys. Soc. Jpn.* **73**, 2845 (2004).
- [124] L. Savary and L. Balents, *Phys. Rev. Lett.* **118** (2017).
- [125] N. Martin, P. Bonville, E. Lhotel, S. Guitteny, A. Wildes, C. Decorse, M. Ciomaga Hatnean, G. Balakrishnan, I. Mirebeau, and S. Petit, *Phys. Rev. X* **7**, 041028 (2017).

- [126] J.-J. Wen, S. M. Koochpayeh, K. A. Ross, B. A. Trump, T. M. McQueen, K. Kimura, S. Nakatsuji, Y. Qiu, D. M. Pajerowski, J. R. D. Copley, and C. L. Broholm, *Phys. Rev. Lett.* **118**, 107206 (2017).
- [127] D. H. Zwillinger, *CRC standard mathematical tables and formulae*, 30th ed. (CRC, Boca Raton ; London [u.a.], 1996).
- [128] R. V. Jones, *J. Sci. Instrum.* **28**, 38 (1951).
- [129] R. V. Jones and I. R. Young, *J. Sci. Instrum.* **33**, 11 (1956).
- [130] H. Sato, K. Matsuhira, T. Sakakibara, T. Tayama, Z. Hiroi, and S. Takagi, *J. Phys.: Cond. Mat.* **19**, 145272 (2007).

Acknowledgments

Many people have helped me to finish this thesis and I want to seize the opportunity to thank some of them explicitly.

First of all, I want to thank Dr. Mathias Doerr for his support and supervision throughout my time at the TU Dresden introducing me to the methods and experimental techniques, the valuable discussions and the revision of this manuscript.

I'm equally grateful to Prof. Dr. Jochen Wosnitza for his ideas and suggestions of experiments, scientific guidance and his input for posters, talks, papers and this thesis.

Some of the experiments would not have been possible without the enduring support of Dr. Toshihiro Nomura; thank you.

I want to thank Dr. Martin Rotter for his very important help for the simulation using the McPhase software bundle. Additionally, he provided me with valuable literature and shared his deep knowledge with me during long discussions.

I thank Dr. Sergei Zherlitsyn, Dr. Haidong Zhou and Dr. Oleg Petrenko for providing me with samples of the rare-earth pyrochlores, in particular $\text{Dy}_2\text{Ti}_2\text{O}_7$ and $\text{Ho}_2\text{Ti}_2\text{O}_7$, studied in this manuscript. In addition, I thank Dr. Mathis Antlauf for the collaboration in the project of the Si-substituted dysprosium germanate.

I thank the SFB 1143 for funding my research.

Last but not least, I want to thank my family and friends who have supported me during my PhD time in Dresden, in particular Miriam Rein, Thomas Preck and Heike Grunow.

Versicherung

Hiermit versichere ich, dass ich die vorliegende Arbeit ohne unzulässige Hilfe Dritter und ohne Benutzung anderer als der angegebenen Hilfsmittel angefertigt habe. Die aus fremden Quellen direkt oder indirekt übernommenen Gedanken sind als solche kenntlich gemacht. Die Arbeit wurde bisher weder im Inland noch im Ausland in gleicher oder ähnlicher Form einer anderen Prüfungsbehörde vorgelegt.

Die vorliegende Dissertation wurde am Institut für Festkörper- und Materialphysik der Technische Universität Dresden unter der wissenschaftlichen Betreuung von Herrn Dr. Mathias Doerr und Prof. Dr. Joachim Wosnitza angefertigt.

Ich erkenne die Promotionsordnung der Fakultät Mathematik und Naturwissenschaften der Technischen Universität Dresden an.

Thomas Stöter
Dresden,